Università degli Studi di Napoli "Federico II"

Dottorato di Ricerca in Fisica Fondamentale ed Applicata
XXV Ciclo (2010-2013)

Structural and Electronic Properties of Oxide Surfaces and Interfaces: an *Ab-Initio* Study

Thesis for Doctor of Philosophy degree
submitted by Nunzio Roberto D'Amico

Supervisors:

Prof. Domenico Ninno

Dr. Giovanni Cantele

Coordinator:

Prof. Raffaele Velotta

Contents

Introduction

Nanoscience is an emerging field of research related to the capability to construct extremely small objects (nanotechnology). It is a highly cross-disciplinary research area, which is going to play a crucial role in future scientific discoveries and new technologies.

In particular metal oxide low dimensional structures are an important class of nanomaterials with unique properties and useful functionalities that are attractive for a variety of applications ranging from electronics to biomedicine and energy conversion. Salient features include abundance and usually high stability. To grow metal oxide nanostructures with desired surface chemistry and orientation, size, shape, and crystal structure in a controllable manner is a primary goal in nanomaterials research but still presents a major challenge today. Toward this goal, substantial research efforts have been made on both the experimental and theoretical fronts [1, 2, 3, 4, 5]. In particular, on the theoretical front, the Density functional theory (DFT) has proven to be a powerful tool for ab-initio calculations giving valuable information on both the structural and the electronic properties arrangement of nanoscale systems. In this thesis we have performed DFT calculations for two different classes of metal oxides low dimensional structures.

The first class of systems which will be considered concerns the *clean and defected zinc oxide non polar surfaces*. We have limited our attentions on the ZnO surfaces because the ZnO nanostructures are considered ideal candidates for the detection of specific gas molecules in mixtures of various gases. The detection of specific gas molecules is increasingly required for the control and monitoring of several industrial and medical processes [6, 7]. Solid-state gas sensors based on metal–oxide–semiconductor materials have attracted considerable attention during the past decade [8, 9, 10, 11, 12, 13, 14] due to low cost, small dimensions, and high compatibility with microelectronics processing. The conventional sensing mechanism relies on the charge transfer between the absorbed gas and the metal oxide surface. Depending on the semiconductor type, the charge transfer will either increase or decrease the concentration of the majority carriers, thereby increasing or decreasing the

sensor electrical conductance [13, 14].

Zinc oxide (ZnO), tin dioxide (SnO_2) and titanium dioxide (TiO_2) nanostructures have been identified as promising gas-sensitive materials with many well documented applications [14, 15, 16, 17, 18, 19, 20, 21, 22]. In particular, ZnO is interesting because of its mixed covalent/ionic character in the chemical bonding, with peculiar properties such as large exciton binding energy (60 meV) and direct band gap (3.4 eV). The versatility and multi-functionality of this material are testified by the wide range of possible applications in varistors [23], surface acoustic wave devices [24], transparent conducting oxide electrodes [25], solar cells [26], blue/UV light emitting devices [27], self-powered (nano)devices [28, 29] and, as mentioned, gas sensors [30, 31]. Of course, it is expected that photocatalysis and gas sensing applications require a precise control on the surface morphology, chemistry and composition: usually, nanostructures with different surface facets are employed, the $(10\bar{1}0)$ and $(11\bar{2}0)$ surfaces/facets being the most stable and abundant ones [32, 33].

Since the ZnO properties are highly sensitive to the nature and concentration of lattice imperfections [34, 35], understanding the thermodynamics and kinetics of point defects in ZnO is not only of fundamental but also of significant technological interest. For example, zinc migration, which is believed to proceed through the migration of intrinsic defects in the vicinity of grain boundaries - most likely zinc interstitials - has been discussed in connection with the degradation of varistors devices [36, 37]. Moreover, it has been argued that the presence of native surface and subsurface point defects, their concentration and depth distribution can strongly affect the electronic properties and electrical response of metal-ZnO interfaces and Schottky barriers, as well as the gas adsorption on specific ZnO surfaces [38].

Some *ab initio* density functional theory (DFT) calculations have been performed in the past to elucidate the behavior of both intrinsic [39, 40, 41, 42] and extrinsic point defects [43, 44]. It is widely accepted that oxygen vacancies can be considered as the most abundant and the chemically most reactive kind of atomic defects for a large variety of oxides [45]. Previous theoretical studies of the bulk ZnO and its surfaces have proven the impact of oxygen deficiency on the electronic and structural properties [46, 47, 48, 49, 50]. Nevertheless, a systematic study of the vacancy diffusion along and across the ZnO non–polar $(10\bar{1}0)$ and $(11\bar{2}0)$ surfaces together with the implications on relevant material properties is still lacking. Moreover, the actual possibility of observing stable (sub)surface oxygen defects has been experimentally proven in the early 80's [51, 52], but questioned by recent STM experiments [53, 54].

In particular, in the works of Göpel *et al.* [51, 52], intrinsic point defect were intentionally induced, with a maximum coverage of 1%, by pursuing

several routes, including:

- high-temperature treatment and subsequent cooling down under ultra-high vacuum conditions;
- UV illumination, leading to thermally activated desorption of oxygen atoms;
- in the absence of UV light, by CO exposure and subsequent CO_2 desorption.

Of course, the surface defects could only be frozen in the absence of O_2, since they react rapidly with oxygen even at low temperature (T $\leq$ 700 K). In the same experiments, fundamental effects induced by the presence of oxygen vacancies, such as the formation of strong accumulation layers, surface free carriers, variations in rates of charge transfer, were extensively characterized. At variance with these results, more recent studies, based on atomically resolved STM experiments [53, 54], have found no signature of the presence of oxygen defects on the same surface.

Therefore, in this thesis, we try to elucidate the apparent disagreement of the available experimental data, which report the observation of a finite concentration of oxygen vacancies or the lack of them close to the surface. With this aim, we also consider the energetics of ZnO-dimer and Zn vacancies, which might occur as the prevailing atomic defects under suitable conditions of temperature and pressure. Moreover, we characterize the defected surfaces electronic and structural properties as a function of the position of the defect with respect to the surface and discuss the diffusion paths of such defects both parallel and across the surfaces.

The second class of metal oxides nanostructures that we have investigated in this thesis is represented by $SrTiO_3$–TiO_2 *interface*. With the advances in thin-film-deposition techniques, such as laser deposition and molecular-beam epitaxy, oxide heterostructures with atomically abrupt interfaces have been realized. A broad range of novel physical phenomena emerges in the presence of interfaces that are not found neither in the bulk counterparts nor in conventional semiconductor heterojunctions. The ability of engineering atomically precise complex interfaces paves the way to an incredible variety of new functional devices. Even the simplest binary oxides, depending on the cation type, the crystal structure, and its stoichiometry, exhibit a broad range of behaviors [38, 55, 22] ranging from insulating to metallic, magnetic, or superconducting. The more complex ternary or higher-order oxides show even more exotic properties like ferroelectricity, colossal magnetoresistance, or high-temperature superconductivity. Even more exciting is the possibility

of combining the properties of individual oxides into various heterostructures. It is, indeed, important to note that the introduction of interfaces in conventional semiconductors has spawned the discovery of many physical phenomena which have led to the invention of numerous semiconductor devices, like transistors, lasers or solar cells, that dominate the nowadays technology. Since oxides exhibit an interesting and variegated physics already in the bulk, we can expect that physical phenomena at interfaces may go well beyond those exhibited by conventional semiconductors interfaces [56, 57, 58].

$SrTiO_3$–TiO_2 is one of the most important interface that has attracted considerable attention from several research groups [59, 60, 61, 62, 63]. In particular a series of experiments [64, 61] has shown the existence of a two dimensional electron gas (2DEG) between the two insulating oxides $SrTiO_3$ and TiO_2 anatase. Extrinsic doping, in the form of oxygen vacancies, has been considered responsible of existence of the 2DEG.

In this thesis we have focused on the determination (with ab initio calculations) of the band offset of this interface. The band offset, i.e., the relative position of the energy levels on both sides of the interface, is one of the most important quantities that characterize an interface. The valence-band offset (VBO) [conduction-band offset (CBO)] is defined as the difference between the position of the top of valence bands [the bottom of the conduction bands] of the two materials. These bands discontinuities have a profound effect on the electronic transport and carrier confinement in electronic devices containing heterojunctions.

Recently, Chambers *et al.* [65], using x-ray photoelectron spectroscopy (XPS), have reveled, for the $SrTiO_3$–TiO_2, a VBO ranging between -0.06 eV and $+0.16$ eV depending on the anatase thickness. Therefore they have reported that there is no measurable valence band offset between anatase TiO_2 (001) and $SrTiO_3$ (001). Curiously, the VBO has also been theoretically calculated [65], but the prediction ($+0.55$ eV) largely overestimates the experimental results.

Therefore, in this thesis, we report on first principles calculations of the properties of the epitaxial $SrTiO_3$–TiO_2 (anatase) heterojunction, with an emphasis on the electronic band profile and lineup at the interface. In particular we try shed light on the discrepancy between experimental and theoretical results, through a detailed ab initio study aimed to gaining insight on the role played by oxygen vacancies in the near-interface region.

The thesis is organized as follows. In chapter 1, we review the fundamental aspects concerning the physics of oxides and of defects. We also describe some experimental results and we pay particular attention to those findings that are still debated and to the works that have been compared and relied on

throughout the thesis. In chapter 2, we present the main features of ab-initio calculations based on DFT, with an emphasis to the ability of modeling bulk structures as well as confined systems like surfaces and interfaces, through an opportune setting of the periodic conditions imposed to the system. In the third chapter we describe the technique, the nudge elastic band (NEB) method, that is used to identify the "minimum energy path" (MEP) connecting stable states of the potential energy surface. We also describe the climbing image nudged elastic band that is a extension to the NEB method. In chapter 4, we present our ab-initio calculations on the ZnO non-polar surfaces, focusing on the variation of the structural and electronic properties induced by surface and sub-surface oxygen vacancies and on the diffusion of oxygen vacancies on the ZnO non-polar surfaces. In chapter 5, the attention is addressed to the $SrTiO_3$–TiO_2 interface focusing on the band offset and on the effects of the oxygen vacancies on the properties of this interface. Finally, we make conclusive remarks and indicate the possible developments in the conclusive section.

Chapter 1

An overview of some experimental measurements

This chapter starts with a introduction to the oxide materials focusing, in particular, on the oxide surfaces and interfaces. Then there is brief discussion of the role of point defects (i.e. oxygen vacancies) on the properties of the oxide surfaces and interfaces. Finally, the chapter closes with a description of the most important properties of materials studied in this thesis (ZnO, $SrTiO_3$, TiO_2) showing in particular some experimental results on the:

- *ZnO non-polar surfaces*
- *$SrTiO_3 - TiO_2$ interface.*

1.1 Oxide materials

Oxide materials have long been known as hosts to an incredible variety of physical phenomena. Even the simplest binary monoxides exhibit broad range of properties ranging from insulating to metallic, magnetic, or even superconducting, depending on the type of the cation and the crystal structure. The more complex ternary or higher-order oxides show even more exotic properties like ferroelectricity, colossal magnetoresistance, or high-temperature superconductivity. Such a broad spectrum of physical properties found in oxides results mainly from a unique balance between ionic and covalent bonding so that even subtle structural changes, like bond lengths or angles, have a profound effect on the interplay among the valence electrons and dramatically affect material properties. Furthermore, the properties are extremely sensitive to pressure or chemical doping offering many routes to

control and engineer new functionalities making oxides very promising materials for industrial applications [66, 67].

Oxide materials may involve strongly correlated electrons for which the bandwidth is comparable to the on-site Coulomb interaction. These systems are very challenging from the theoretical point of view as they can neither be described by nearly free electron model, nor by a completely ionic model. They exhibit many exotic behaviors and often condense into variety of phases with separate ordering of their charge, spin and orbital degrees of freedom. The different electronic phases compete with each other and are highly sensitive to external parameters such as electric and magnetic fields and temperature. Moreover different electronic degrees of freedom couple with each other or with the lattice, leading to remarkable and useful phenomena such as colossal magnetoresistance or magnetoelectric effect.

1.2 Oxide surfaces

A surface is the boundary between the bulk solid and its environment, and represents a rather unique type of defect in the solid state. At a surface, the periodicity of the bulk solid is abruptly terminated along one direction which results in dangling bonds that increase the surface free energy. Under suitable conditions these atoms can relax and/or organize themselves into structures that have translational periodicities larger than those of bulk. This is more evident on low index surfaces since they have higher dangling bond densities. These reconstructions generally involve a few atomic layers and are accompanied by strain fields that decay exponentially into the bulk [68, 69]. Reconstructions can be broadly divided into two classes: native and adatom induced, depending on the presence or absence of foreign species on the surface.

Surface structures are classified by one of the 17 crystallographic plane groups since they possess only two-dimensional periodicity. The 2-D surface mesh generated by bulk truncation is the most natural coordinate system to describe the structure, and the reconstruction is described by its size and orientation relative to the primitive 1×1 lattice [70].

The technological importance of surfaces and the various novel structures they adopt cannot be overstated. The semiconductor industry, with its ever shrinking device dimensions, drives the need for understanding the various atomic-scale surface phenomena. As the feature sizes in CMOS devices shrink, a transition needs to be made from the current microelectronics technology and molecular electronics. In this limit, a bottom-up approach to device fabrication is inevitable, wherein devices are assembled a few atoms at a

time. Nanostructured surfaces are nowadays increasingly used as substrates for growing articial structures with specific conformations. Reconstructed surfaces with large unit cells may also drive specific growth modes, favouring for example the formation of size-controlled clusters. Vicinal surfaces, which exhibit arrays of parallel steps, can be used to make quantum wires: the migration of metallic adatoms on the surface after deposition is driven by the presence of the steps, and the atoms gather in linear chains rather than disperse on the surface.

Another discipline where a fundamental understanding of surface processes is indispensable is catalysis. Traditionally, technological developments in the area of heterogeneous catalysis are products of the trial and error technique, though, research over the last few decades has shed some light on the underlying processes [71]. Vital to the understanding of a catalytic reaction is the knowledge of the atomic-scale structure of the surface, which aids the identication of catalytically active sites. Oxides (of transition metals) comprise the vast majority of the catalysts used in the chemical industry, either in the form of the active material or as support. Transition metal cations exhibit multiple valencies and form a rich array of compounds whose bulk properties are well characterized.

The most commercial catalysts consist of microscopic particles of a metal supported on a high-surface-area oxide. The two most commonly used oxide supports are SiO_2 and Al_2O_3. Metal catalysts supported on such nonreducible oxides generally exhibit little effect of the presence of the support, but in some cases either the interaction between the catalyst and the support, or the existence of complementary reactions taking place on the metal and the oxide play an important role in catalysis. When catalyst metals are supported on reducible transition-metal oxides, strong interactions can occurs that alter the catalytic behavior of the metal.

Metal oxides are also themselves catalysts for a variety of commercially important reactions. Sometimes a metal oxide is used in its pure form (e.g.. bismuth molybdate for the oxidation of propene to acrolein or acrylonitrile), while in other cases the oxide is supported on another oxide, and the catalytic activity results from the interaction between the two oxides (e.g.. V_2O_5 supported on TiO_2 for the selective oxidation of hydrocarbons and the selective catalytic reduction of nitrogen oxides). All of these catalytic reactions proceed by complex mechanisms that involve a range of different chemical interactions: these include acid/base reactions as well as oxidation and reduction steps where lattice oxygens are lost and gained by the substrate

Another important application of metal oxides is as gas sensors. The most studied oxides for this purpose are ZnO and SnO_2. Both of these have high bulk electrical resistivity when stoichiometric, although they normally

behave as n-type semiconductors due to the presence of defects or deliberate doping. The absorption of certain molecules bends the bands at the surfaces, producing changes in surface conductivity and can be used to monitor the presence of that molecule. In some cases the sensitivity and selectivity of the material can be improved by deposition of submonolayers of metal on the oxide surface. In literature there are many works that investigate the atomic and electronic properties of the surfaces of these materials [72].

The theoretical classification of surfaces, based on a classical electrostatic analysis and proposed by Tasker [73], allows to understand some experimental results. Figure 1.1 illustrates the various possible atomic configurations for the surfaces. Type 1 or type 2 (non-polar) surfaces which differ in the charge Q borne by their layers have a zero dipole moment in their repeat unit and are thus potentially stable. In contrast, polar type 3 surfaces have a diverging electrostatic surface energy [73] due to the presence of a non-zero dipole moment not only on the outer layers, but also on all the repeat units throughout the material. The cancellation of this macroscopic dipole moment can be achieved by one of three mechanisms:

- **Changes in the stoichiometry of surface.** Assuming that surface species retain their bulk oxidation states, the excess charge at the surface can be balanced by having a surface that is stoichiometrically different from the bulk. This process is usually accompanied by a reconstruction of the first few surface layers and faceting depending upon how the vacancies or adatoms order.

- **Adsorption of charged foreign species.** The residual atmosphere in the experimental set-up usually contains charged radicals, for example OH^-, which can adsorb on the surface and provide charge compensation.

- **Modification of the surface electronic structure.** Charge compensation can be attained through an electron redistribution in response to the polar electrostatic field. This is achieved by a total or partial filling of surface states, sometimes leading to surface metallization.

Polar surfaces of compound semiconductors have been studied extensively due to the fact that the (100) surface of zinc-blende compounds serves as a substrate for the growth of nearly all $III-V$ and $II-VI$ device layers.

Polar oxide surfaces are much more diverse, presenting a vast number of crystallographic structures: rock-salt, corundum, spinel, inverse spinel, wurtzite, perovskite. The nature of metal-oxygen bonding in these oxides

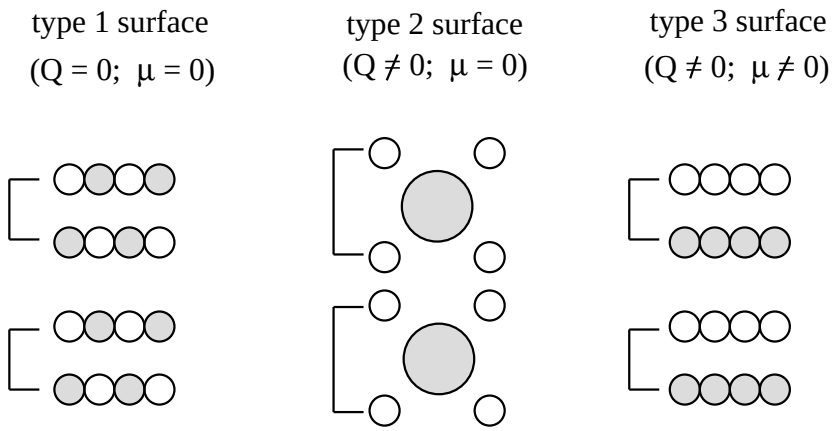

Figure 1.1: Classification of surfaces of compounds. Q is the total charge in a layer and μ is the net dipole moment normal to the surface

span the entire range between fully ionic and primarily covalent. Transition metal oxides add another dimension to the problem forming mixed valence compounds (like Fe_3O_4) which stabilize oxides with different stoichiometries depending on temperature and oxygen partial pressure. In a seminal article in 1992, Wolf [74] argued that surfaces of ionic rock-salt oxides should be terminated with complete $(MO)_4$ octopolar units. The octopolar units ensure charge neutrality of the surface and also have rapidly decaying electrostatic interactions. However, this result is valid only if both the anion and the cation retain their bulk oxidation states and the surface reconstructs stoichiometrically. Since the atoms in the near surface region are in a very different environment (compared to bulk) they almost never have the same oxidation state as the bulk atoms. The validity of this model in the presence of excess anions (or cations) is not clear. Nevertheless, the octopolar unit is a recurring structural motif in various reconstructions on $MgO(111)$ [75] and $SrTiO_3$ (111) surfaces [76]. More recently, Warschkow *et al.* [77] have hypothesized that the ability of the surface oxygen atoms to relax out of the surface plane can be used as a reliable predictor for determining the stability of various structures on $SrTiO_3$ (100) surface.

Despite these efforts, presently there is no definitive method of predicting what the surface rearrangements will be in a given material. Even the various atomic structures experimentally determined are in disagreement with theory in terms of energetics. They may well be kinetically trapped structures [78], but such discord helps in gaining signicant insight into the nature of surfaces and help in developing a tool to predict surface structures.

1.3 Interfaces between oxides

While oxide materials exhibit a variety of remarkable and potentially useful phenomena already in the bulk form, perhaps even more exciting is the possibility of combining the properties of individual oxides into various heterostructures. Indeed, the introduction of interfaces in the semiconductor structures spawned discovery of many fascinating physical phenomena which led to invention of numerous semiconductor devices, like transistors, lasers or solar cells, that dominate the nowadays technology. Interestingly, in the bulk of the material, the behavior of conventional semiconductors like silicon is less exciting. Since oxide materials exhibit spectacular physics already in the bulk, we can expect that physical phenomena possible at oxide interfaces go well beyond those exhibited by interfaces between conventional semiconductors.

The physics of oxide interfaces is largely unexplored since the progress in this field was for many years thwarted by difficulties in growing epitaxial oxide multilayers [56]. This problem was recently overcome by development of new deposition techniques like molecular beam epitaxy (MBE) and pulsed laser deposition (PLD). These methods enable growth of high-quality oxide heterostructures with atomically sharp interfaces. They are grown layer by layer as can be monitored in situ by reflection high-energy electron diffraction (RHEED). Currently, it is possible to deposit thin films even one atomic layer thick. The spectacular properties of oxide materials involve ordering and mutual interaction of different degrees of freedom like charge, spin, orbital and lattice. Therefore the presence of an interface can affect these degrees of freedom and may lead to new exciting physical phenomena. In particular we can distinguish five different mechanisms by which the interface affects the properties of oxides: *symmetry breaking, charge transfer, strain, frustration and electrostatic coupling* [57] (Fig. 1.2).

- **Symmetry breaking.**

  When an interface between two oxides is created, it is broken the translational symmetry of both materials. This modifies electronic states at the interface altering the hybridization of the ionic orbitals which in turn modifies electronic orderings. Furthermore, new states can be formed within band gaps that are localized close to the interface. These interface states are direct consequence of translational symmetry breaking that invalidates the Bloch theorem and don't require change of the charge density. The interface states can pin the position of the Fermi level determining transport properties and charge transport across the interface.

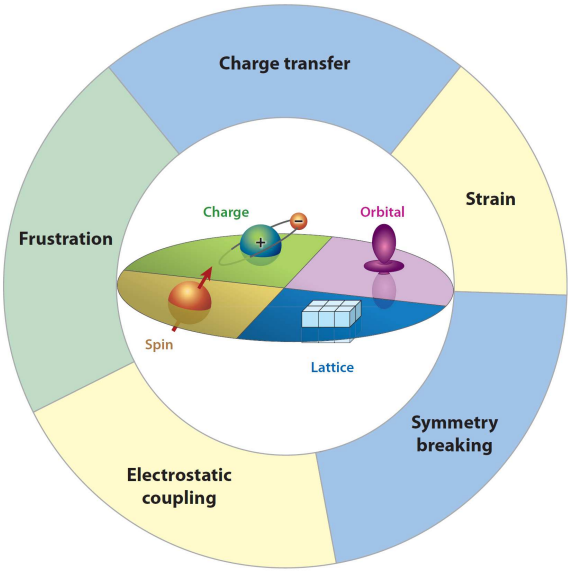

Figure 1.2: Spectacular properties of many oxides arise from the complex interactions between their charge, orbital, spin, and lattice degrees of freedom. These interactions can be modified at the interface by mechanisms of symmetry breaking, charge transfer, electrostatic coupling, frustration, and strain, leading to new behavior. The Figure is taken from Ref. [57].

Similarly, as in the case of surface, the atoms at the interface can undergo reconstruction further breaking the symmetry of the constituent bulk oxides. In perovskites for example, the presence of interface can induce rotation of oxygen octahedra in the ideal cubic structure of the bulk oxide which can change its conducting and magnetic properties as well as the ferroelectric order.

- **Charge transfer.**

  When two oxides are stacked together creating an interface, there is charge transfer between them in order to equalize electronic chemical potentials of both materials. This phenomenon is mainly responsible for rich physics in conventional semiconductor heterostructures that led to devices like p-n junction, Schottky diodes, or high-mobility transistors based on two-dimensional electron gas (2DEG). Naturally the same effects exist at the oxide interfaces. In particular, high mobility 2DEG was reported at high-quality $ZnO - Mg_xZn_{1-x}O$ interface that allows observation of the quantum Hall effect (QHE) [79]. Therefore there is the possibility of 2DEG at the interface between oxides with different

types of electronic orders, like magnetism or superconductivity that could interact with QHE [57].

Recently, 2DEG was observed at the interface between two band insulators $SrTiO_3$ and $LaAlO_3$ [80]. While the origin of this 2DEG is not fully understood yet, it is clear that the mechanism is quite different than in the case of semiconductor heterostructures. The charge transfer at the oxide interfaces leads to effective doping of the space charge region. The filling or emptying electronic states at the interface strongly affects interaction between electronic degrees of freedom. For example, in the case of interface between two insulating antiferromagnets $LaMnO_3$ and $SrMnO_3$ the charge transfer leads to the interface ferromagnetism [81].

- **Strain.**

  Lattice mismatch between substrate and deposited material leads to the biaxial strain. The strain changes the distance between the ions in the oxide thin film altering the orbital overlap and hence affecting electronic and lattice degrees of freedom. For example, $SrTiO_3$ becomes ferroelectric under strain and multiferroicity can be induced by epitaxial strain in $EuTiO_3$. In particular, by choosing different substrate, the magnitude and the sign of epitaxial strain can be altered providing a powerful tool for tuning the properties of oxides and stabilizing alternative orderings.

- **Frustration.**

  Particularly interesting effects can arise at the interface between oxides with electronic or lattice orderings which cannot coexist, i.e., there is a frustration at the interface. In an attempt to reduce frustration materials often undergoes dramatic changes that lead to new phases that are absent in the bulk of both constituents. For example, at the interface between ferromagnetic $La_{0.6}Sr_{0.4}MnO_3$ (LSMO) and antiferromagnetic $La_{0.6}Sr0.4FeO_3$ spin frustration leads to the canting of spins and a reduction of overall magnetic moment. As both ferromagnetism and conductivity in LSMO are mediated by electron hopping, the conductivity of LSMO is also reduced due to interfacial effect. Application of magnetic field restores ferromagnetic alignment and increases conductivity leading to large magnetoresistance [82].

- **Electrostatic coupling.**

  At the interface where one or both oxides are ferroelectric, the electrostatic boundary conditions must be satisfied leading to an elec-

trostatic coupling between the layers. For example, in the case of $BaTiO_3/SrTiO_3$ superlattices grown on $SrTiO_3$ substrate $BaTiO_3$ is under compressive strain that induces out-of-plane electric polarization. Since $SrTiO_3$ is not under strain, one could expect that it remains paraelectric as in the bulk. However, the condition for continuity of the electric displacement across the interfaces means that any polarization mismatch between the layers would give rise to depolarizing field with a large energy cost. The structure thus adopts uniformly polarized state with the polarization value determined by the competition between the energy cost of polarizing the paraelectric $SrTiO_3$ layers and the energy gain in preserving the polarization in $BaTiO_3$ layers.

1.4 Defects and oxygen vacancies

During the course of the last century, it has been realized that several properties of solid materials are controlled not so much by their geometric and electronic structure, but by faults or defects in the structure. For instance, the strength of a metal is largely determined by the presence of extended defects called dislocations; the color of a gemstone is entirely related to the presence of impurity atoms in the lattice; even the electronic properties of the semiconductors present in our electronic devices are connected to the level of doping introduced by the insertion of impurity atoms. Defects are also terribly important in chemistry, as they largely determine phenomena such as corrosion, which costs billions of dollars each year, and catalysis by certain oxides, an activity which is the basis of a large fraction of the whole chemical industry. In summary, there is no aspect of chemistry and physics of solids which is not decisively affected by the presence of defects in a material.

For these reasons, the study of the chemical, electrical and optical properties of defects has attracted a continuously increasing interest in modern material science, to the point that a new discipline has emerged; defect engineering. Defect engineering is aimed at manipulating the nature and the concentration of defects in a material so as to tune its properties in a desired manner or to generate completely new and unexpected behaviors. For instance, by changing the defect concentration, one can turn a colorless insulator into a black material with metallic conductivity or an ordinary copper oxide into a high temperature superconductor. While this is well-known in the field of bulk materials, it is only more recently that attention has been given to the problem of defects at the surface or interface of solids.

On a metal the defect can consist of an impurity or dopant atom, or can be an extended morphological irregularity like a step. In an ionic compound,

the complexity of defects is at least one order of magnitude higher than in metals because of the presence of anions and cations, which can assume a variety of charged states. Then this situation is particularly pronounced in metal oxides, also because of the very large number of these compounds.

As we said, oxide surfaces are finding continuous new applications in advanced technologies such as in corrosion protection, coating for thermal applications, in catalysis as inert supports or directly as catalysts, in sensors, in microelectronics for their dielectric properties. Films of magnetic oxides are integral components in magnetic recording devices and many microporous materials are based on oxides. For all the reasons mentioned above, there is a considerable effort to better characterize the surface of oxides or the interface between an oxide and another materials (a metal, a semiconductor, or another oxide). This implies also a detailed mapping of the surface and interface defects. This is a difficult task because of their low concentration and of the great variety of possible defect situations.

Among all the defects in the oxides, the oxygen vacancy is one of the most important and is supposed to be the prevalent defect in many oxides. Depending on the material, the structure and properties of oxygen vacancies can vary substantially. One could say that the oxygen vacancy is a fingerprint of the electronic structure of the oxide.

In general, a detailed understanding and a control at the atomistic level of the nature and concentration of point defects in oxides (not only vacancies) is essential for the understanding of their structure-properties relationships. But the problem is that defects are often elusive species, highly diluted, and therefore difficult to detect.

The same happens with the identification of defects and vacancies at oxide surfaces. Very often the proofs of their existence are indirect, based on the change of a property or of a spectroscopic response as a function of the number of defects present in the sample. For instance, the oxygen vacancies often result in peculiar optical properties and in a specific color of the sample. Sometimes one can use more sophisticated techniques to prove the presence of defects. Some defects consist of single electrons trapped in special sites (including oxygen vacancies). The resulting centers are paramagnetic, and their presence can be detected by electron paramagnetic resonance (EPR) [83]. This technique is rather sensitive to the presence of unpaired electrons, being able to reveal 10^{12} spins; this means that for a high surface area polycrystalline sample of 200 m^2g^{-1}, the lower limit of sensitivity is 10^7 spins cm^{-2}, that is, about a paramagnetic center every 10^8 surface atoms. This level is much better than the sensitivity of optical measurements which, for high dilutions, cannot detect the electronic states associated with the defect.

Moreover, the dynamics of surface oxygen vacancies are essential for the

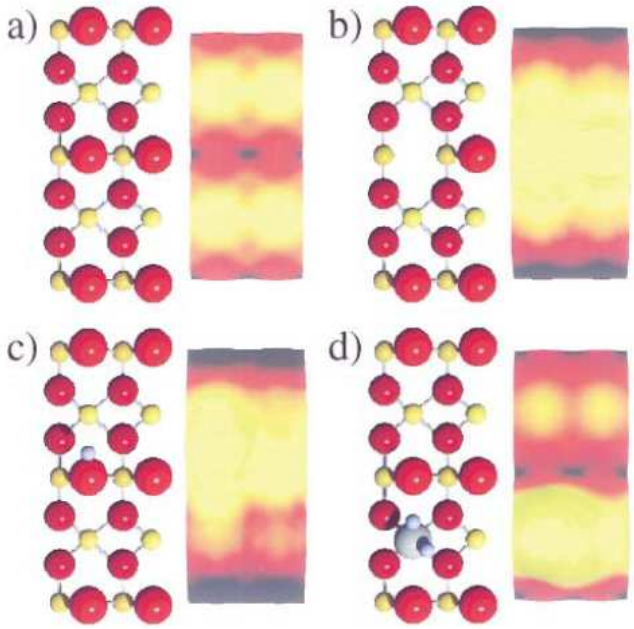

Figure 1.3: Ball-and-stick model and corresponding simulated STM image of the TiO_2 surface showing the appearance of *a*) vacancy-free surface, *b*) bridging oxygen vacancy, *c*) bridging OH group, and *d*) water molecule on top of a Ti atom. Red atoms: O; yellow atoms: Ti; blue atoms H. The Figure is taken from Ref. [45].

understanding of numerous reactions in catalysis by transition-metal oxides. For example, the oxidation of an organic substrate at an oxide surface usually occurs at the expense of a surface lattice oxygen atom, and results in the formation of a surface vacancy. The role of gas-phase O_2 in the process is to react with the surface to regenerate the surface oxygen atom. At an atomistic level, this implies that the O_2 molecule dissociates at the vacancy site, with formation of highly reactive atomic oxygen and of the regular surface. The study of Schaub *et al.* [84] provides a direct proof and a detailed interpretation of the mechanism of this process on the TiO_2 surface. Recently the same group has shown the role of oxygen vacancies on the TiO_2 surface in dissociating water [84] (Fig. 1.3).

Using STM images and DFT calculations they showed that the amount of water dissociation is limited by the density of oxygen vacancies and that the dissociation takes place as soon as molecular water is able to diffuse to the active site.

Oxygen vacancies are relevant not only in catalysis by oxides. Recently it

has been suggested that they can play an important role in tuning the activity of supported metal nanoparticles. We have assisted spectacular advances in the deposition of metal clusters on oxide surfaces in the last years [85]. These systems represent well-defined models of the more complex and often not well-understood catalysts consisting of small particles deposited by chemical impregnation on inert supports (silica, alumina, etc.). The key problem in this research area is the control of the size of the particles, in order to generate a system with a narrow distribution of the particle dimensions. Thanks to new experiments designed to nucleate clusters under controlled conditions [85], it has been possible to produce collections of nanosized particles, all having the same dimensions. For many years this has been the dream of people working on supported metal clusters. The conditions in which this has been realized are very far from the actual working conditions of the practical catalysts. Still, these experiments offer the unique opportunity to study the cluster reactivity as a function of the particle size [86], opening up new perspectives for the understanding of the basic principles of catalysis by metal particles.

To understand the connection between the field of supported nanoclusters and the problem of oxygen vacancies at oxide surfaces, it is necessary to think about what happens when the metal atoms are deposited onto the oxide surface from the vapor phase. The atoms impinging on the surface can stick to it, diffuse on the surface, or re-evaporate, depending on the strength of the interaction with the substrate, of their kinetic energy, and of the amount of thermal energy in the system. In the process of diffusing on the surface, it can happen that the atoms encounter a specific site where the interaction is stronger and the diffusion barrier is higher. On these sites the atoms remain trapped and there is a given probability that a second atom diffusing on the surface binds to the first one, which gives rise to the nucleation and growth of the metal cluster. It is a general belief that oxygen vacancies are among the most likely sites for the nucleation to occur. Even when the clusters are generated in the gas-phase and soft-land on the oxide surface there is indication that oxygen vacancies are important for their stabilization. The binding of a metal atom or a cluster to an oxygen vacancy can be three to four times larger than on the regular sites [87, 88]. It is not surprising that these are the most likely sites for the nucleation to occur. It should be mentioned, however, that some theoretical studies cast doubts on this view, at least for the transition-metal atoms at the right of the periodic table [89]. But there is also another reason why these centers are important. For very small cluster sizes, in the nanometer regime, the strong interaction with the oxygen vacancy leads to a modification of the chemical activity of the particle. The vacancy site represents a special source of electrons which increases the

donor ability of the metal cluster, changing the ability to activate adsorbed molecules.

Therefore the oxygen vacancies are elusive, almost invisible, but crucial entities on the surface of oxides. While the vast majority of the regular surface sites may not be involved in chemical reactions, at least up to room temperature, the defect sites and in particular the oxygen vacancies are among the most reactive sites of the whole surface. The consequence is that adsorbed molecular species diffuse on the surface until they are blocked at the vacancy sites where they can be stabilized or converted into new chemical entities.

The oxygen vacancies can have also an important role in the oxide interfaces. In fact:

- it was proposed that the 2DEG at the n-type $SrTiO_3/LaAlO_3$ interface is caused by the presence of oxygen vacancies;
- it has been argued that the presence of native surface and subsurface point defects (such as oxygen vacancies), their concentration, and depth distribution can strongly affect the electronic properties and electrical response of metal-ZnO interfaces and Schottky barriers.

1.5 *ZnO*

1.5.1 Properties and device applications

The wide range of useful properties displayed by ZnO has been recognized for a long time. What has captured most of the attention in recent years is the fact that ZnO is a semiconductor with a direct band gap of 3.44 eV [90, 91], which in principle enables optoelectronic applications in the blue and UV regions of the spectrum. The prospect of such applications has been fueled by impressive progress in bulk-crystal [92, 93] as well as thin-film growth over the past few years [94, 95, 96]. A partial list of the properties of ZnO that distinguish it from other semiconductors or oxides or render it useful for applications includes:

- **Direct and wide band gap.** The band gap of ZnO is 3.44 eV at low temperatures and 3.37 eV at room temperature [97]. This enables applications in optoelectronics in the blue/UV region, including light-emitting diodes, laser diodes and photodetectors [98, 91]. Optically pumped lasing has been reported in ZnO platelets [99], thin films [100], clusters consisting of ZnO nanocrystals [101] and ZnO nanowires [102].

Reports on p–n homojunctions have recently appeared in the literature [103], but stability and reproducibility have not been established.

- **Large exciton binding energy.** The free-exciton binding energy in ZnO is 60 meV [99, 100]. This large exciton binding energy indicates that efficient excitonic emission in ZnO can persist at room temperature and higher [99, 100]. Since the oscillator strength of excitons is typically much larger than that of direct electron–hole transitions in direct gap semiconductors, the large exciton binding energy makes ZnO a promising material for optical devices that are based on excitonic effects.

- **Large piezoelectric constants.** In piezoelectric materials, an applied voltage generates a deformation in the crystal and vice versa. These materials are generally used as sensors, transducers and actuators. The low symmetry of the wurtzite crystal structure combined with a large electromechanical coupling in ZnO gives rise to strong piezoelectric and pyroelectric properties. Piezoelectric ZnO films with uniform thickness and orientation have been grown on a variety of substrates using different deposition techniques, including sol–gel process, spray pyrolysis, chemical vapor deposition, molecular-beam epitaxy and sputtering [104, 105].

- **Strong luminescence.** Due to a strong luminescence in the green–white region of the spectrum, ZnO is also a suitable material for phosphor applications. The emission spectrum has a peak at 495 nm and a very broad half-width of 0.4 eV. The n-type conductivity of ZnO makes it appropriate for applications in vacuum fluorescent displays and field emission displays. The origin of the luminescence center and the luminescence mechanism are not really understood, being frequently attributed to oxygen vacancies or zinc interstitials, without any clear evidence. These defects cannot emit in the green region, and it has been suggested that zinc vacancies are a more likely cause of the green luminescence. Zn vacancies are acceptors and likely to form in n-type ZnO.

- **Strong sensitivity of surface conductivity to the presence of adsorbed species.** The conductivity of ZnO thin films is very sensitive to the exposure of the surface to various gases. It can be used as a cheap smell sensor capable of detecting the freshness of foods and drinks, due to the high sensitivity to trimethylamine present in the odor. The mechanisms of the sensor action are poorly understood.

Recent experiments reveal the existence of a surface electron accumulation layer in vacuum annealed single crystals, which disappears upon exposure to ambient air [106, 107]. This layer may play a role in sensor action, as well. The presence of this conducting surface channel has been suggested to be related to some puzzling type-conversion effects observed when attempting to obtain p-type ZnO [106, 107].

- **Strong non-linear resistance of polycrystalline ZnO.** Commercially available ZnO varistors are made of semiconducting polycrystalline films with highly non-ohmic current-voltage characteristics. While this nonlinear resistance has often been attributed to grain boundaries, the microscopic mechanisms are still not fully understood and the effects of additives and microstructures, as well as their relation to degradation mechanisms, are still under debate.

- **Large non-linear optical coefficients.** ZnO crystals and, in particular, thin films exhibit second- and third-order non-linear optical behavior, suitable for non-linear optical devices. The linear and non-linear optical properties of ZnO depend on the crystallinity of the samples. ZnO films grown by laser deposition, reactive sputtering and spray pyrolysis show strong second-order non-linear response. Third-order non-linear response has recently been observed in ZnO nanocrystalline films [108]. The non-linear optical response in ZnO thin films is attractive for integrated non-linear optical devices.

- **High thermal conductivity.** This property makes ZnO useful as an additive (e.g. ZnO is added to rubber in order to increase the thermal conductivity of tires). It also increases the appeal of ZnO as a substrate for homoepitaxy or heteroepitaxy (e.g. for growth of GaN, which has a very similar lattice constant) [109]. High thermal conductivity translates into high efficiency of heat removal during device operation.

- **Amenability to wet chemical etching.** Semiconductor device fabrication processes greatly benefit from the amenability to low-temperature wet chemical etching. It has been reported that ZnO thin films can be etched with acidic, alkaline as well as mixture solutions. This possibility of low-temperature chemical etching adds great flexibility in the processing, designing and integration of electronic and optoelectronic devices.

- **Radiation hardness.** Radiation hardness is important for applications at high altitude or in space. It has been observed that ZnO

exhibits exceptionally high radiation hardness [110], even greater than that of GaN, the cause of which is still unknown.

1.5.2 Non-polar surfaces

ZnO crystallizes in the wurtzite structure (B4) at room temperature. The wurtzite morphology is characterized by four low-index surfaces, that is, the nonpolar prism $(10\bar{1}0)$ and $(11\bar{2}0)$ surfaces, along with the polar or basal (0001)-Zn and $(000\bar{1})$-O surfaces.

ZnO surfaces have attracted substantial attention in recent years because of the wide band gap semiconductor, where it finds a wide variety of applications such as catalysis and most recently nanomaterials. The structure and morphology of ZnO are decisive for the atomic-scale growth of nanomaterials. ZnO nanoparticles and nanorods/wires have been intensively studied for promising applications as gas sensors, photodetectors, and optoelectronic devices. However, before these interesting applications of ZnO can be addressed, a thorough understanding of the underlying ZnO surfaces is necessary. In particular there is a great interest for the non polar surfaces because nanostructures with different surface facets are employed but the $(10\bar{1}0)$ and $(11\bar{2}0)$ surfaces/facets are the most stable and abundant ones [32, 33].

The mixed-terminated $(10\bar{1}0)$-surface

The ZnO $(10\bar{1}0)$ mixed-terminated surface of zinc oxide is the energetically most favorable surface; SEM images recorded for ZnO powder particles reveal a dominance of this surface which forms the sides of the hexagonal columns, (Fig. 1.4).

Since this is a nonpolar surface no electrostatic instabilities as expected for the polar surfaces are present and the actual geometric structure of the surface should be similar to a bulk truncation. In accord with this expectation, previous works with LEED [111, 112, 113] and He atom scattering [114, 115] have not revealed any deviations from a surface periodicity expected on the basis of the bulk structure. The absence of an electrostatic instability for this non-polar also makes theoretical calculations possible in a rather straightforward fashion and a number of theoretical results have been reported for this ZnO $(10\bar{1}0)$ surface [114, 115, 116]. Several authors have succeeded in recording atomically resolved STM micrographs for this surface, see e.g. the work by Diebold and coworkers [117, 53] and by Yin *et al.* [114, 118].

A typical high resolution STM image recorded for the clean ZnO $(10\bar{1}0)$ surface is shown in Figure 1.5. The STM micrograph reproduced in Figure

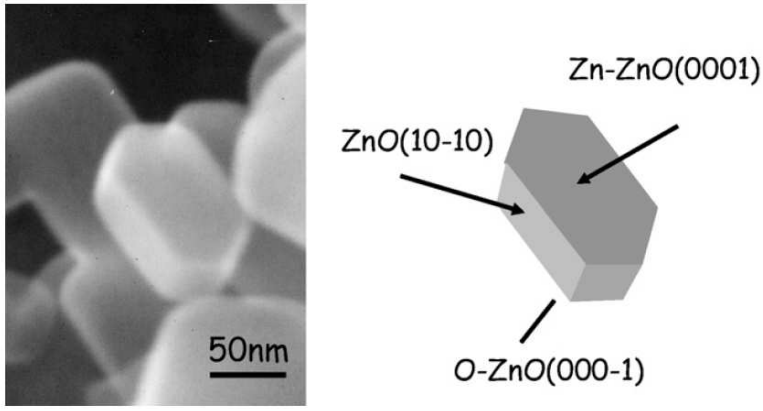

Figure 1.4: Left: SEM-image of ZnO powder particles. Right: schematic sketch showing the typical shape of ZnO powder particles, a hexagonal column with the top-face corresponding to the Zn-terminated Zn–ZnO surface and the bottom to the O-terminated O–ZnO surface. The six side faces are all equivalent and correspond to the mixed terminated ZnO $(10\bar{1}0)$ surface.

1.5a shows a corrugated terrace structure; about 10 different height levels are visible. The terraces are found to be elongated along the [0001] direction; Figure 1.5b shows a higher magnification image which makes it possible to investigate the local step structure. As evidenced by the line scan shown in Figure 1.5c the step height amounts to 0.28 nm, in good agreement with the value expected from the crystallographic bulk data, 0.281 nm. In Figure 1.5d it is shown a high resolution STM image where atomic resolution could be achieved. The bright spots in this empty-state image (negative tip voltage) are tentatively assigned to the Zn atoms.

This assignment is based on theoretical results for the electronic structure of the clean ZnO $(10\bar{1}0)$ surface which reveals that the electronic states closest to the Fermi energy, both occupied and unoccupied, are mainly of Zn 3d character [115].

The mixed-terminated $(11\bar{2}0)$-surface

This nonpolar surface has been the subject of a few studies only; the number of works reported for this termination is significantly smaller than for the other low Miller index surfaces of ZnO. We are not aware of an experimental study on the geometry relaxation on this surface using diffraction methods (LEED or GIXD). Recent STM and LEED studies [117, 53] were consistent with an essentially bulk-like termination of the surface. A high background

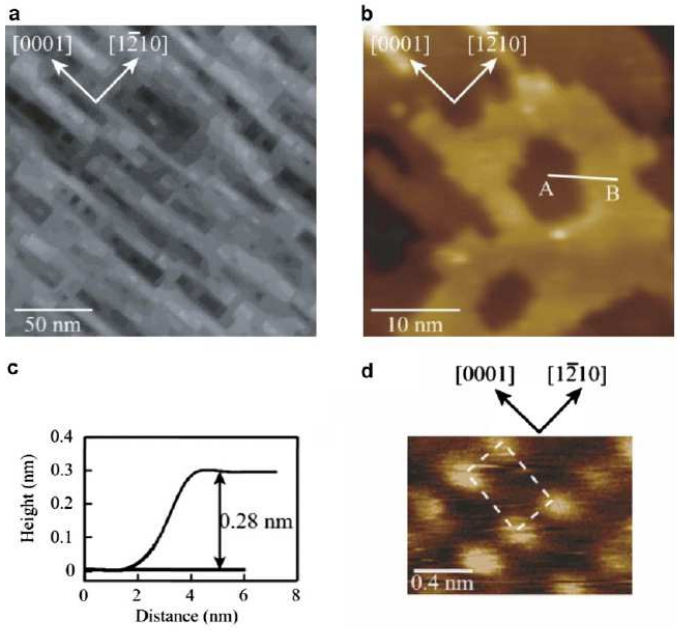

Figure 1.5: STM images recorded for a clean, mixed-terminated ZnO (10$\bar{1}$0) surface. The large scale image shown in (a), width 200 nm, was obtained at room temperature, images (b) and (d) were obtained at 380-400 K, tunneling parameters: 2.1 V, 1.3 nA in (a), 2.6 V, 0.4 nA in (b) and 0.7 V, 1.1 nA in (d); (c) line profile AB indicated in b. Figure taken from Yin *et al.* [118].

in LEED and a large surface roughness in STM were observed, which was interpreted in terms of the this surface orientation being rather unstable.

There are several theoretical studies which have been reported for this surface, see Meyer and Marx [119] for an overview of previous computational results. Basically, the DFT slab calculations reveal relaxations which are similar to those found for the ZnO (10$\bar{1}$0) surface. The most important changes with respect to the bulk-like structure are a 7.5° tilt of the Zn–O surface dimers and a reduction of the ZnO dimer bond length by about 6% [119]. In these calculations, the surface free energy of the ZnO(11$\bar{2}$0)-surface was found to be only slightly larger than for the ZnO (10$\bar{1}$0) surface, but significantly lower than for the two polar ZnO surfaces. The hypothesis quoted above as regards the poor structural quality of this surface being due to an instability [117, 53] could thus not be confirmed by the theoretical results.

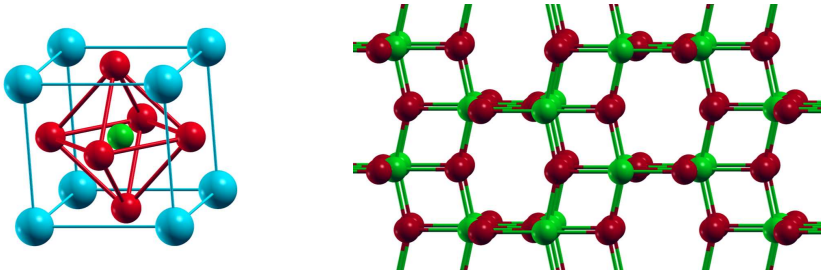

(a) (b)

Figure 1.6: (a) Perovskite structure and (b) anatase structure. Oxygen are red, strontium are blue and titanium atoms are green.

1.6 $SrTiO_3$–TiO_2 interface

One family of oxide materials that has received enormous amount of attention consists of compounds with chemical formula ABO_3 and crystallizes in the perovskite structure, shown in Figure 1.6(a).

The perovskite is characterized by a small cation, B, at the center of an octahedron of oxygen anions, with large cations, A, at the unit cell corners. The ideal cubic perovskite structure from Figure 1.6(a) is stable only within a very limited range of ionic radii and undergoes different types of symmetry-lowering distortions depending on the size of the A and B cations. The deviation from the ideal structure is often quantified through the Goldschmidt tolerance factor $t = (r_A + r_O)/\sqrt{2}(r_B + r_O)$ [120], which is equal to 1 when the ionic radii r_A, r_B and r_O are such that all the anions just touch the cations. For example, in $BaTiO_3$ the Ti^{4+} ions occupying sites B are too small for the oxygen octahedron ($t > 1$) and prefer to move off-center, generating an electric dipoles and giving rise to ferroelectricity. On the other hand, when A cation is too small, as in $BiFeO_3$, then $t < 1$. In this case the oxygen octahedra are too large and they must tilt to fit into the cell. Such tilting has a profound effect on magnetic and transport properties of perovskite oxides as it leads to reduction of B–O–B angle which diminishes the orbital overlap and superexchange interaction. In addition to ionic mismatch, the structural distortions in perovskite oxides can be also induced by orbitally degenerate electronic configuration that undergoes Jahn-Teller distortion as in the case for manganites (e.g. $LaMnO_3$).

1.6.1 $SrTiO_3$

An important example of a perovskite oxide is $SrTiO_3$. At room temperature it has a cubic structure as depicted in Figure 1.6(a) with an experimental lattice constant of 3.904 Å. As temperature is decreased below 105 K it undergoes a phase transition to tetragonal structure driven by tilting neighboring oxygen octahedra in opposite directions. $SrTiO_3$ has been thoroughly investigated during past decades and now high-quality single crystals of $SrTiO_3$ are freely available. The reason for the scientific interest in $SrTiO_3$ is that it is used as a standard substrate for depositing oxide materials. Indeed $SrTiO_3$ has a similar structure and lattice constant to many other important oxides allowing for their epitaxial growth. In addition, it is chemically inert and usually it does not interact with deposited materials. An important property of $SrTiO_3$ is that it can be grown on Si [121]. This provides a route to integrate oxide-based devices into microelectronic industry. $SrTiO_3$ has many attractive properties by itself. In its stoichiometric form it is a paraelectric insulator with rather large indirect band gap of 3.25 eV but by introducing oxygen vacancies it can be doped to a metallic or even superconducting state. The concentration of oxygen vacancies can be carefully controlled in single crystals or even in thin films. $SrTiO_3$ has also remarkable dielectric properties. It has a very large dielectric constant (several hundred at room temperature) making $SrTiO_3$ a good candidate for a gate in field effect transistors. Furthermore, $SrTiO_3$ can be driven into ferroelectric state by application of strain.

1.6.2 TiO_2

Titanium dioxide is a ceramic material, commonly known as titania. Although generally used as a white pigment or opacifier, titania can also be applied in enameling and catalysis. Three polymorphs of titanium dioxide exist: brookite, anatase, and rutile. All possess the same empirical chemistry, TiO_2, but each has a different crystal structure. Brookite has an orthorhombic crystal structure and spontaneously transforms to rutile around 750° C. Its mechanical properties are very similar to those of rutile, but it is the least common of the three phases and is rarely used commercially.

Anatase is a TiO_2 poly morph which is less stable than rutile, but more efficient than rutile for several applications, including catalysis [122], photocatalysis [123], and, especially, dye-sensitized solar cells. Anatase has a tetragonal crystal structure in which the Ti–O octahedra share four corners, as shown in Figure 1.6(b) and it has a band gap of 3.2 eV. In all its applications, surface properties are of major importance. However, while the

surfaces of rutile have been extensively investigated [123, 124], due to the limited availability of sufficiently large anatase single crystals the fundamental surface properties of this polymorph are still largely unexplored. Only very recently, thanks to improved sample preparation techniques, experimental studies of well defined anatase surfaces have started to appear.

1.6.3 Interface

As it has been said, the $SrTiO_3$ is used as substrate for many metal oxides. In particular films of TiO_2 are grown on $SrTiO_3$ (001) [59, 125]. Experimentally it is found that, when the TiO_2 films are deposited on $SrTiO_3$ (001) at $T = 1000°$ C, TiO_2 anatase is formed [126]. The stability of anatase in these conditions can be understood by examining the lattice constants and (001) planar structures of the $SrTiO_3$ and TiO_2 anatase. $SrTiO_3$ is cubic with $a = b = c = 3.904$ Å while TiO_2 anatase and rutile are tetragonal with $a = b = 3.784$ Å and $c = 9.515$ Å for the anatase and $a = b = 4.593$ Å and $c = 2.959$ Å for the rutile [126]. So, the in-piano lattice mismatch between $SrTiO_3$ (001) and TiO_2 rutile is 15%, while that between $SrTiO_3$ (001) and TiO_2 anatase is 3%. Moreover, by comparing the planar atomic configuration among $SrTiO_3$ (001), anatase TiO_2 (001) and rutile TiO_2 (001) planes, an important role may also be played from the similarities exhibited between the $SrTiO_3$ (001) and TiO_2 anatase (001).

In this scenario one expects that during the initial stage of film growth the arriving Ti and O atoms will tend to align themselves with the existing Ti and oxygen sublattices of the $SrTiO_3$ substrate. This process naturally leads to the formation of (001) anatase phase despite that it is not a thermodynamically favorable phase.

There are many works on this interface. In particular Ohta *et al.* [64] claimed that the $anatase/SrTiO_3$(001) interface exhibits 2D electron gas behaviour. In this experiment epitaxial films of TiO_2 were deposited on the (100)-face of $SrTiO_3$ single-crystal plates (10 mm × 10 mm × 0.5 mm) by PLD using a ceramic TiO_2 (rutile) target at 700° C in an oxygen atmosphere (oxygen pressure $P_{O_2} = 3 \times 10^{-3}$ Pa). Moreover Ohta *et al.* [64] also prepared an epitaxial layer of TiO_2 on a (100)-face of $LaAlO_3$ single-crystal substrate (10 mm × 10 mm × 0.5 mm) for comparison. Figure 1.8 shows the depth profiles for the $TiO_2/SrTiO_3$ and $TiO_2/LaAlO_3$ heterointerfaces. A steep peak with n_e of $\sim 1.4 \times 10^{21}$ cm^{-3} is seen at the heterointerface of $TiO_2/SrTiO_3$ The full-width at half-maximum of the peak is ~ 3 Å, which agrees well with the lattice parameter of $SrTiO_3$ ($a = 3.904$ Å), indicating that high-density carrier electrons ($n_e \sim 7.0 \times 10^{20}$ cm^{-3}) are localized within a unit cell layer thickness of $SrTiO_3$ at the heterointerface. On the other hand, the depth

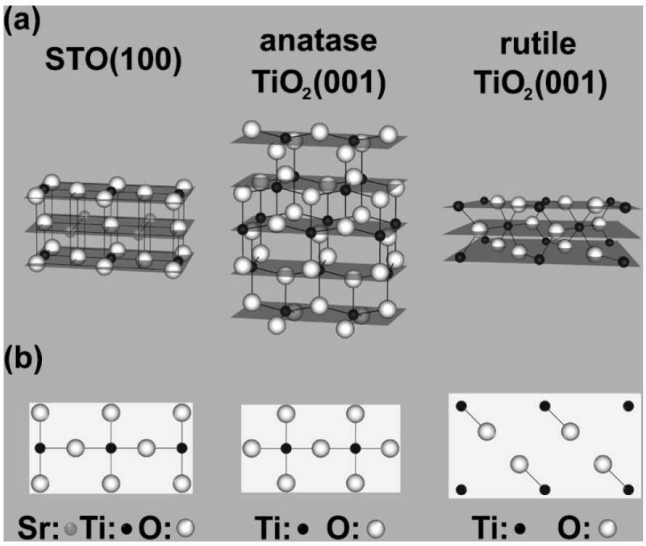

Figure 1.7: (a) The three-dimensional view of the crystallographic structures of $SrTiO_3$ (100), anatase TiO_2 (001), and rutile TiO_2 (001). (b) The (001) planar structure of $SrTiO_3$, anatase TiO_2, and rutile TiO_2.

profile of $TiO_2/LaAlO_3$ shows a constant n_e of $\sim 5 \times 10^{18}$ cm^{-3} over the whole depth, which corresponds well to the averaged n_e value evaluated by a conventional Hall voltage measurement. These observations clearly demonstrate that a 2DEG is formed at the heterointerface in $TiO_2/SrTiO_3$, but not in $TiO_2/LaAlO_3$. Ohta *et al.* [64] posited that the anatase films are inherently oxygen deficient and that oxygen diffuses from the $SrTiO_3$ substrate into the anatase film, leading to carrier confinement at the interface due to band bending and a space charge region in the substrate. Presumably, it is more difficult to extract oxygen from $LaAlO_3$, precluding band bending and carrier confinement at the $anatase/LaAlO_3$ interface.

Experimental details and band offset at $SrTiO_3 - TiO_2$ interface

After the work of Ohta *et al.* [64] there were many works on the $TiO_2/SrTiO_3$ interface aimed to investigate the electronic structure at these interfaces. In particular, Chambers *et al.* [65] have used high-energy resolution core-level and valence band X-ray photoemission spectroscopy (XPS) to determine the valence band offset (VBO) of $TiO_2/SrTiO_3$ interface.

In this section there is a brief description of the experimental details of the work of Chambers *et al.* [65]. In particular this section shows the experimental techniques used to grow anatase on the $SrTiO_3$ and to determine

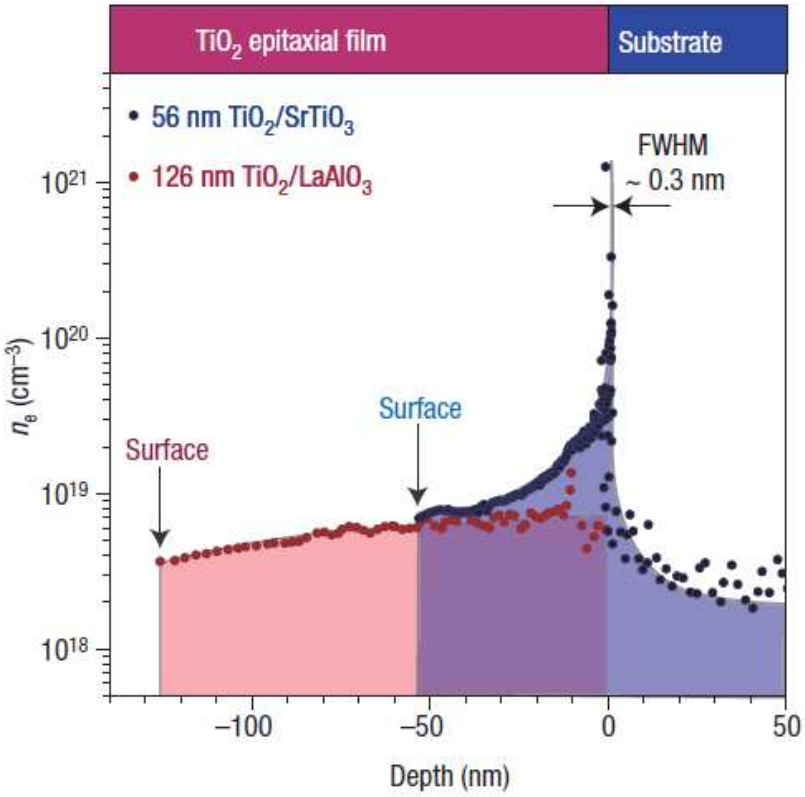

Figure 1.8: Depth profile of the carrier concentration around the interface between a 56-nm-thick TiO_2 epitaxial film and the $SrTiO_3$ substrate (blue). That for the interface between a 126-nm-thick epitaxial layer and insulating $LaAlO_3$ layer is also plotted for comparison (red). An intense carrier-concentration peak ($n_e \sim 1.4 \times 10^{21}$ cm^{-3}) with a full-width at half-maximum of ~ 3 Å is seen at the $TiO_2/SrTiO_3$ heterointerface. Figure taken from Ohta *et al.* [64].

the valence band offset (VBO).

In the work of Chambers *et al.* [65] all films were grown using MBE, with and without activated oxygen. The Ti atom beam was generated using a high-temperature effusion cell. The substrates consisted of undoped and Nb-doped (0.02 at.%) $SrTiO_3$(001). Each substrate was etched in buffered HF and annealed in flowing O_2 at 1 atm at 950° C for 8 h. This etch dissolves SrO terraces and the oxygen anneal results in mass transport of the nano- and mesoscale, discontinuous TiO_2 terraces, resulting in an atomically flat and exclusively TiO_2 terminated surface with a minimum step height of 4 Å [127]. This treatment leaves some residual fluorine on the surface which is

not removed by annealing.

Following sonication in acetone and isopropanol, along with UV/ozone cleaning on the bench, the substrates were loaded into the MBE chamber and subjected to one of three different treatments. The first (preparation 1) consisted of exposure to activated oxygen from the electron cyclotron resonance (ECR) plasma at a chamber pressure of 2×10^{-5} Torr for 1 h to rid the surface of adventitious carbon. However, the residual F is not removed by the procedure. The second (preparation 2) consisted of sputtering very briefly with 1 kV Ar ions at a glancing angle of incidence to rid the surface of F, followed by annealing in activated oxygen at 2×10^{-5} Torr and 550° C for 1 h to attempt removal of surface defects created by Ar ion sputtering. This surface had no detectable impurities of any kind by XPS. The third (preparation 3) also included a brief Ar ion sputter to rid the surface of F, followed by a second oxygen tube furnace anneal, as described above. This substrate was then exposed solvent and UV/ozone cleaned on the bench and cleaning with activated oxygen in the MBE chamber. The motivation behind this treatment was to give the surface an extensive oxygen anneal in order to more fully heal defects created by Ar ion sputtering. This method resulted $\sim$1 at.% F in the anion sublattice, presumably because F diffused from the sides and back of the substrate to the growth surface during the second tube furnace anneal.

Three series of films were grown on substrates prepared by the three methods. All films were grown at a substrate temperature of $575 \pm 50°$ C. The growths were carried out under oxygen rich conditions, with a combined O_2 and O to Ti flux ratio of $\sim$ 250. Growths were carried out with and without activated oxygen. Oxygen activation, leading to a mix of O and O_2, was not found to be needed to fully oxidize all incoming Ti. The growth rate was $\sim$ 0.5 ML TiO_2 anatase per minute. Following growth, the films were transferred under ultrahigh vacuum to an appended XPS chamber. All spectra used to determine band offsets were measured with a electron pass energy and a entrance slit width of 150 eV and 1.5 mm, respectively, resulting in a total energy resolution of 0.46 eV. None of the films grown on n-$SrTiO_3$ exhibited any charging artifacts. The binding energy scale was calibrated using the Au $4f_{7/2}$ core-level peak from a Au foil, which has a binding energy of 84.00 eV.

The valence band (VB) spectra of anatase and $SrTiO_3$ are somewhat similar in appearance. Both consist of a broad two-lobed structure with peaks at 4-5 and 7-8 eV and similar overall widths. While both lobes originate from states of mixed metal and oxygen character, the VB is mostly O 2p like. Figure 1.9 shows the VB spectrum for pure $SrTiO_3$ using preparation 3, as well as those for a thick-film of epitaxial anatase (top spectrum), and

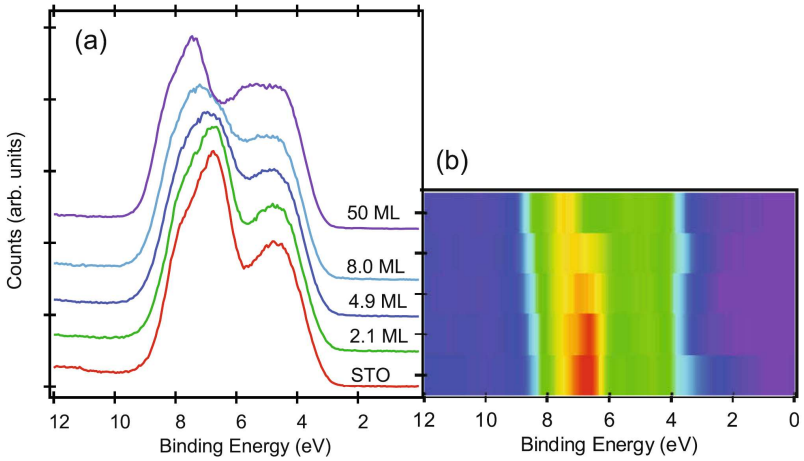

Figure 1.9: X-ray excited band photoemission spectra for epitaxial TiO_2 anatase on $SrTiO_3$(001) (series 3) shown conventionally (left) and as intensity contour plots (right). Differences in band bending have been removed by aligning the binding energy scales for all specimens to that of $SrTiO_3$, which exhibits a near flat-band condition. Figure taken from Chambers *et al.* [65].

representative anatase epitaxial films of intermediate thickness grown on the same substrate (growth series 3, using substrate preparation method 3). Differences in band bending have been removed from Figure 1.9 by aligning the binding energy scales of all spectra to that of the substrate. This was done in order to facilitate visual inspection of the overall VB width as a function of anatase film thickness.

About the quantitative determination of the valence band offsets, from the raw VB spectra (Fig. 1.9), it can be noted that the overall width of the VB is slightly larger for thick-film, bulk-like TiO_2(001) anatase than it is for clean $SrTiO_3$(001), as seen by comparing the top (anatase) and bottom ($SrTiO_3$) intensity contour plots on the right side of the figure. Moreover, the VB width increases slowly with anatase thickness, gradually approaching that of thick-film anatase. This result is qualitatively consistent with expectations if the VBO (ΔE_v) at the interface is very small or zero. However, it is necessary to accurately measure ΔE_v, which it is defined as the difference in VBM between the anatase and the $SrTiO_3$ at the interface ($\Delta E_v = E_v^{ana} - E_v^{SrTiO_3}$). For heterojunctions with at least one unique element in each material, determining ΔE_v from a combination of core levels and valence band spectra is straightforward [128, 129, 130, 131]. In this case, CL binding energies for at least one unique element from each material are

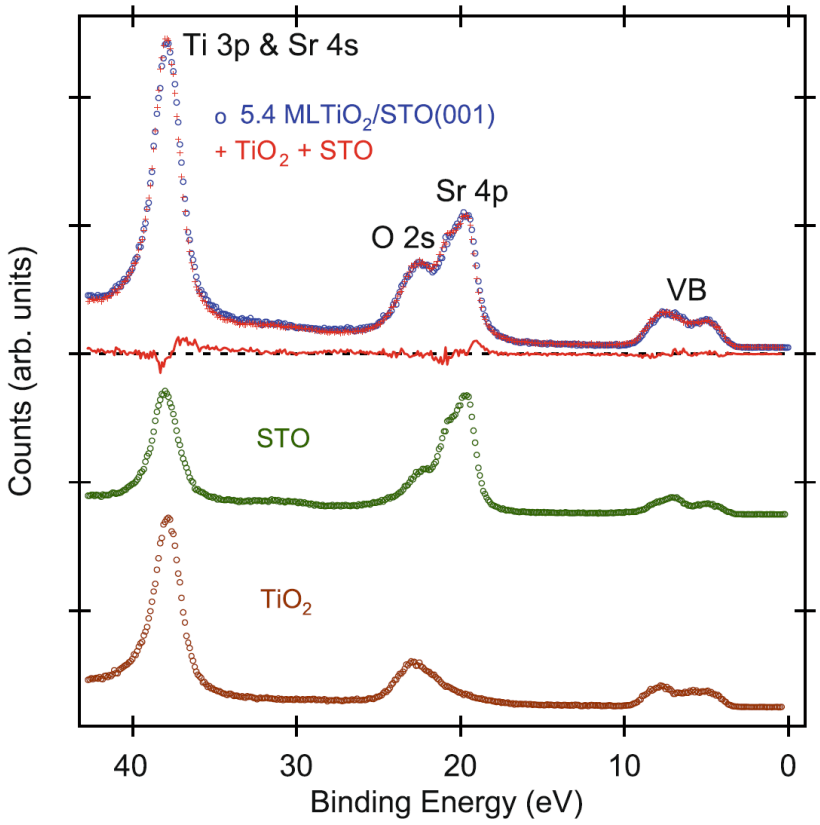

Figure 1.10: Shallow core-level spectra for 5.4 ML TiO_2 anatase on $SrTiO_3$(001) (preparation 1), along with simulated spectrum generated by shifting and weighting reference spectra for pure $SrTiO_3$ and TiO_2 to optimize the fit. The residuals are shown below the simulated and actual spectra. Figure taken from Chambers *et al.* [65].

referenced to E_v for pure phases of the materials. Then, these quantities are combined with the difference in core levels (CL) binding energies for the actual heterojunction to yield ΔE_v at the interface. In the present case, this approach cannot be used because anatase does not contain an element not also found in $SrTiO_3$. Therefore, a more elaborate procedure must be used. To this end, the shallow CL and VB spectra are measured with high-energy resolution from 0 to $\sim$ 50 eV binding energy for each interface, a thick-film anatase which simulates a bulk crystal, and each $SrTiO_3$ substrate [65]. The next step is to attenuate the intensity and shift the binding energy scale in the pure $SrTiO_3$ spectrum such the Sr CL peak areas and energies match those found in the heterojunction spectrum.

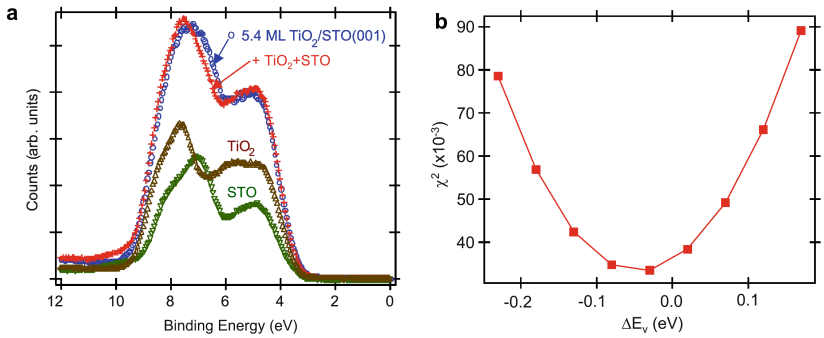

Figure 1.11: (a) X-ray excited valence band spectra for 5.4 ML TiO_2 anatase on $SrTiO_3(001)$ (preparation 1), along with a simulated spectrum generated by shifting and weighting spectra for pure $SrTiO_3$ and TiO_2 to optimize the fit and minimize χ^2. The simulation is shown for $\Delta E_v = -0.03$ eV. (b) The dependence of χ^2 on valence band offset. Figure taken from Chambers *et al.* [65].

Then the same step is carried out for the thick-film anatase spectrum, using the Ti 3p peak for alignment. The results of this procedure are shown in Figure 1.10 for a representative heterojunction, 5.4 ML of anatase grown on $SrTiO_3$ with preparation method 1 [65]. Summing the two shifted and attenuated spectra for pure $SrTiO_3$ and anatase yields a simulated heterojunction spectrum (designated "$TiO_2 + SrTiO_3$" in Figure 1.10) that matches that of the actual heterojunction rather well, as seen in the residuals. The magnitudes of the binding energy shifts applied to the $SrTiO_3$ and anatase spectra yield an initial determination of ΔE_v. In order to complete the analysis, the same attenuation factors and energy shifts are applied to VB spectra for pure anatase and $SrTiO_3$ measured with excellent statistics. Chambers *et al.* [65] then systematically shift either the $SrTiO_3$ or the thick-film anatase VB spectrum (whichever is less intense) from +0.3 to −0.3 eV in 0.05 eV increments from the initial offset value determined as described above. For each of these shifted spectra, it is fitted the sum of the thick-film anatase and $SrTiO_3$ spectra to the experimental heterojunction spectrum and it is computed a χ^2 value. Here it is defined the χ^2 as $\sum_i [I_{expt}(E_i) - I_{sim}(E_i)]^2 / I_{expt}(E)$, where $I_{expt}(E_i)$ and $I_{sim}(E_i)$ are the experimental and simulated heterojunction spectral intensities, respectively, and the sum is over all VB energies.

The results are shown in Figure 1.11 for a 5.4 ML film. This analysis is typical and therefore representative of all thicknesses investigated. The ΔE_v for the optimized fit is −0.03 eV for this particular film. The minimum in χ^2 found by this method is consistently within 0.1 eV of that found by

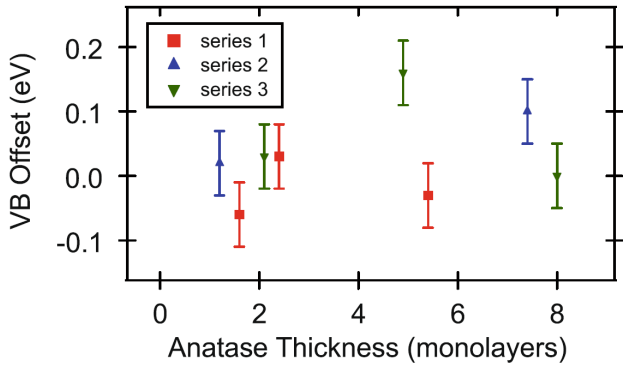

Figure 1.12: Valence band offset as a function of anatase film thickness for the three different growth series. Figure taken from Chambers *et al.* [65].

alignment of the CLs. Based on the clear minima exhibited by the χ^2 curves, it is assigned an experimental uncertainty of ± 0.05 eV to each individual determination. The ΔE_v values for film thicknesses between 1.2 and 8.0 ML are shown in Figure 1.12.

The values are near zero for all anatase thicknesses, independent of substrate preparation method. Moreover, because the band gaps are the same for the two materials, ΔE_c is also quite small. The sensitivity of this method to the value of ΔE_v depends on film thickness. There is maximum sensitivity when the film thickness is such that the anatase and $SrTiO_3$ VB contributions are of approximately equal weight. In this case, an energy shift in one spectrum relative to the other results in the largest change in the sum of the two spectra.

These near zero band offset values are significant for fundamental photochemistry studies using this heterojunction in that neither photogenerated electrons nor holes are expected to become trapped in the substrate. Rather, both kinds of charged particles can freely diffuse to the surface and drive heterogeneous photochemical reactions.

Chapter 2

Model

The development in computational physics, both in efficiency of the algorithms and the possibility to use parallel computers, now enables the study of properties in increasingly complex systems. The refinements of the methods have also increased the accuracy making it possible to e.g. discriminate between the adsorption energies of different bonding sites for a molecule on a surface or to determine the lowest energy structure for a grain boundary [132, 133]. Electron structure calculations can be used to analyze the conduction properties of materials and the band structure gives information about electron states due to impurities, surfaces or interfaces. Many interesting physical phenomena are connected to these properties and some are discussed in the present thesis. The advantage of first principles calculations is that they provide unbiased microscopic information that is not available from other sources. These methods therefore give important contributions to the understanding of complex phenomena where experiments and simple models aren't sufficient.

The present chapter summarizes the fundamental aspects of the theoretical framework for the study of the structural and electronic properties of the nanostructures investigated in this thesis.

2.1 Density Functional Theory

There are numerous approaches at different levels of sophistication to calculate the wavefunctions and eigenstates for electrons in a solid material. The Nearly Free Electron (NFE) model [134] and the tight-binding method [135] are two simple wave function methods which don't treat the electron-electron interaction explicitly. Instead the Hartree equations takes the electrostatic interaction between the electrons into account. The Hartree-Fock methods

[134] give good results for systems where the exchange effects are more important than correlation effects and Hartree-Fock calculations have been used widely, particularly in the chemist community.

Going beyond the Hartree-Fock approximation to include the correlation effects adds a considerable complexity to problem and treating the correlation effects exactly in a realistic material is impossible. The Density functional theory (DFT) is however a very convenient method to treat the correlation effects in a mean field manor.

The method, introduced in the 60s by Hohenberg and Kohn [136, 137], allows to recast the electronic Hamiltonian in a more practical, self-consistent, and one-electron formulation which is based on an exact result even if resembling a Hartree mean-field calculation. In the DFT the ground state density of a bound system of interacting electrons in an external potential is proved to uniquely determine the potential. Hence, the ground state values of all the observables are uniquely determined by the exact ground state electron density. This result busts the possibility to develop an efficient method to study systems with a huge number of particles because we are left with the search of just one fundamental function (the electronic total density), depending on three total variables (the spatial coordinates), from which all the informations of interest can be extracted. This squeezes the much far complicated computational effort to solve the Schrödinger equations depending on all the electronic variables. There is only one problem still to be overcome which is an exact expression for the exchange-correlation functional, whose knowledge would give a complete exact self-consistent theory. Many formulations have been developed to approximate this term and the one used in this thesis will be discussed, namely the generalized gradient approximation. More practical approximations are needed to use the DFT in real calculations which however go beyond the theory in itself, as the basis representation of the functions. In this thesis we chose to use a plane-wave based code which is suited for extended crystal materials, but it brings a simple way to improve and control the accuracy of the calculations, that is the solely number of plane waves of the basis set. At last, the pseudopotential approximation allows to scale down the computational cost thanks to the fact the chemical bonds in real materials are essentially determined by the valence electron.

2.1.1 The Hohenberg-Kohn Energy Functional

The original formulation of the Density Functional Theory (DFT) [137] was considering an electron gas in an time-independent external potential. The Hamiltonian for the electrons has three contributions in such case: the kinetic energy, $\hat{T}$,

$$\hat{T} = \frac{\hbar^2}{2m} \int \nabla\psi^\dagger(\mathbf{r}) \nabla\psi(\mathbf{r}) d\mathbf{r} \tag{2.1}$$

the electron-electron interaction, $\hat{V}^{ee}$

$$\hat{V}^{ee} = \frac{e^2}{2} \int \frac{\psi^\dagger(\mathbf{r})\psi^\dagger(\mathbf{r}')\psi(\mathbf{r}')\psi(\mathbf{r}) d\mathbf{r} d\mathbf{r}'}{\mid \mathbf{r} - \mathbf{r}' \mid} \tag{2.2}$$

and the electron-ion interaction, $\hat{V}^{eI}$

$$\hat{V}^{eI} = \int \psi^\dagger(\mathbf{r}) v(\mathbf{r}) \psi(\mathbf{r}) d\mathbf{r} \tag{2.3}$$

where $\psi(\mathbf{r})$ and $\psi^\dagger(\mathbf{r})$ are electron annihilation and creation field operators and $v(\mathbf{r})$ is the external potential from the ions in the material.

The total energy of the ground state is obtained from the variation principle by minimizing the energy with respect to the electron wave function of the system $|\Psi\rangle$

$$E_0 = \langle \Psi_0 | \hat{H} | \Psi_0 \rangle \leq \langle \Psi | \hat{T} + \hat{V}^{ee} + \hat{V}^{eI} | \Psi \rangle \tag{2.4}$$

Hohenberg and Kohn [136] found that all the individual terms in the expression for the total energy in Eq. (2.8) could be written as a functional of the electron density according to the following formulas: the kinetic energy for the electrons

$$E_{kin} = \frac{\hbar^2}{2m} \int \langle \Psi | \nabla\psi^\dagger(\mathbf{r}) \nabla\psi(\mathbf{r}) | \Psi \rangle d\mathbf{r} = -\frac{\hbar^2}{2m} \int \nabla^2 n(\mathbf{r}) d\mathbf{r} \tag{2.5}$$

the contribution from the electron-ion attraction

$$E_{eI} = \langle \Psi | \int \psi^\dagger(\mathbf{r}) v(\mathbf{r}) \psi(\mathbf{r}) d\mathbf{r} | \Psi \rangle = \int v(\mathbf{r}) n(\mathbf{r}) d\mathbf{r} \tag{2.6}$$

and the electron-electron interaction which is divided into the direct Coulomb interaction called the Hartree term and the Exchange and Correlation term

$$\begin{aligned} E_{ee} &= \frac{e^2}{2} \int \frac{\langle \Psi | \psi^\dagger(\mathbf{r})\psi^\dagger(\mathbf{r}')\psi(\mathbf{r}')\psi(\mathbf{r}) | \Psi \rangle}{|\mathbf{r} - \mathbf{r}'|} d\mathbf{r} d\mathbf{r}' \\ &= \frac{e^2}{2} \int \frac{n(\mathbf{r}) n(\mathbf{r}')}{|\mathbf{r} - \mathbf{r}'|} d\mathbf{r} d\mathbf{r}' + \frac{e^2}{2} \int \frac{n_2(\mathbf{r}, \mathbf{r}'; \mathbf{r}, \mathbf{r}') - n(\mathbf{r}) n(\mathbf{r}')}{|\mathbf{r} - \mathbf{r}'|} d\mathbf{r} d\mathbf{r}' \\ &= E_H + E_{xc} \end{aligned} \tag{2.7}$$

where $n_2(\mathbf{r}, \mathbf{r}'; \mathbf{r}, \mathbf{r}')$ is the two-particle density giving the correlation effects.

The Hohenberg-Kohn theorem [136] states that i) the total energy of the system is a functional of the electron density in the system

$$\begin{aligned} E[n(\mathbf{r})] &= E_{kin} + E_{eI} + E_H + E_{xc} \\ &= -\frac{\hbar^2}{2m}\int \nabla^2 n(\mathbf{r}) d\mathbf{r} + \int v(\mathbf{r}) n(\mathbf{r}) d\mathbf{r} + \frac{e^2}{2}\int \frac{n(\mathbf{r}) n(\mathbf{r}')}{|\mathbf{r}-\mathbf{r}'|} d\mathbf{r} d\mathbf{r}' + \\ &+ \frac{e^2}{2}\int \frac{n_2(\mathbf{r}, \mathbf{r}'; \mathbf{r}, \mathbf{r}') - n(\mathbf{r}) n(\mathbf{r}')}{|\mathbf{r}-\mathbf{r}'|} d\mathbf{r} d\mathbf{r}' \end{aligned} \tag{2.8}$$

and that ii) the ground state electron density gives the lowest total energy.

$$E_0 = E[n_0(\mathbf{r})] \leq E[n(\mathbf{r})] \tag{2.9}$$

It should be mentioned that the expression in Eq. (2.8) only considers the electronic contribution to the total energy and it needs to be complemented by the Madelung energy in order to obtain the full expression for the total energy of the material:

$$E_M = \frac{1}{2}\sum_{i \neq j} \frac{q_i q_j}{4\pi\epsilon_0 |\mathbf{R}_i - \mathbf{R}_j|} \tag{2.10}$$

where q_i are the ionic charges. The Madelung energy represents the ion-ion interaction at absolute zero and it is a sum over the mutual coulomb interactions between the ions in the crystal.

2.1.2 The Kohn-Sham Equations

Kohn and Sham [137] later showed that the total energy functional for the interacting many-particle system can be transformed into a set of one-particle equations, called the Kohn-Sham equations. This result was obtained by observing that minimizing the energy functional in Eq. (2.8) with respect to the electron density gives the Lagrange equation

$$\begin{aligned} &\int [v(\mathbf{r})\delta n(\mathbf{r}) + e^2 \int \frac{n(\mathbf{r}')\delta n(\mathbf{r}) d\mathbf{r}'}{|\mathbf{r}-\mathbf{r}'|} - \frac{\hbar^2}{2m}\nabla^2 n(\mathbf{r})\delta n(\mathbf{r}) + \\ &+\delta(n(\mathbf{r})\epsilon_{xc}[n(\mathbf{r})])] d\mathbf{r} = \int \lambda \delta n(\mathbf{r}) d\mathbf{r} \end{aligned} \tag{2.11}$$

This equation has the same form as a Schrödinger equation for a set of non-interaction electrons which moves in an effective potential V_{eff}. This effective one electron potential

$$V_{eff}(\mathbf{r}) = v(\mathbf{r}) + \int \frac{n(\mathbf{r}')d\mathbf{r}'}{|\mathbf{r} - \mathbf{r}'|} + \mu_{xc}(\mathbf{r}) \tag{2.12}$$

has a contributions from the ion-electron interaction, while the electron-electron interaction is divided into the Hartree term and the exchange and correlation potential $\mu_{xc}(\mathbf{r})$.

The problem of finding the ground state of an interacting many particle system is therefore mapped into a mean field problem where non-interacting electrons are moving in an effective potential set up by all electrons in the material. The resulting Kohn-Sham equations

$$\left[-\frac{\hbar^2}{2m}\nabla^2 + V_{eff}(\mathbf{r})\right]\psi_i = \epsilon_i\psi_i \tag{2.13}$$

are solved self-consistently and the ground state electron density is determined by the one-electron wave functions, ψ_i, as

$$n(\mathbf{r}) = \langle\Psi|\psi^\dagger(\mathbf{r})\psi(\mathbf{r})|\Psi\rangle = \sum_i |\psi_i|^2 \tag{2.14}$$

2.1.3 The self-consistent scheme

The self-consistent scheme is an iterative process to obtain the correct electron density which minimizes the total energy of the system. This is achieved by assigning trail wave functions which are used to calculate the electron density $n(\mathbf{r})$, by Eq. (2.14). $n(\mathbf{r})$ is used to calculate V_{eff} by Eq. (2.12) and V_{eff} is then inserted in the Kohn-Sham equations.

New wave functions are obtained by solving the Kohn-Sham equations and the procedure is repeated until convergence is achieved between the input and output wavefunctions from the Kohn-Sham wave functions. The sum over the occupied one-electron energies ϵ_i have to be corrected with a Coulomb and an exchange-correlation term to give the correct total energy

$$E[n(\mathbf{r})] = \sum_i \epsilon_i - \frac{e^2}{2}\int \frac{n(\mathbf{r})n(\mathbf{r}')}{|\mathbf{r} - \mathbf{r}'|}d\mathbf{r}d\mathbf{r}' + e^2\int n(\mathbf{r})[\epsilon_{xc}[n(\mathbf{r})] - \mu_{xc}(n(\mathbf{r}))]d\mathbf{r} \tag{2.15}$$

2.2 The Exchange-Correlation functional

The DFT is still exactly defined up to this point but its practical use depends on an explicit definition of the exchange-correlation energy, which is currently unknown. Therefore the exchange-correlation functional is most often approximated by a closed function expression and the credibility of the DFT calculation relay heavily on the accuracy of these approximations.

The simplest approximation which has had a tremendous success is the Local Density Approximation (LDA) [136, 137]. This approximation assumes that the exchange-correlation energy at a point is equivalent to the value for a homogeneous electron gas having the same electron density, $\epsilon_{xc}^{LDA}[n(\mathbf{r})] = \epsilon_{xc}^{hom}(n(\mathbf{r}))$. The exchange-correlation energy of the homogeneous electron gas has been calculated by Ceperley and Alder [138] for different electron densities. This data has been used by Perdew and Zunger [139] to parameterize a LDA exchange-correlation energy density as a function of the electron density which has been widely used.

The LDA exchange-correlation energy is then the expectation value of the exchange-correlation function weighted by the electron density

$$E_{xc}^{LDA}[n(\mathbf{r})] = \int \epsilon_{xc}^{hom}[n(\mathbf{r})]n(\mathbf{r})d\mathbf{r} \tag{2.16}$$

The LDA approximation works well for slowly varying electron densities in for instance bulk materials. One reason for the success of LDA in describing bulk properties is that the LDA expression fulfill the sum rule for the exchange-correlation hole located around each electron.

However, when the electron density varies rapidly as in molecules, at surfaces or for strongly correlated electron systems as ionic semiconductors LDA fails miserably. A well known problem is the underestimation of the size of the band gap in semiconductors.

In a sense, LDA can be viewed as the zeroth order term in a Taylor expansion of the exchange-correlation energy in terms of the electron density. Therefore an improvement over the LDA is given by considering the dependence of the exchange-correlation energy also on gradients of the density. This was proposed by Hohenberg, Kohn and Sham [136, 137], but the first formulation of the Gradient Expansion Approximation (GEA) did not improve upon the results of LDA. Later works by Langreth and Mehl [140], Perdew [141] and Becke [142] evolved into the Generalized Gradient Approximation (GGA). The kernel of the GGA exchange-correlation functional is a function of both the electron density and the gradients of the electron density in contrast to the GEA

$$E_{xc}^{GGA} = \int \epsilon(n(\mathbf{r}))n(\mathbf{r})d\mathbf{r} + \int f_{xc}(n(\mathbf{r}), |\nabla n(\mathbf{r})|)n(\mathbf{r})d\mathbf{r} \tag{2.17}$$

where f_{xc} is a function of the two independent variables $n(\mathbf{r})$ and $|\nabla n(\mathbf{r})|$. GGA is found to improve the binding energy estimates and the description of more inhomogeneous materials, giving reliable results also in some cases where LDA completely fails.

There has been several alternative versions of GGA-functionals presented through the years [143, 144, 145]. The PW-91 version of GGA by Perdew and Wang [143] is a parametrization of a numerical calculation of exchange-correlation energy and the derivation of the PW-91 version of GGA focused on the long range properties of the exchange-correlation hole.

Perdew *et al.* [143] also suggested a simplified version called the PBE-GGA, which focused on the the most important physical properties of exchange and correlation. This made the derivation more transparent than the derivation of the PW-91 version and the PBE-GGA has also shown improvements in the results for atoms and molecules compared to LDA and PW-91 GGA. The PBE-GGA and PW-91 GGA functionals have been used throughout the calculations of this thesis.

2.3 The Pseudopotential approximation

The electrons in a solid are divided into core electrons and valence electrons. The core electrons are localized around the nucleus in closed shells while the valence electrons take part in the bonding between atoms. The valence electrons determine the chemical and transport properties of the material and they are consequently the most interesting electrons to study. The core electrons screen the charge of the nuclei such that the valence electrons experience a smoother potential in the core region than the bare Coulomb potential. The pseudopotential approximation exploits this fact by considering that the valence electrons are moving in a pseudo potential, formed by bare the nuclei potential screened by the core electrons.

The theory of the pseudopotential began as an extension of the Orthogonalized Plane Wave method (OPW) [146] when it was noticed that it was hard to describe the rapid oscillations in the wave function near the core by a limited number of plane waves. The modern theory of first principles pseudopotentials was introduced by Hamann, Schuter and Chiang (HSC) [147]. They suggested a procedure to generate the pseudopotential based on an all-electron calculation of the potential and wavefunctions of the atom. Four

constraints were proposed to ensure that the pseudopotential has appropriate scattering properties and give the correct eigenvalues.

The pseudo potential was assigned to be smooth in the core region and to be equal to the all-electron potential outside a cut-off radius. This would ensure that the pseudo wave functions are smoother than the all-electron wave functions in the core region, but still have the correct chemical properties because they are equal to the all-electron wave functions outside the core region

$$\psi^{AE}(r) = \phi^{PsP}(r), r > r_c \tag{2.18}$$

The eigenvalues of the pseudopotential should reproduce the eigenvalues of the atom in the reference configuration.

$$\epsilon_i^{AE} = \epsilon_i^{PsP} \tag{2.19}$$

The pseudopotential was constructed to be norm conserving, which means that the radial integral of the pseudo charge density will give the same total charge inside the cut-off radius as the all-electron charge.

$$\int_0^{r_c} |\psi^{AE}(r)|^2 r^2 dr = \int_0^{r_c} |\phi^{PsP}(r)|^2 r^2 dr \tag{2.20}$$

The norm conservation constraint guarantees that the electrostatic potential outside the pseudopotential agrees with the all-electron potential. The logarithmic derivative of the pseudopotential and the all-electron potential at the cut-off radius should agree.

$$\begin{aligned} 2\pi \left[(r\phi^{PsP})^2 \frac{d}{d\epsilon} \frac{d}{dr} ln(\psi^{PsP}) \right] &= 2\pi \left[(r\psi^{AE})^2 \frac{d}{d\epsilon} \frac{d}{dr} ln(\psi^{AE}) \right] \\ &= 4\pi \int_0^{r_c} |\psi^{AE}|^2 r^2 dr \end{aligned} \tag{2.21}$$

The logarithmic derivative is connected to the phase-shift produced by a scattering potential which secured that the scattering properties of the pseudopotential would be equal to the all-electron potential.

The HSC pseudopotential is a semi-local pseudopotential. Kleinman and Bylander (KB) [148] suggested a fully non-local pseudopotential which couples different states and is capable of scattering the electron from one state to another. The non-local part of the KB pseudopotential has the form

$$\hat{V}_{NL}^{KB} = \sum_{lm} V_{lm} |\Phi_{lm}\rangle \langle \Phi_{lm}| \tag{2.22}$$

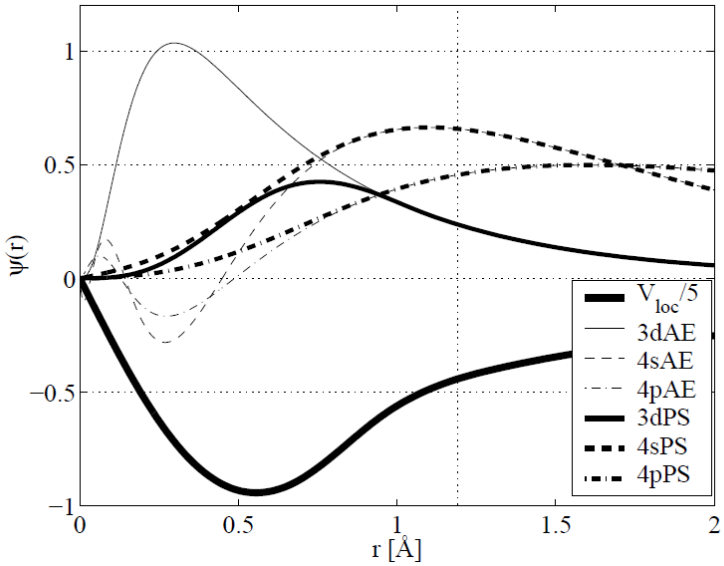

Figure 2.1: The local part of the pseudopotential V_{loc} together with the all-electron and ultrasoft wave functions for the Zn-pseudopotential. Note that V_{loc} is divided by 5 to get similar amplitude as the wavefunctions. The vertical dotted line indicates the cut-off radius r_c.

where $|\Phi_{lm}\rangle$ are the projectors and V_{lm} is scattering amplitude. The norm conserving pseudopotentials have been further by introducing more constraints to improve the accuracy and achieve smoother pseudopotentials. The smoothness of the pseudopotential is essential in plane wave calculations to reduce the number of expansion coefficients. The wave function has the strongest variation in the core region and if it is possible to decrease these oscillations, less coefficient are required in the expansion of the wave function. Troullier and Martins [149] proposed to use higher order derivatives at the cut-off radius to improve the smoothness of the potential. Their method of construction pseudopotentials has been widely used.

2.3.1 The Ultrasoft Pseudopotential

An additional step in the development of even softer pseudopotentials was taken by Vanderbilt when he introduced the concept of ultrasoft pseudopotentials [150]. The general idea was to relax the norm conservation constraint on the pseudo wave function to make them even softer. He claimed that it was sufficient to match the logarithmic derivatives at a diagnostic radius to secure the scattering properties of the pseudopotential. The charge deficit in

the core region is compensated by an augmentation charge defined as

$$Q_{nm}(\mathbf{r}) = \psi_n^{\dagger^{AE}}(\mathbf{r})\psi_m^{AE}(\mathbf{r}) - \phi_n^{\dagger^{US}}(\mathbf{r})\phi_m^{US}(\mathbf{r}) \tag{2.23}$$

The idea behind the ultrasoft pseudopotential is in a sense similar to the OPW method, because the Kohn-Sham wave function is divided into a soft delocalized contribution ϕ_m^{US} and a rapidly oscillating augmentation charge localized in the core region. A comparison between the ultrasoft and the all-electron wave functions for Zn is shown in Figure 2.1. The expression for the charge density $n(\mathbf{r})$ in Eq. (2.14) has to be complemented by the augmentation charge to restore the physical charge density

$$n(\mathbf{r}) = \sum_i \left[|\phi_i^{US}(\mathbf{r})|^2 + \sum_{nm,I} Q_{nm}^I(\mathbf{r}) \langle \phi_i^{US} | \beta_n^I \rangle \langle \beta_m^I | \phi_i^{US} \rangle \right] \tag{2.24}$$

The ultrasoft pseudopotential uses the Kleinman-Bylander division of the pseudopotential into a local and a non-local part,

$$V^{USPP}(\mathbf{r}) = V_{loc}(r) + V_{NL}(\mathbf{r}) \tag{2.25}$$

The local potential follows the HSC constraint to coincide with the all-electron potential outside a cut-off radius r_c, but it is smoother inside the cut-off region. The non-local potential, defined as

$$V_{NL}^{US} = \sum_{nm} D_{nm}^{(0)} |\beta_n\rangle\langle\beta_m| \tag{2.26}$$

is strictly localized inside the cut-off radius since the β-projection functions

$$|\beta_n\rangle = \sum_m \frac{(\epsilon_m^{AE} - (T + V_{loc}))|\phi_m^{US}\rangle}{\langle \phi_m^{US} | (\epsilon_n^{AE} - (T + V_{loc}))|\phi_n^{US}\rangle} \tag{2.27}$$

are limited to the core region by construction. The weight of each n,m-channel in the non-local potential is defined as

$$D_{nm}^{(0)} = \left[\langle \phi_n^{US} | (\epsilon_m - (T + V_{loc}))|\phi_n^{US}\rangle + \epsilon_m q_{nm} \right] - \int V_{loc}(\mathbf{r}')n(\mathbf{r}')d\mathbf{r} \tag{2.28}$$

The resulting pseudopotential is very smooth and the plane wave energy cut-off required for a transition metal atom is lowered down to half of the

value for norm conserving pseudopotentials. The price to pay for the relaxation of the norm conservation condition is that the Kohn-Sham equations to solve is a generalized eigenvalue problem

$$H|\phi_i^{US}\rangle = \epsilon_i \hat{S}|\phi_i^{US}\rangle \tag{2.29}$$

which includes an overlap operator $\hat{S}$,

$$\hat{S} = 1 + \sum_{nm} q_{nm}|\beta_n\rangle\langle\beta_m| \tag{2.30}$$

where q_{nm} is the integral of the $Q_{nm}(\mathbf{r})$ extending over the core region inside the cut-off radius. An additional complexity is caused by the non-local part of the pseudopotential because it is an operator which need to be evaluated for each wave function individually

$$E_{NL}[\phi_i] = \sum_i \langle\phi_i|V_{NL}|\phi_i\rangle \tag{2.31}$$

The ion-electron contribution to the total energy is therefore divided into the local and non-local part. The local part of the pseudopotential is included in the effective potential, defined in Eq. (2.31), while the non-local part is an additional term in the Hamiltonian [151]

$$H = -\frac{\hbar^2\nabla^2}{2m} + V_{eff}(\mathbf{r}) + \sum_{nmI} D_{nm}^I|\beta_n^I\rangle\langle\beta_m^I| \tag{2.32}$$

where

$$D_{nm}^I = D_{nm}^{(0)} + \int V_{eff}(\mathbf{r})Q_{nm}^I(\mathbf{r})d\mathbf{r} \tag{2.33}$$

The inclusion of the overlap operator of course adds computational complexity to the problem of solving the Kohn-Sham equations. However, for large systems the decreased number of expansion coefficient will out-weigh the added complexity because the Hamiltonian matrices will be much smaller. Consequently it takes a large system to really appreciate the advantages of the ultrasoft pseudopotential.

2.4 Supercell calculations

The required input in a first-principles calculation is the atomic species and positions. A solid material contains on the order of 10^{24} electrons and ion

cores per cm^3, but the symmetry of the crystal structure provides the possibility to diminish the problem to manageable size. The periodic crystal structure is represented by the unit cell and electrons within the material experiences the potential in the material as a periodically repeated entity. Bloch theorem [134] states that the wave function of an electron in a periodic potential can be described by the product of a local, periodic function and a plane wave:

$$\psi_{n,\mathbf{k}}(\mathbf{r}) = e^{i\mathbf{k}\cdot\mathbf{r}}\Phi_{n,\mathbf{k}}(\mathbf{r}) \tag{2.34}$$

The theorem imply that all important properties of the crystal can be studied within the unit cell. The periodicity of lattice also suggests that plane waves is a suitable basis set to expand the electron wavefunctions in crystalline materials. The cell periodic function is also expanded in the basis functions which converts the electron wave function into a Fourier sum

$$\psi_{n,\mathbf{k}}(\mathbf{r}) = \sum_{\mathbf{r}} c_{n,\mathbf{k}+\mathbf{G}} e^{i(\mathbf{k}+\mathbf{G})\cdot\mathbf{r}} \tag{2.35}$$

However, Bloch's theorem is not strictly applicable if the three dimensional translational symmetry is broken by a surface (or an interface). This means that plane waves are no longer suitable basis functions, since it would require an infinite number of plane waves to treat the discontinuity of the surface properly. The solution of the problem of lost periodicity is to consider a larger periodic cell, called a supercell, where the periodicity is artificially restored and the surfaces are far apart. This results in a super structure which is a layered structure for surface calculations. A number of different types of supercell have been used to study aperiodic structure.

2.5 Convergence

The accuracy of self-consistent calculations is ultimately dependent on the resolution of the basis set, the k-point sampling, the Fermi distribution smearing and the size of the supercell. It is therefore important to check the convergence of the results with respect to these parameters. There are two types of convergence, relative and absolute. Absolute convergence occurs when the value of a single quantity doesn't change by additional refinement of the resolution. Relative converge is the fact that the difference between two systems in some quantity doesn't change by additional refinement of the resolution. The relative convergence occurs most often at lower resolution than the absolute convergence since the error in two calculations might be "on the same side" causing an error cancellation in taking the difference.

The wavefunctions are expanded in a basis set and the accuracy of the representation depends on the number of terms included in the expansion. The usual test of convergence is to do a number of bulk calculations at various cut-off energies and check when the total energy variation has diminished below a threshold value.

The Kohn-Sham equations are solved in the reciprocal space by sampling discrete k-points in the Brillouin zone. The selection of the k-points must be done carefully to get a good representation of the wave function. Monkhurst and Pack [152] have suggested a grid of k-points evenly distributed over the Brillouin zone which is more or less standard today. The number of k-points needed depends on the dispersion of the bands in the Brillouin zone. The bands in metals have more dispersion compared to semiconductors and insulators, why it is necessary to include more k-points for metals. Another reason why metals demand more k-points than semiconductors, is that the Fermi level crosses partially filled valence bands and determining the exact crossing point requires a high k-point resolution.

2.6 Structure determination

Total energy calculations can be used very conveniently to determine the equilibrium structure of a system. The basic laws of physics tell us that the ground state of a system has the lowest energy.

$$E_0 \leq \langle \psi | H | \psi \rangle \tag{2.36}$$

Hence, comparing the total energy for different configurations of a system gives you the possibility to determine the configuration of lowest energy. The bulk properties of a crystalline material can accordingly be determined by calculating the total energy as a function of the cell volume. The values are fitted to Murnagham's universal binding curve [153]

$$E(V) = E_0 + \frac{B_0 V}{B_1(B_1 - 1)} \left[B_1(1 - \frac{V_0}{V}) - 1 + \left(\frac{V_0}{V} \right)^{B_1} \right] \tag{2.37}$$

The parameters in the Murnaghan's function is the Bulk modulus B_0, the pressure derivative of the Bulk modulus $B_1 = \frac{\partial B}{\partial P}$, the equilibrium volume V_0 and the ground state energy E_0

2.7 Structural optimization

In the previous sections we described the theory and some practical approximations to solve the electron Hamiltonian. This is accomplished by an iterative and self-consistent procedure which is inserted into the searching for the ionic configuration of the ground state. In fact, following the Born-Oppenheimer approximation, the ions (nuclei and their respective core electrons) move on the potential energy surface (PES)

$$V^{BO}(\mathbf{X}) = \sum_{\alpha<\beta} \frac{Z_\alpha Z_\beta e^2}{|X_\alpha - X_\beta|} + \epsilon_n(\mathbf{X}) \tag{2.38}$$

where $\mathbf{X}$ is the set of ionic positions. The ground state geometry of the system is obtained by minimizing the forces acting on the ions, that is by searching for the minimum of the PES. Hence we can calculate the forces acting on each ion by the energy gradient with respect to the ionic positions and construct an algorithm to find the ground state geometry by using the Hellman-Feynman theorem [154]:

Hellman-Feynman theorem *Let η be a parameter in the Hamiltonian $\hat{H}$, Ψ_η an eigenfunction of $\hat{H}$ of energy E. Then*

$$\frac{\partial E}{\partial \eta} = \left\langle \Psi_\eta \left| \frac{\partial \hat{H}}{\partial \eta} \right| \Psi_\eta \right\rangle \tag{2.39}$$

In this case the parameter η is given by the set of ionic positions $\mathbf{X}$. Different techniques have been implemented to actually find the ground state geometry of the systems, all based on the Hellman-Feynman theorem. In this thesis we choose the Broyden-Fletcher-Goldfarb-Shanno (BFGS) procedure [155], which is a quasi-Newton method based on the calculation of an approximate Hessian matrix.

In this algorithm the total energy is considered as a function of the coordinates of the N released atoms $E_{tot} = E_{tot}(\mathbf{X})$. An expansion of E_{tot} around the minimum energy configuration $\mathbf{X}_m$ yields

$$E_{tot}(\mathbf{X}) = E(\mathbf{X}_m) + (\mathbf{X} - \mathbf{X}_m) \cdot \frac{\partial E}{\partial \mathbf{X}} + \frac{1}{2}(\mathbf{X} - \mathbf{X}_m)_i H_{ij} (\mathbf{X} - \mathbf{X}_m)_j \tag{2.40}$$

where H_{ij} is the Hessian matrix

$$H_{ij} = \frac{\partial^2 E}{\partial \mathbf{X}_i \partial \mathbf{X}_j} \tag{2.41}$$

The gradient of the total energy at the minimum is zero, so the first order term vanishes. Taking the gradient of Eq. (2.40) gives the forces as function of the coordinates. Inverting the expression gives the equation for the minimum ionic positions

$$\mathbf{X}_m = \mathbf{X} - (H)^{-1} \cdot \mathbf{F} \tag{2.42}$$

If the inverse Hessian is known the minimum configuration could be determined directly, but it in general unknown. Instead an iterative method is employed to calculate the inverse Hessian by taking successive ionic steps and recalculating the inverse Hessian matrix in each step. The efficiency of the algorithm is improved if the inverse Hessian matrix is preconditioned to have a good start value.

To summary, the self-consistent approach in solving the total Hamiltonian and its electron and ionic parts starts from a given set of atomic positions in the unit cell and an initial guess of the electron density (generally obtained by a superposition of atomic orbitals). Then the electronic Hamiltonian is solved self-consistently due to the dependence of the effective potential on the density. The convergence of the electronic Hamiltonian is reached when the charge density difference between two consecutive steps is less than a given threshold. At this point, the ionic Hamiltonian is solved and the forces acting on atoms are computed. If these forces are higher than a given threshold, the ions are moved and a new set of coordinates determines the input ionic potential for a further electronic self-consistent calculation. When the forces acting on atoms are sufficiently low the computational process comes to end so that it is possible to extract the physical quantities of interest.

Chapter 3

Thermally activated processes

The identification of a lowest energy path for a rearrangement of a group of atoms from one stable configuration to another is an important and common problem in theoretical chemistry and in condensed matter physics. Such a path is often referred to as the "minimum energy path" (MEP). It is frequently used to define a "reaction coordinate" [156] for transitions, such as chemical reactions, changes in conformation of molecules, or diffusion processes in solids. The potential energy maximum along the MEP is the saddle point energy which gives the activation energy barrier, a quantity of central importance for estimating the transition rate within harmonic transition state theory [157].

There are many different methods for finding reaction paths and saddle points.

- Some schemes start at the local minimum on the potential energy surface representing the initial state and then trace stepwise, in a sequential manner, a path of slowest ascent [158, 159, 160]. Such slowest ascent paths, however, do not necessarily lead to saddle points. Figure 3.1 shows an example of such a system.

- A commonly used method involves calculating normal modes of a local harmonic approximations of the potential energy surface and then following each of the modes until a saddle point is found [161, 162]. Each step in this procedure requires evaluation and diagonalization of the second derivative matrix and is therefore limited to rather small systems and descriptions of atomic interactions where second derivatives are readily available (excluding, for example, plane wave based density functional theory calculations).

- Other methods make use of a two point boundary condition, i.e. both

the initial and final configurations for the transition are given. These would normally be two local minima on the multidimensional potential energy surface.

This chapter focuses on methods that only require the potential energy and the its first derivative with respect to the atom coordinates because such methods can be applied, for example, in plane wave based Density Functional Theory calculations, and the computational effort typically scales well with system size. The simplest and perhaps the most intuitive method is the **"drag" method**, where some subset of the coordinates in the system is used to define a progress variable, often through linear interpolation between the initial and final configurations. This one degree of freedom is then varied stepwise from the initial to the final value and at each step a minimization is carried out over the remaining degrees of freedom (a total of $(3N - 1)$ degrees of freedom if the system consists of N atoms in 3 dimensions). This method can work well in simple cases, but there are many instances where it fails. The path generated may be discontinuous and the procedure may depend on the direction of the drag (hysteresis ects). In particular, some atomic coordinates may "slip" near the saddle point region and the saddle point configuration will then be missed [164, 165]. An example of this is given in Figure 3.1.

Even though the initial straight line interpolation goes very close to the saddle point, the relaxation of the remaining degree of freedom gives a result that is quite far from the MEP. For a range of values of the drag coordinate, there are, in fact, two minima. If the drag coordinate is incremented gradually using the previous minimum as an initial guess in the minimization procedure for the next value of the drag coordinate, then two different paths will be traced out depending on whether the calculation starts from the initial state or the final state. These paths "overshoot" the saddle point until the potential energy contours become parallel to the line corresponding to the degree of freedom that is being optimized.

More recently much more reliable methods have emerged which are significantly more involved to implement or costly to use. In these methods, a chain of images (or replicas, or "states") of the system is generated between the end point configurations and all the intermediate images are optimized simultaneously in some concerted way. An example calculation is shown in Figure 3.2. Here, the initial images are located along a line joining the initial and final point, but after an optimization calculation acting on all the images simultaneously, the images lie near the MEP. The distribution of the images, which give a discrete representation of the path, can be controlled and has been set here to be twice as high in the barrier region as compared

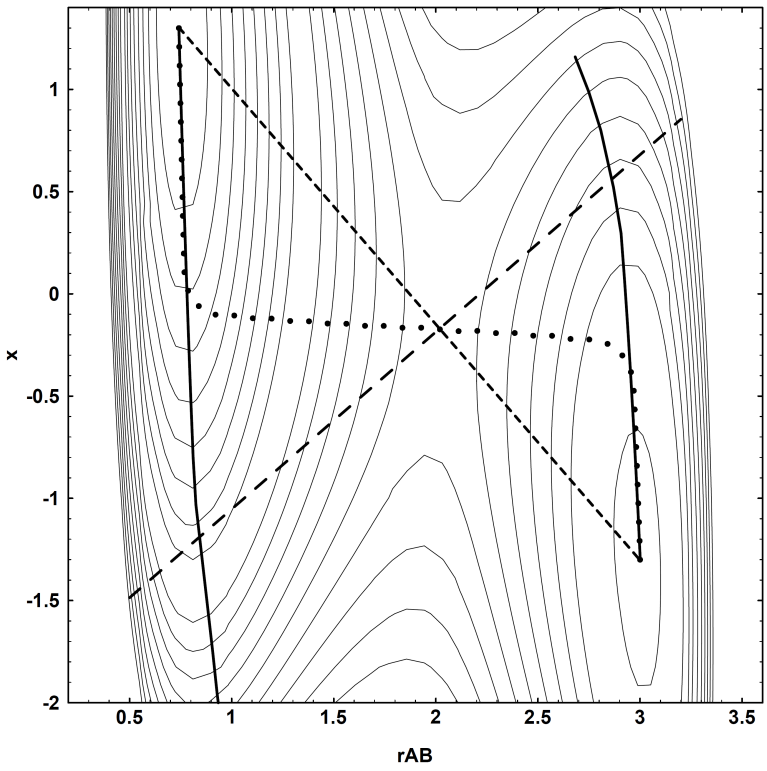

Figure 3.1: A contour plot of the potential energy surface for a simple test problem, where an atom, B, can form a chemical bond with either one of two fixed atoms, A or C, (described by a LEPS potential) and is simultaneously coupled in a harmonic way to a fourth atom, D. The horizontal axis gives the A-B distance and the vertical axis the B-D distance. All atoms are confined to a line. The MEP is shown with a dotted line going through the saddle point (obtained with the NEB method using 50 images). A straight line interpolation between the initial and final state minima, defining a "drag coordinate", is shown with small dashes. In the drag method, the system energy is minimized with respect to all remaining degrees of freedom, corresponding here to relaxation along a line perpendicular to the drag line. Such a line going through the saddle point is shown with large dashes. The drag method gives paths indicated by two thick, solid lines. The drag paths lie close to the slowest ascent paths, which do not lead to the saddle point. The result of the drag method is a discontinuous path which depends on the direction of the drag. Figure taken from Jónsson *et al.* [163].

with the end regions. An important aspect of these types of methods is that parallel computers or simply a cluster of networked computers can be used

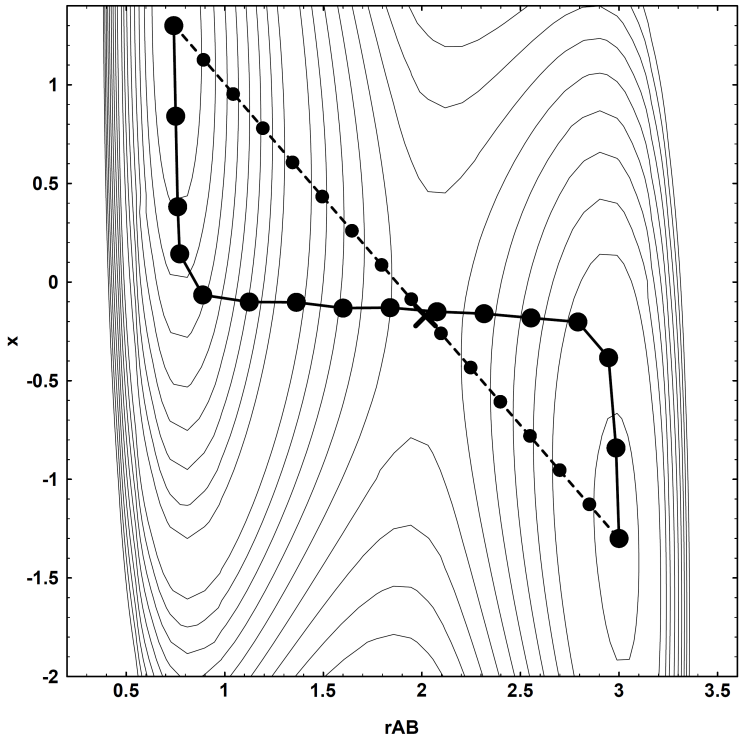

Figure 3.2: Same problem of Figure 3.1. The initial and final configuration of a NEB with 16 images is shown. The straight line interpolation between the initial and final point is shown with dashes and the small, filled circles along the line indicate the initial configuration chosen for the images in the elastic band. The larger, filled circles lying close to the MEP show the images after convergence. The spring constant is $k = 0.5$ near the ends of the band and $k = 1.0$ in the middle so as to increase the density of images in the most relevant region. Figure taken from Jónsson *et al.* [163].

very efficiently for finding the MEP, in contrast to methods that are based on a sequential "walk" along the potential energy surface.

This chapter, in particular, will focus on the *Nudged Elastic Band method (NEB)*, the *Climbing Image–NEB* and their implementation in the open–source Quantum–ESPRESSO.

3.1 The Nudged Elastic Band method

The minimum energy path is defined as the particular configuration space path, connecting reactants and products, characterised by the property that

the components of the forces orthogonal to the path are zero:

$$\nabla V(\mathbf{x}(s)) - \boldsymbol{\tau}(s)(\boldsymbol{\tau}(s)|\nabla V(\mathbf{x}(s))) = 0 \tag{3.1}$$

where $\boldsymbol{\tau}(s)$ represents the normalised tangent vector and MEP is parametrised by an arbitrary reaction coordinate $s \in [0, 1]$. It has also been shown that, the MEP is, in the low temperature limit, the most probable path that connects two minima in the PES. Equation (3.1) states that the potential energy is stationary on each hyperplane orthogonal to the MEP. However, only those paths in which the energy is minimised on the orthogonal hyperplanes are physically relevant, the others having zero probability of being reaction paths.

The identification of the MEP and of the saddle point separating reactants and products can be achieved by solving numerically the equation (3.1). The first step consists in representing the path $\mathbf{x}(s)$, which is a continuous function, in a form suitable to be handled numerically. This is done by discretising the reaction coordinate s and by representing the path on this discretized mesh. The continuous $\mathbf{x}(s)$ is thus represented by a *chain of images*:

$$\begin{aligned} s &\rightarrow i \cdot \delta s \\ \mathbf{x}(s) &\rightarrow \mathbf{x}_i \\ \boldsymbol{\tau}(s) &\rightarrow \boldsymbol{\tau}_i = \frac{\mathbf{x}_{i+1} - \mathbf{x}_{i-1}}{|\mathbf{x}_{i+1} - \mathbf{x}_{i-1}|} \end{aligned} \tag{3.2}$$

Therefore the discreatised version of equation (3.1) is given by:

$$\nabla V(\mathbf{x}_i) - \boldsymbol{\tau}_i(\boldsymbol{\tau}_i|\nabla V(\mathbf{x}_i)) = 0 \tag{3.3}$$

The solution of this set (one for each point used to represent the path) of coupled non-linear equations represents the discretized MEP. Equations (3.3) are solved when, for each image, the energy is minimised on the hyperplane orthogonal to the discretized path. Such minimised can be carried out iteratively using a sort of steepest-descent dynamics in the space of paths. The procedure starts by constructing the initial path as a chain of equispaced images. Then each image evolves following the fictitious dynamics given by projected force:

$$\begin{aligned} F(\mathbf{x}_i)_\perp &= -[\nabla V(\mathbf{x}_i) - \boldsymbol{\tau}_i(\boldsymbol{\tau}_i|\nabla V(\mathbf{x}_i))] \\ &\Downarrow \\ \mathbf{x}_i(t + \delta t) &= \mathbf{x}_i(t) + \delta t F(\mathbf{x}_i(t))_\perp \end{aligned} \tag{3.4}$$

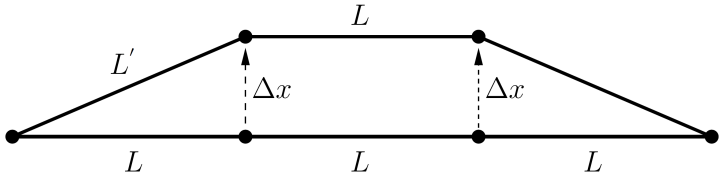

$$L' = \sqrt{L^2 + \Delta x^2}$$

$$L' - L = L\left(\sqrt{1 + \frac{\Delta x^2}{L^2}} - 1\right) \sim \frac{1}{2}\frac{\Delta x^2}{L^2}$$

Figure 3.3: An illustration of the evolution of an equispaced path. In is shown that the variation in the inter-image distance is second order in the displacement Δx.

The path is converged to the MEP when $\mathbf{F}(\mathbf{x}_i)_\perp = 0$ for all the images $(\mathbf{x}_i)$ in the chain.

The main limit of this approach is that this dynamics does not preserve the inter-image distance and, in general, does not prevent images to slide down in the two minima. Indeed, since the path is represented with limited accuracy, also the estimate of the tangent (and thus of the projections) is approximately known and a residual component of the force parallel to the path acts on the images. The result is that the images start sliding down along the path, further reducing the accuracy of the projections. If this behaviour is not opposed, all the images of the chain can eventually collapse in the two minima. This effect is described in Figure 3.3 where, however, it is also shown that, as a positive consequence of the projection of the forces, the variation of the inter-image distance is of order Δx^2, where Δx is the image displacement: the inter-image distance is thus preserved at first order in the time step δt.

From these observation it is clear that the strategy used to discretize the path and constraints imposed to preserve the parametrisation (i.e. the inter-image distance) are both of fundamental importance in the numerical solution of equation (3.3).

In the nudged elastic band method (NEB) [166, 167], the path parametrisation is enforced by connecting each image of the chain to its neighbours by "virtual" springs of zero rest-length. Therefore the images feel both the forces due to external potential (the true projected, $\mathbf{F}(\mathbf{x}_i)_\perp$) and those due to the "virtual" springs $\mathbf{F}(\mathbf{x}_i)^{elastic}$. The discretized path is thus described as an

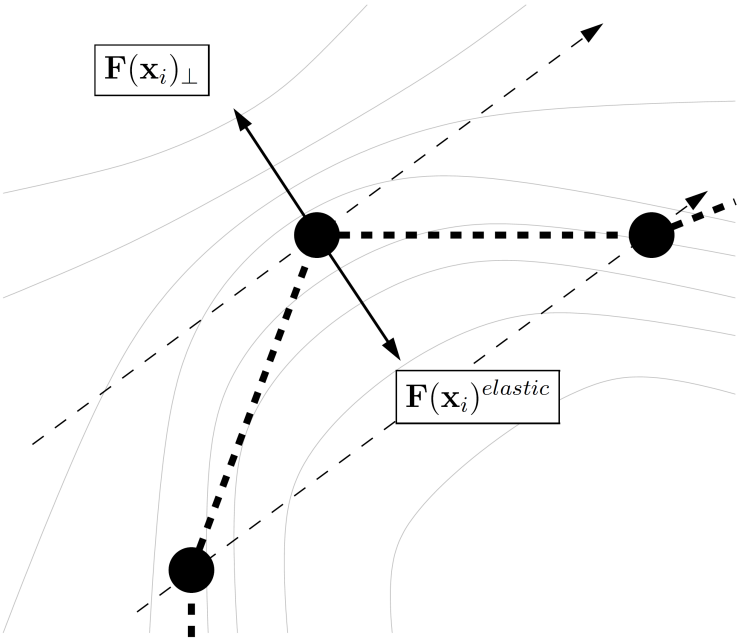

Figure 3.4: Illustration of the "corner cutting" problem

elastic band. Unfortunately, when the path bends the springs can introduce an artificial component of the force orthogonal to the path that prevents the chain to converge to the true MEP. As shown in Figure 3.4, this effect, which is generally referred to as "corner cutting", is more relevant where the curvature to the path is larger. To reduce these spurious effects, in the NEB method the elastic forces are projected along the path's tangent:

$$\mathbf{F}(\mathbf{x}_i)_\parallel^{elastic} = -k\boldsymbol{\tau}_i(\boldsymbol{\tau}_i|(2\mathbf{x}_i - \mathbf{x}_{i+1} - \mathbf{x}_{i-1})) \tag{3.5}$$

The procedure of projecting the spring forces is called nudging of the elastic band and represents the principal improvement offered by the NEB method against its predecessors: it is essential to decouple the effect of the "virtual" springs from the external potential. The chain that satisfies equation (3.3) in presence of the springs is found by evolving each image with the steepest-descent algorithm, where the overall force vector acting on the image $\mathbf{x}_i$ at time t (hereafter indicated as $\mathbf{F}(\mathbf{x}_i(t)) = \mathbf{F}(\mathbf{x}_i(t))_\perp + \mathbf{F}(\mathbf{x}_i(t))_\parallel^{elastic}$) is used:

$$\mathbf{x}_i(t + \delta t) = \mathbf{x}_i(t) + \delta t\mathbf{F}(\mathbf{x}_i(t)) \tag{3.6}$$

In the NEB method the "virtual" springs act as a penalty function that, when all the elastic constants have the same value, favours the configura-

tion of the chain where all images are equispaced. At convergence all the inter-image distances are equal. As a consequences of the projections, this behaviour does not depend on the specific choice of the elastic constant, provided that they are larger than zero.

In the NEB method the elastic forces act exclusively along the path; one is thus free to choose different spring constants between different pair of images without affecting the convergence of the chain to the MEP (this because the geometrical definition of MEP given by equation (3.1) is invariant for any reparametrisation of path). Clearly, the saddle point is the most important configuration along the MEP and one would typically prefer to have higher resolution close to this point than near the end points. This can be accomplished within the variable-elastic-constants scheme, where stiffer springs are used near the point of highest energy. In particular, this is done by specifying a minimum and a maximum value for the elastic constants (k_{min} and k_{max}) and interpolating between these two values:

$$k_i = \frac{1}{2}\left(k_{max} + k_{min} - (k_{max} - k_{min})cos\left(\pi\frac{(V(\mathbf{x}_i) - V_{min})}{(V_{max} - V_{min})}\right)\right) \tag{3.7}$$

The variable-elastic-constant scheme thus provides a natural way of choosing the parametrisation of the path so that a minimum number of images is required to have a good estimate of the saddle point position. In the case described above the resolution is risen around points of high potential energy, which is a reasonable choice because the saddle point has the highest energy along the path. An alternative choice can be that of rising the path resolution (stiffer spring) around points of largest local curvature $\mathbf{w}(s) = \frac{d\boldsymbol{\tau}(s)}{ds}$. Indeed, the number of images required to represent a path depends on the global curvature of the path

$$\Omega = \int_0^1 |\boldsymbol{\omega}(s)|ds \tag{3.8}$$

A straight path can be represented by only two images, but a path that bends on itself many times can require a large number of images, even if the energy barrier is very small. By defining the discretized local curvatures as $\boldsymbol{\omega}_i = \frac{\mathbf{x}_{i+1}-\mathbf{x}_i}{|\mathbf{x}_{i+1}-\mathbf{x}_i|} - \frac{\mathbf{x}_i-\mathbf{x}_{i-1}}{|\mathbf{x}_i-\mathbf{x}_{i-1}|}$, "curvature-weighted" elastic constants can be used, obtaining an optimal parametrisation of the path. As in original recipe, the elastic constants are obtained interpolating between a minimum and a maximum value:

$$k_i = \frac{1}{2}\left(k_{max} + k_{min} - (k_{max} - k_{min})cos\left(\pi\frac{(\omega_i - \omega_{min})}{\omega_{max} - \omega_{min})}\right)\right) \tag{3.9}$$

Within the variable elastic constants scheme the projected elastic forces are given by:

$$k_{i,i+1} = \frac{1}{2}(k_i + k_{i+1}) \tag{3.10}$$

$$\mathbf{F}(\mathbf{x}_i)_{\parallel}^{elastic} = -\boldsymbol{\tau}_i(\boldsymbol{\tau}_i|(k_{i,i+1}((\mathbf{x}_{i+1} - \mathbf{x}_i) - k_{i-1,i}(\mathbf{x}_i - \mathbf{x}_{i-1}))) \tag{3.11}$$

As previously pointed out, the choice of the elastic constants (k_{min} and k_{max}) is not essential for the convergence of the path to the MEP because of the projection of the forces described above. Anyway, a wrong choice of the elastic constants can seriously affect the convergence rate of the chain of images to the MEP because it can introduce longitudinal modes of frequency much higher than the "physical" modes of the potential energy surface, resulting in a hill-conditioned optimisation problem. In this case the time step used to evolve the chain of images will be dictated by the artificial longitudinal modes. This is one of the more severe limitations to the usability of the NEB method. On the other hand it is known that the largest frequency supported by the elastic band is given by $\nu = \frac{1}{\pi}\sqrt{k_{max}}$. The optimal value of k_{max} can thus be obtained requiring that the time step, chosen small enough to well represent all the frequencies characterising the potential energy surface, is also smaller than ν^{-1}. In practice, given the time step as an input, k_{max} is automatically set to $k_{max} = \frac{\pi^2}{n^2\delta t^2}$ (where n is some integer larger than one) so that also the elastic frequencies are well described. This implementation of NEB thus removes the duty of choosing the correct value for the elastic constants. Of course, the soft longitudinal modes of the elastic band are still present, thus influencing the convergence rate to the MEP.

3.2 Climbing Image NEB

The climbing image NEB (CI-NEB) method, introduced by G. Henkelman, B. P. Uberuaga and H. Jónsson in [166], is a small, but important, improvement of the NEB method originally described in [168]. Information about the shape of the MEP is retained, but a rigorous convergence of to a saddle point is also obtained. This additional feature does not add any significant computational effort. The climbing image scheme consists in the following procedure: after a few iterations with the regular NEB, the image with the highest energy i_{max} is identified. The force on this image is set to be the full force due to the potential with the component along the path inverted:

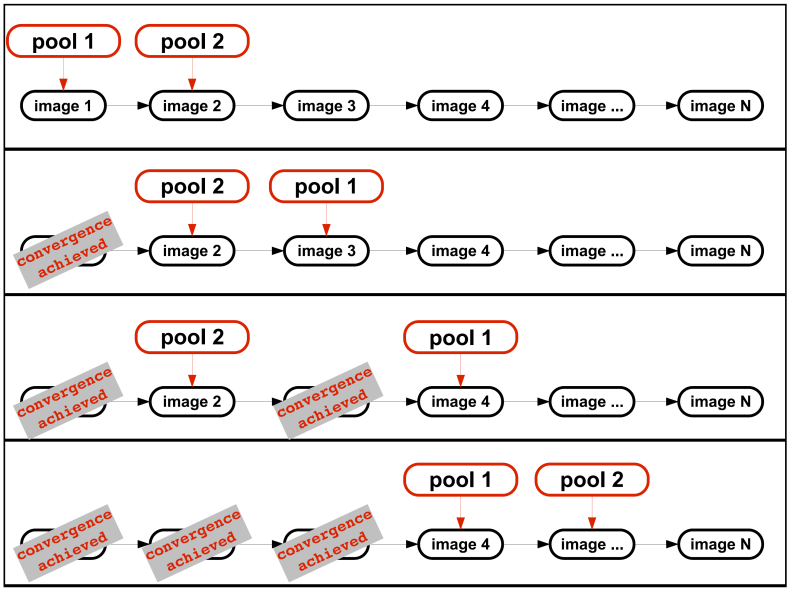

Figure 3.5: Parallelisation scheme used for NEB calculations. Here it is assumed that 2 pools (pool 1 and pool 2) are used on a path discretized by N images. Pool 1 working on image 1 and pool 2 on image 2. The first pool that reaches the self-consistency (pool 1) starts working on image 3, and so on.

$$\mathbf{F}(\mathbf{x}_{i_{max}}) = \nabla V(\mathbf{x}_{i_{max}}) + 2\boldsymbol{\tau}_{i_{max}}(\boldsymbol{\tau}_{i_{max}}|\nabla V(\mathbf{x}_{i_{max}})) \tag{3.12}$$

Qualitatively, the climbing-image moves up the potential energy surface along the elastic band and down the potential surface perpendicular to the band; moreover it is not effected by the spring forces at all. The other images of the chain serve the purpose of defining the one degree of freedom for which a maximization (rather than a minimisation) of the energy is carried out. Since the images in the chain eventually converge to MEP, they give a good approximation to the reaction coordinate around the saddle point.

CI-NEB has proved to be extremely useful because it directly provides an accurate identification of saddle point without any additional effort so that, at the end of a path optimisation, the activation energy and the saddle point coordinates are immediately available.

3.3 Implementation

The NEB have been implemented by the author in the open-source Quantum-ESPRESSO package [169]. In this implementation the path optimisation is performed on the electronic ground state (the Born-Oppenheimer surface), so that a full self-consistency is required for each image at each step. This is by far the most demanding part of the whole calculation, in terms of both memory and cpu time. The optimisation scheme outlined above permits a very efficient parallelisation in which different pools of cpus work on different images; the communication between pools is negligible.

The load balancing is optimised by adopting the strategy depicted in Figure 3.5, where, as an example, 2 pools (pool 1 and pool 2) are used on a path discretized by N images. Pool 1 starts working on image 1 and pool 2 on image 2. The first pool that reaches the self-consistency starts working on image 3, communicating to the other one that the next image available is 4. For particular systems, it may occur that the self-consistency on image 2 takes so long to be completed that all the other images are done by pool 1.

Chapter 4

Clean and defected ZnO non polar surfaces

Zinc oxide is widely used in technological applications because of its unique electronic and electro-optical properties. In particular, ZnO has been considered a good candidate for gas sensors [170, 171, 172]. Recently, ZnO and other metal oxide nanowires-based quasi-one-dimensional gas sensors have received great attention due to their excellent sensing property and low cost [173, 174, 175, 176]. ZnO nanowire gas sensors for sensing oxygen, ethanol, NO_2, and NH_3 have been fabricated [174, 175, 176]. The high sensitivity is attributed to the high surface-to-volume ratio and finite charge-carrier concentration. The sensing mechanism of metal-oxide-based gas sensors relies on the change in electrical conductivity caused by adsorption and reaction of gas molecules on surfaces. It has been well accepted that the electrical property change is the consequence of charge transfer between the quasi-one-dimensional host and the chemisorbed species [177]. Of course, it is expected that gas sensing applications require a precise control on the surface morphology, chemistry and composition: usually, nanostructures with different surface facets are employed, the $(10\bar{1}0)$ and $(11\bar{2}0)$ surfaces/facets being the most stable and abundant ones [32, 33].

Understanding the behavior of native point defects is essential to the successful application of any semiconductor. These defects often control, directly or indirectly, doping, compensation, minority carrier lifetime, and luminescence efficiency. They also assist the diffusion mechanisms involved in growth, processing, and device degradation. Doping forms the basis of much of semiconductor technology and can be drastically affected by native point defects such as vacancies, self-interstitials, and antisites. In ZnO, specific native defects have long been believed to play an even more important role. As-grown ZnO frequently exhibits high levels of unintentional n-type

conductivity, and native point defects have often been invoked to explain this behavior. Oxygen vacancies and zinc interstitials have most often been mentioned as sources of n-type conductivity in ZnO. Moreover, it has been shown that the presence of native surface and subsurface point defects, their concentration and depth distribution can strongly affect the electronic properties and electrical response of metal-ZnO interfaces and Schottky barriers, as well as the gas adsorption on specific ZnO surfaces [38].

In literature, there are some *ab initio* density functional theory (DFT) calculations that have been performed to elucidate the behavior of both intrinsic [39, 40, 41, 42] and extrinsic point defects [43, 44]. In particular, it has been noted that the oxygen vacancies can be considered as the most abundant and the chemically most reactive kind of atomic defects for a large variety of oxides [45]. Previous theoretical studies of the bulk ZnO and its surfaces have proven the impact of oxygen deficiency on the electronic and structural properties [46, 47, 48, 49, 50]. But, a systematic study of the vacancy diffusion along and across the ZnO non–polar $(10\bar{1}0)$ and $(11\bar{2}0)$ surfaces together with the implications on relevant material properties is still lacking. Moreover, the actual possibility of observing stable (sub)surface oxygen defects has been experimentally proven in the early 80's [51, 52], but questioned by recent STM experiments [53, 54].

In this chapter we discuss the structural and electronic properties of oxygen deficient surfaces as a function of the defect position with respect to the surface. Oxygen vacancy migration paths are characterized in the framework of the climbing image nudged elastic band method considering the diffusion both parallel and across the surface. The calculated energy barriers and activation temperatures involved in the diffusion process are discussed and compared with the respective bulk counterparts. Moreover, in the case of the $(10\bar{1}0)$ surface, we try to elucidate the apparent disagreement of the available experimental data, which report, depending on the preparation conditions, the observation of a finite concentration of oxygen vacancies or the lack of them close to the surface. With this aim, we also consider the energetics of ZnO-dimer and Zn vacancies, which might occur as the prevailing atomic defects under suitable conditions of temperature and pressure.

This chapter is organized as follows. In Sec. 4.1 the technical details on the performed calculations are summarized. In Sec. 4.2 we present the results for the ideal and defected ZnO $(10\bar{1}0)$ and $(11\bar{2}0)$ surfaces. The Sec. 4.3 deals with the diffusion of oxygen vacancies in the bulk ZnO crystal and in proximity of ZnO surfaces. Finally, in Sec. 4.4 some conclusions are drawn.

4.1 Methodology

4.1.1 Computation details

All first–principles calculations are carried out within the DFT framework as implemented in the QUANTUM–ESPRESSO package [169]. We use the generalized gradient approximation (GGA) parametrized with the Perdew, Burke and Ernzerhof (PBE) exchange–correlation functional [144] and Vanderbilt ultrasoft pseudopotentials [150] to mimic the ion cores. The kinetic–energy cutoff for the plane waves is set to 40 Ry while the cutoff for the augmented density is set to 320 Ry. The crystal/surface geometries are optimized with the direct energy minimization technique of Broyden–Fletcher–Goldfarb–Shanno [178]. The optimization is stopped when each Cartesian component of the force acting on each atom is less than 0.026 eV/Å and when the total energy difference between consecutive steps of the minimization procedure is less than 10^{-4} eV. All results presented in the next sections are referred to the optimized systems.

To test the reliability of the methods and of the pseudopotentials, the bulk ZnO structural and electronic properties have been computed. The ZnO polymorph of interest for the present study is the wurtzite structure. The first Brilluoin zone (BZ) is sampled using a $16 \times 16 \times 12$ Monkhorst–Pack k–point mesh. The BZ sampling meshes for all the other systems under investigation are scaled so as to be consistent, as close as possible, with that used for the bulk unit cell. Using the Birch-Murnaghan equation of state [179], we obtained the crystallographic parameters $a = 3.295$ Å, $c = 5.294$ Å, and $u = 0.3812$ which well compare with the experimental values [90] $a = 3.258$ Å, $c = 5.220$ Å, and $u = 0.382$, respectively. The band structure along relevant paths in the first Brillouin zone is shown in Figure 4.1, right panel; the band gap value at Γ of 0.71 eV underestimates the experimental value [91] of 3.4 eV, but it is consistent with previous DFT calculations [41]. While the DFT failure in predicting the band gap is a well known fact, the underestimation in the case of ZnO goes well beyond the typical errors found for other materials. Moreover it is observed that

- the Zn 3d states are located at ~ 5 eV below the valence band maximum (VBM). This is more than 2 eV too shallow compared with the measured value of 7.5–8.8 eV [180];
- these underbound d states strongly hybridize with the valence p states and push these states up, resulting in a greatly reduced gap (~ 0.7 eV).

The road we have followed for curing these problems is that proposed by Janotti and co–workers [47], who employ the DFT+U scheme. The Hubbard

U values we included are 12.0 eV on the Zn $3d$ orbitals and 6.5 eV on the oxygen $2p$ orbitals, which have already been shown to work well for ZnO [181]. The lattice parameters, recomputed within the DFT+U scheme, change by about 1%, whereas a 3.31 eV Γ–point band gap is found (see Fig. 4.1, left panel). The DFT and DFT+U results are summarized in Table 4.1. Since only the electronic properties are significantly modified using the DFT+U scheme, following Ref. [181] we first optimize the atomic positions at the standard DFT level and only after we include the Hubbard correction for the calculation of the electronic properties.

Table 4.1: The lattice parameters a, c (in Å), the internal coordinate u and the energy gap $E_{\rm gap}$ (in eV) of Bulk ZnO. Theoretical results are obtained from GGA and GGA+U calculations. Experimental and theoretical data [90, 91, 47, 181] are reported for comparison.

	a	c	u	E_{gap}
EXP [90, 91]	3.258	5.220	0.382	3.4
GGA	3.295	5.294	0.381	0.71
GGA+U	3.258	5.227	0.381	3.31
LDA [47]	3.195	5.160	0.379	0.80
LDA+U [47]	3.148	5.074	0.379	1.51
GGA [181]	3.289	5.315		0.7
GGA+U [181]	3.239	5.257		3.3

The ZnO $(10\bar{1}0)$ and $(11\bar{2}0)$ surfaces are modeled using a slab geometry of periodically repeated supercells containing 12 atomic planes. This slab thickness proved to be sufficient to ensure good convergence of the calculated properties when the point defect is moved towards the bulk-like (deeper) positions. A vacuum width of 15 Å separating each slab from its periodic images proved to be sufficient to avoid spurious interactions between repeated slabs. The ZnO $(10\bar{1}0)$ and ZnO $(11\bar{2}0)$ stoichiometric surfaces are shown in Figure 4.2(a) and 4.2(b), respectively. As pointed out in the Figure 4.2, while the $[11\bar{2}0]$ direction can be viewed as a stacking of equidistant lattice planes, the $[10\bar{1}0]$ direction can be defined as consisting of an $ABABAB\ldots$ stacking of ZnO planes, in which each B plane has a distance of 0.95 Å and 1.90 Å from the two nearest A planes (these distances are those of the ideal bulk geometry).

For both slab geometries, we adopt an "asymmetric" slab model, with the atoms in the four bottom atomic planes anchored to their bulk positions. All the other atoms are allowed to fully relax according to their interatomic

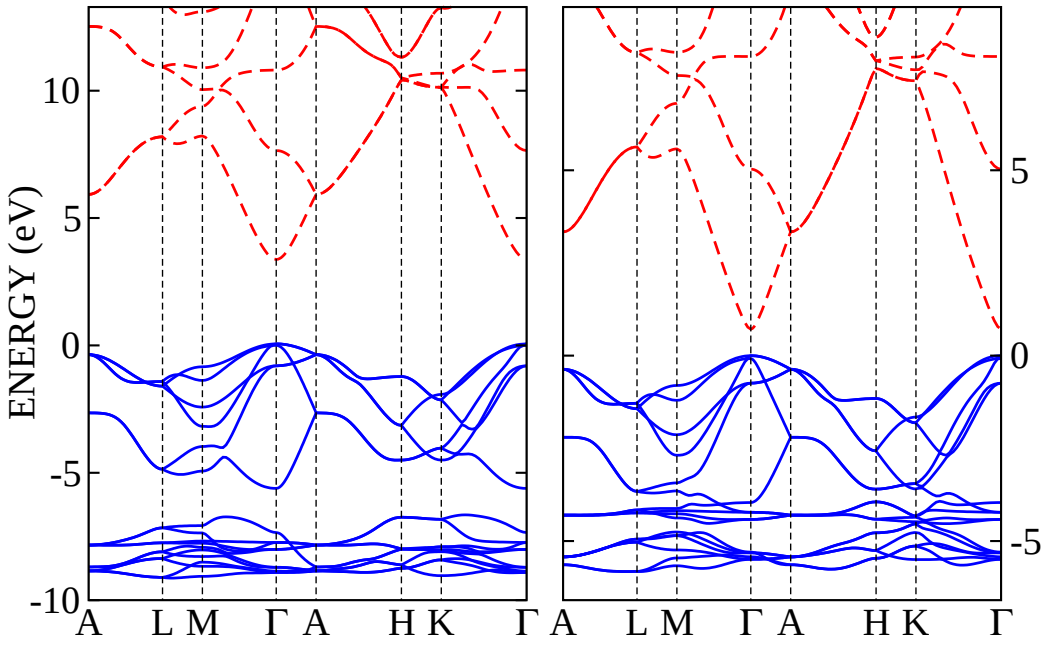

Figure 4.1: Band structure of bulk ZnO obtained from GGA+U (left panel) and GGA (right panel) calculations. The zero energy corresponds to the top valence band. The occupied (unoccupied) bands are drown as blue solid (red dashed) curves.

forces. The surface and the point defect(s) are thus only modeled on the top side of the slab. It has already been shown that modeling the surface in this way leads to a much better convergence of the geometrical and electronic properties with respect to the number of layers in the slab [182]. A dipole correction has been applied to get rid of spurious electric fields across the slab arising from the combination of periodic boundary conditions with the asymmetric slab model [183].

Isolated oxygen vacancies in bulk ZnO have been modeled by removing a single oxygen atom from a $3 \times 3 \times 2$ supercell (the BZ sampling is performed using a $5 \times 5 \times 6$ k-point grid) while, for the study of oxygen vacancies at the ZnO $(10\bar{1}0)$ and ZnO $(11\bar{2}0)$ surfaces, we have considered, respectively, 2×2 and 2×1 surface supercells to study the dependence of the calculated properties as a function of the defect depth with respect to the surface. These supercells correspond to a minimum vacancy–vacancy distance of 9.8 Å, 6.6 Å and 5.3 Å for the defected bulk, $(10\bar{1}0)$ and $(11\bar{2}0)$ ZnO surfaces,

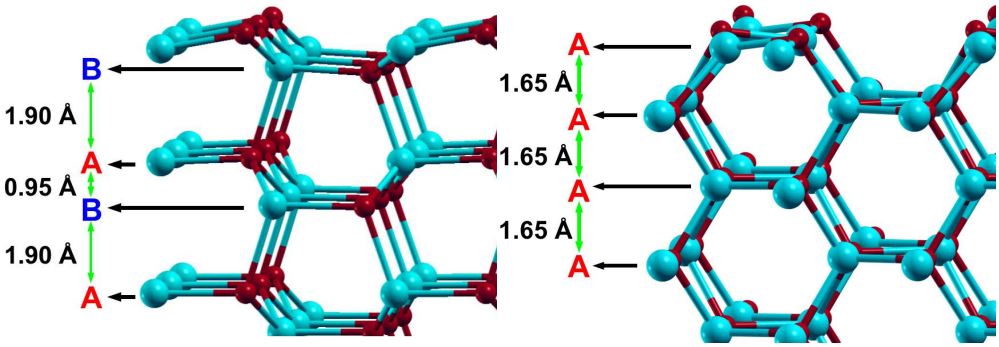

(a) (b)

Figure 4.2: Side view of the reconstructed ZnO (a) $(10\bar{1}0)$ and (b) $(11\bar{2}0)$ stoichiometric surfaces. Oxygen are small red, and zinc atoms are large blue. The lattice plane distances reported on the left are those of the bulk crystal. Figure taken from D'Amico *et al.* [184].

respectively. Convergence tests with respect to the vacancy–vacancy distance showed small variations (within 0.1 eV) of the vacancy formation energies and of the surface band gap. Yet, electronic levels localized around the defect did show a larger sensitivity to the vacancy concentration. As such, surface band structure calculations were performed using a 3×3 supercell.

To shed light on the stability of the above mentioned defected surface and bulk ZnO models, we have carried out an extensive thermodynamic and kinetic analysis, aimed to identify the most favorable configurations as well as migration paths for oxygen vacancies in thermally activated diffusion processes. The thermodynamic analysis (relative stability as a function of the oxygen content at a given pressure and temperature) is carried out according to the methodology proposed by Reuter and Scheffler [185], which is outlined in the next section. Migration paths are studied by employing the climbing image nudged elastic band (CI–NEB) method [186, 166], an efficient and improved algorithm aimed to find the minimum energy path (MEP) connecting an initial and a final state configuration corresponding to two minima of the potential energy surface. The kinetics underlying the thermally-activated transition from the initial to the final state is governed by the energy barrier, defined as the energy difference between the saddle point located along the MEP and an initial state configuration. In the specific case of the vacancy defect migration, the initial and final configurations correspond to two different positions of the defect. An accurate sampling of the MEP is performed using eleven intermediate images (between the initial and final point of the path). Forces on the path images in CI–NEB calculations were minimized to

less than 0.1 eV/Å to ensure convergence.

As a final remark, it is worth mentioning that careful tests have been performed to ensure full convergence of the main computed properties (formation energies, energy barriers in diffusion paths, etc.) with respect to the parameters entering the calculations (cut-off, BZ sampling, etc.).

4.1.2 Thermodynamic stability

The relative stability (against oxidation and reduction processes) of different (defected or undefected) surfaces in equilibrium with an oxygen atmosphere at a given pressure p and temperature T [187, 188, 189, 185], is found by calculating the surface formation energy (per unit area) defined as

$$\begin{aligned}\gamma(T,p) = \frac{1}{A}[&G(T,p,N_{Zn},N_O) \\ &- N_{Zn}\mu_{Zn}(T,p) - N_O\mu_O(T,p)]\end{aligned} \tag{4.1}$$

Here $G(T,p,N_{Zn},N_O)$ is the Gibbs free energy of the system under investigation, μ_{Zn}, and μ_O are the chemical potentials for the Zn and O atomic species, respectively, N_O and N_{Zn} are the number of O and Zn atoms in the supercell and A the surface unit cell area. The most stable surface composition is the one that minimizes the surface energy.

Equation (4.1) does not directly apply to our models, because, as previously mentioned, the surface is modeled using a slab supercell with two different surfaces (atoms on one side fixed at their bulk positions). To get rid of the contribution of the "unrelaxed" side of the slab, we must subtract from Eq. (4.1) the surface formation energy $\gamma_{NR}(T,p)$ of the stoichiometric, unrelaxed surface, as follows:

$$\begin{aligned}\gamma(T,p) = \frac{1}{A}[&G(T,p,N_{Zn},N_O) \\ &- N_{Zn}\mu_{Zn}(T,p) - N_O\mu_O(T,p)] - \gamma_{NR}(T,p)\end{aligned} \tag{4.2}$$

where $\gamma_{NR}(T,p)$ is defined as

$$\begin{aligned}\gamma_{NR}(T,p) = \frac{1}{2A}[&G_{NR}(T,p,N_{Zn},N_O) \\ &- \bar{N}_{Zn}\mu_{Zn}(T,p) - \bar{N}_O\mu_O(T,p)]\end{aligned} \tag{4.3}$$

Here $G_{NR}(T,p,N_{Zn},N_O)$ is the Gibbs free energy of the unrelaxed slab (the factor of 2 arises because the unrelaxed slab contains two equivalent

surfaces). $\bar{N}_O$ and $\bar{N}_{Zn}$ are the number of O and Zn atoms in the supercell used to mimic the unrelaxed, stoichiometric surface and might differ from N_O and N_{Zn} when a defected slab is considered.

If there is enough bulk material to act as a thermodynamic reservoir, the chemical potentials of O and Zn in Eq. (4.2) are not independent, but related by the Gibbs free energy of the bulk oxide

$$\mu_{Zn}(T,p) + \mu_O(T,p) = g^{bulk}_{ZnO}(T,p) \tag{4.4}$$

where $g^{bulk}_{ZnO}(T,p)$ is the Gibbs free energy of bulk ZnO per formula unit. By inserting this constraint into Eq. (4.2) we obtain

$$\begin{aligned}\gamma(T,p) = \frac{1}{A}[G(T,p,N_{Zn},N_O) - N_{Zn}g^{bulk}_{ZnO}(T,p) \\ + N_{vac}\mu_O(T,p)] - \gamma_{NR}(T,p)\end{aligned} \tag{4.5}$$

This formula shows how the surface formation energy depends only on the oxygen chemical potential. In Eq. (4.5), $N_{vac} = N_{Zn} - N_O$ is the number of oxygen vacancies in the slab and is zero for the stoichiometric systems. It is important to note that experimentally μ_O and μ_{Zn} cannot be varied without bounds. Indeed, the O and Zn atoms are assumed to form no condensate on the surface. Consequently, the chemical potential of each species must be lower than the Gibbs free energy of an atom in the stable phase of the considered species

$$\begin{aligned}\Delta\mu_O(T,p) = \mu_O(T,p) - \frac{g^{mol}_{O_2}(T,p)}{2} < 0 \\ \Delta\mu_{Zn}(T,p) = \mu_{Zn}(T,p) - g^{bulk}_{Zn}(T,p) < 0\end{aligned} \tag{4.6}$$

In these inequalities, $\Delta\mu_{Zn}$ and $\Delta\mu_O$ are the variations of the chemical potentials with respect to the Gibbs free energy (per formula unit) of a Zn atom in the *hcp* bulk metal ($g^{bulk}_{Zn}(T,p)$) and of an O atom in the O_2 molecule in the gas phase ($g^{mol}_{O_2}(T,p)/2$), respectively. By combining Eqs. (4.4) and (4.6) we obtain

$$\Delta G^{bulk}_{ZnO}(T,p) < \Delta\mu_O(T,p) < 0 \tag{4.7}$$

where $\Delta G^{bulk}_{ZnO}(T,p) = g^{bulk}_{ZnO}(T,p) - g^{mol}_{O_2}(T,p)/2 - g^{bulk}_{Zn}(T,p)$ is the Gibbs free energy due to the formation of the bulk ZnO crystal starting from bulk Zn and molecular oxygen.

The described formalism is entirely based on the Gibbs free energies of the system, but it has been argued that the vibrational contribution to the Gibbs

free energy either can be neglected with respect to the other contributions or does not significantly affect the physical conclusions [185], even though in special situations such approximations might not be valid. Neglecting the vibrational contribution, the Gibbs free energies can be written in terms of DFT total energies so that the surface formation energy per unit of surface area is

$$\gamma(T,p) = \frac{1}{A}\left[E_{ZnO}^{slab} - N_{Zn}E_{ZnO}^{bulk} + N_{vac}\frac{E_{O_2}^{mol}}{2}\right] - \gamma_{NR} + \frac{N_{vac}\Delta\mu_O(T,p)}{A} \tag{4.8}$$

From Eq. (4.8) we observe that $\gamma(T,p)$ is a function of only $\Delta\mu_O(T,p)$ whose temperature and pressure dependence is defined by

$$\Delta\mu_O(T,p) = \Delta\mu_O(T,p^0) + \frac{1}{2}k_BTln(\frac{p}{p^0}) \tag{4.9}$$

where p^0=1 atm. The temperature dependence of $\Delta\mu_O(T,p^0)$ includes contributions from molecular vibration and rotations, as well as ideal-gas entropy at 1 atm pressure. These data can be found in thermodynamic tables [190]. Employing Eq. (4.9), one can provide the diagrams of the thermodynamic stability with a clear physical meaning behind the calculated curves.

We end this section by pointing out that for all stoichiometric and defected slabs, formation energy calculations are performed at the DFT level of the theory. Indeed, a complication arises when total DFT+U energies are used in calculations involving energy differences because of the need of calculating elemental reference energies, e.g., metallic bulk Zn and O_2 molecule in our case. On one hand, the appropriate U value for the Zn d states should be smaller in the metal than in ZnO, due to the difference in screening. On the other hand, total energies should in practice be compared only for the same U [191, 192]. Thus, the DFT+U vacancy formation energies might not be accurate, if different values of U are taken for the semiconductor and the metal.

4.1.3 Defect-annealing temperatures

Starting from the results for migration paths and energy barriers, we can discuss the temperatures at which we expect oxygen vacancies to become mobile.

According to transition state theory [157], an atom near a vacancy can jump into the vacancy overcoming an energy barrier E_b with a frequency

$$\Gamma = \Gamma_o \exp(-\frac{E_b}{k_BT}) \tag{4.10}$$

where the prefactor Γ_o is the ratio of the vibrational frequencies at the initial configuration to the frequencies at the saddle point, k_B is the Boltzmann constant, and T is the temperature. A reasonable estimate of the temperature at which the oxygen vacancy becomes mobile can be obtained by taking the usual definition of the active temperature, i.e., the temperature at which the jump rate Γ in Eq. (4.10) is 1 s^{-1}. To a good approximation Γ_o can be taken as a typical phonon frequency, i.e.,10^{13} s^{-1}. Therefore, we can use $\Gamma = 1$ s^{-1}, $\Gamma_o = 10^{13}$ s^{-1}, and the calculated E_b values for each path can be used to estimate the annealing temperature (this typically slightly overestimates the temperature at which oxygen vacancies become mobile).

4.2 Stoichiometric and defective ZnO surfaces

4.2.1 Clean ZnO $(10\bar{1}0)$ and ZnO $(11\bar{2}0)$ surfaces

The non–polar ZnO $(10\bar{1}0)$ and $(11\bar{2}0)$ surfaces are obtained by cutting the bulk crystal along planes parallel to the c axis. The respective surface geometries are sketched in Figure 4.2. While in the bulk, the Zn and O atoms are 4–fold coordinated, surface atoms at the $(10\bar{1}0)$ and $(11\bar{2}0)$ surfaces become 3–fold coordinated.

As far as the $(10\bar{1}0)$ surface is concerned, we can identify two potentially stable, stoichiometric surface terminations, namely, the A-plane and the B-plane terminations (see Fig. 4.2(a) for the definition of A and B planes). The two configurations have different geometries, in that while the first shows a "flat" geometry, the second results in a faceted structure. It has been shown that the flat, A-plane termination is the most stable one [193], therefore only results concerning such termination will be presented here. From our calculations, we obtained that the surface Zn and the uppermost O atoms relaxed into the surface by 0.341 Å and 0.003 Å, respectively (to be compared with the LEED experimental outcomes [111] of 0.3 ± 0.15 Å and 0.1 ± 0.05 Å). The surface relaxation leads to a shortening of the Zn–O bond at the surface (from 2.02 Å to 1.87 Å) and to a tilting of the Zn–O bond by 10.3°. This type of relaxation is limited to the surface atoms as indicated by the slight reduction of Zn–O bond length (from 2.02 Å to 2.01 Å) on the subsurface layer. As proposed by Mayer *et al.* [119], the shortening and the tilt can be attributed to two competing phenomena. For a given binary compound, when the surface bond is dominated by a covalent character, a rehybridization from sp^3 to sp^2 leads to a large tilt of the surface dimer (values as large as 30° are observed), with small to negligible variations of the bond length. On the other hand, in a ionic compound electrostatic

effects are dominant over rehybridization, which is reflected in significant bond length reduction but small tilt of the cation–anion dimer. In the specific case of ZnO, the relatively small tilt angle of 10.3° of the surface Zn–O dimer, together with the Zn–O bond length contraction of about 7%, confirm that the character of the chemical bond in ZnO is highly ionic but with a significant covalent contribution.

At variance with the previous case, the ZnO layer staking along the bulk $[11\bar{2}0]$ direction results in equivalent ZnO layers at a distance (in the ideal, bulk positions) of 1.65 Å (see Fig. 4.2(b)), therefore, only one possible surface termination can be identified, with two Zn–O dimers in the unit cell. After optimization, the Zn–O bond length for the two surface dimers reduces to 1.89 Å and 1.90 Å, with tilt angles of 7.7° and 7.6°, respectively. Therefore, only negligible differences are observed between the two dimers. Moreover, the bond length contraction and the relatively small tilt angle confirm the mixed covalent/ionic character previously discussed.

To get insight on the relative stability of the two surfaces, we compute the surface formation energy per unit surface area from Eq. (4.8) with $N_{vac} = 0$. Our estimates are 0.052 eV/Å^2 and 0.055 eV/Å^2 for the $(10\bar{1}0)$ and $(11\bar{2}0)$ surfaces, respectively. The (slightly) higher stability of the former agrees with the experimental findings. In particular, scanning tunneling microscopy studies [117, 53] showed, as a possible explanation of the lower stability of the $(11\bar{2}0)$ surface, the rougher morphology if compared with the $(10\bar{1}0)$ surface. Our results are compatible with the previous theoretical calculations of Meyer *et al.* [119] which use a symmetric slab model. On the other hand, a discrepancy is found with the results of Spencer *et al.* [194]. In the latter case, the authors use a slab model with fixed bottom layers (as that reported in the presented study) but use Eq. (4.1) instead of Eq. (4.2) to compute the surface formation energy, thus mixing the contributions coming from relaxed and the unrelaxed sides of the slab.

The band structures of both surfaces, calculated using the GGA+U approach, are reported in Figure 4.3(a). As a technical remark, we point out that, because we use an asymmetric slab model, some spurious intra-gap surface states show up, that are associated with the bulk-like side of the slab. For this reason, both the surface band structure and the total DOS have been obtained by retaining the only contributions coming from electronic states with a significant projection (> 0.2) onto the atomic orbitals associated to the uppermost surface layers (the ones that have been optimized during the calculations).

From Figure 4.3(a) we can note that the band edges (top valence band and bottom conduction bands) are both located at the Γ point of the 2D Brillouin zone. Surface states within the bulk band gap are highlighted as black stars in

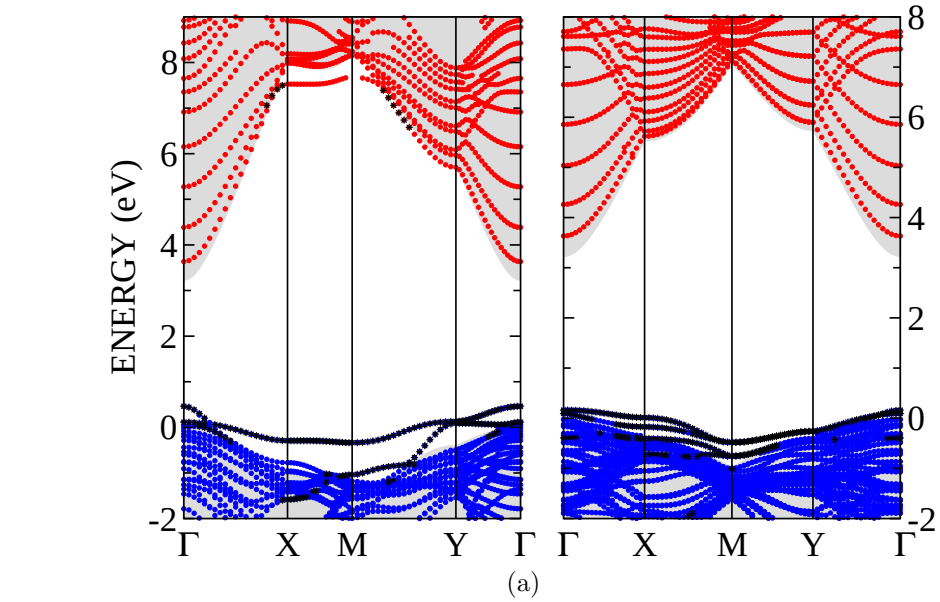

(a)

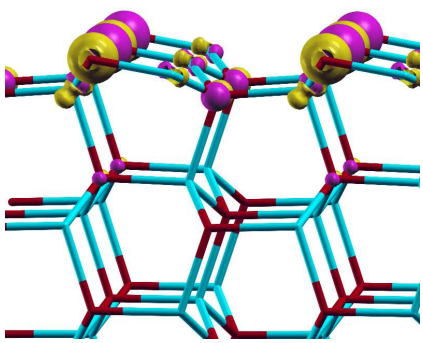

(b)

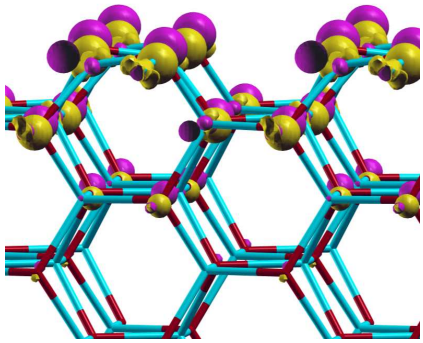

(c)

Figure 4.3: (a) Band structures of the ZnO $(10\bar{1}0)$ (left panel) and $(11\bar{2}0)$ (right panel) surfaces, calculated within the GGA+U approach. Occupied (unoccupied) bands are reported as blue (red) filled circles. The shaded regions correspond to the bulk band structure projected onto the surface two-dimensional BZ. The energy zero is set to the top bulk valence band. The black stars identify the slab electronic states with a significant projection ($>$ 0.4) onto the surface atomic orbitals. The relative line-up of the surface and bulk band structures is obtained by matching the macroscopically averaged self-consistent potential of the bulk crystal with that in the inner part of the slab [195]. Panels (b) and (c) show contour plots of the top valence band wave functions for the ZnO $(10\bar{1}0)$ and $(11\bar{2}0)$ surfaces, respectively (the contours correspond to a wave function amplitude of $\pm 16\%$ of its maximum value).

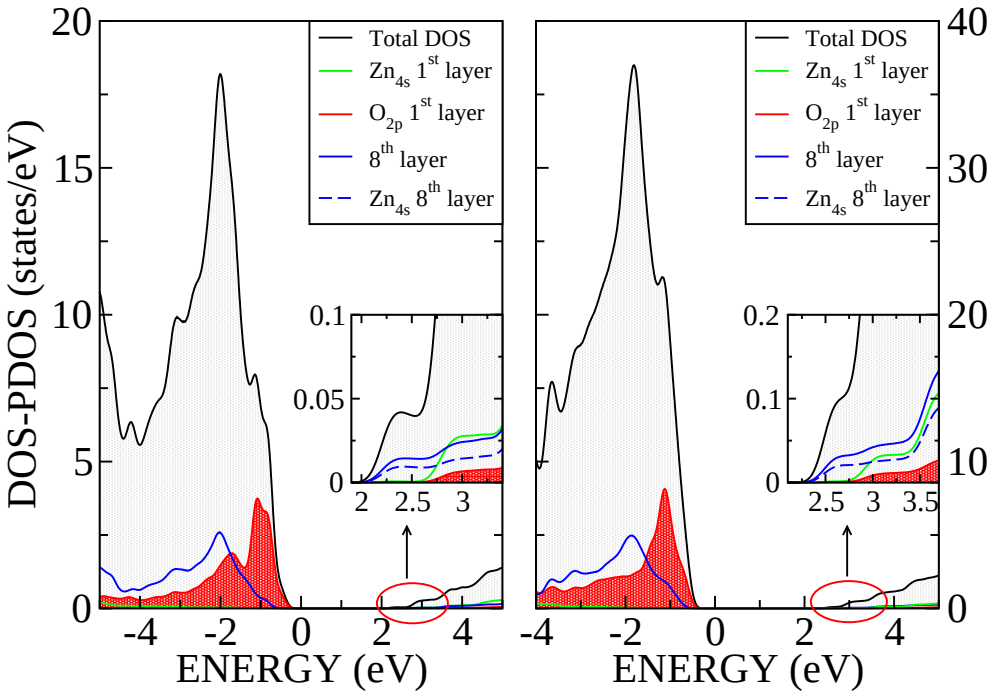

Figure 4.4: The PDOS in the near-gap region for the $(10\bar{1}0)$ and $(11\bar{2}0)$ surfaces (left and right panel, respectively). The insets show a zoom in proximity of the conduction band edge. The projections are made on: i) surface atomic orbitals (Zn 4*s* and O 2*p* states), ii) atomic orbitals belonging to a bulk-like layer (we choose the eighth layer and project onto either all the atomic orbitals or on only Zn 4*s* states belonging to it). This allows to distinguish between "surface" and "bulk" contributions, as well as between O and Zn atomic orbitals contributions. Figure taken from D'Amico *et al.* [184].

Figure 4.3(a) and are identified by evaluating the projection of the calculated band structure onto surface atomic orbitals. The surface localization of such states is also confirmed by the contour plots of the top valence band wave functions shown in Figures 4.3(b) and 4.3(c). When compared with the bulk value (3.31 eV), the direct band gap gets reduced (3.17 eV) for the $(10\bar{1}0)$ surface, whereas a larger value (3.47 eV) is obtained for the $(11\bar{2}0)$ surface.

The character of the near-gap states can be inferred from the analysis of the projected DOS (PDOS) on atomic orbitals shown in Figure 4.4. For both the $(10\bar{1}0)$ and $(11\bar{2}0)$ surfaces, the top valence band is mainly derived from the *p* orbitals of O atoms with Zn atoms giving no or negligible contribution. On the other hand, the bottom conduction band is strongly dominated by

the bulk contributions as seen in the Figure insets. These results are in agreement with recent first-principles studies [196].

4.2.2 Oxygen-deficient surfaces

We now have all the basic elements for discussing the effects due to oxygen vacancy. As far as the structural properties are concerned, the presence of a vacancy in the topmost layer induces an inward displacement of the unpaired Zn atom so as to restore a bulk-like fourfold coordination with the two neighbor Zn atoms of the second layer, in agreement with previous theoretical studies [193, 197, 198, 199]. Significant relaxation effects are also observed when the vacancy is located in the first two subsurface layers. For deeper vacancies, relaxation effects are more moderate and very similar to those observed in the defected bulk crystal. Moreover, the vacancy-induced distortions are mostly localized around the defect, whereas the geometry of the stoichiometric system is almost preserved in the regions far from the defect site.

A key issue in the applications of such surfaces in more complex systems, such as gas sensors and ZnO contacts, is given by the defect concentration and depth distribution (for example, such factors have been shown to play a role on the electronic processes occurring at ZnO Schottky barriers [38]). To get insight on this point, the vacancy formation energy, which measures the energy required to remove an oxygen atom from the stoichiometric surface, has been calculated as a function of the vacancy position with respect to the surface. This energy is defined as

$$E_{\mathrm{vf}} = E_{\mathrm{slab}} + N_{\mathrm{vac}} \times \frac{1}{2} E_{O_2} - E^{\mathrm{st}}_{\mathrm{slab}} \tag{4.11}$$

where E_{slab} and E^{st}_{slab} are the DFT total energies of the slab containing the defect(s) and of the stoichiometric slab, respectively.

The computed values of E_{vf} as a function of the oxygen vacancy position and for a defect concentration of 25% are plotted in Figure 4.5(a). The surface vacancy corresponds to 0 Å depth and has the lowest formation energy (2.84 eV and 2.72 eV for the $(10\bar{1}0)$ and $(11\bar{2}0)$ surfaces, respectively). Higher formation energies are obtained for deeper positions of the vacancy (for example 3.32 eV and 3.37 eV for sub–surface vacancies in the $(10\bar{1}0)$ and $(11\bar{2}0)$ surface, respectively), monotonically approaching the bulk limit of 3.64 eV for sufficiently deep sites (even in the case of the $(10\bar{1}0)$ surface in which, as previously mentioned, an A–B stacking of the atomic planes can be identified).

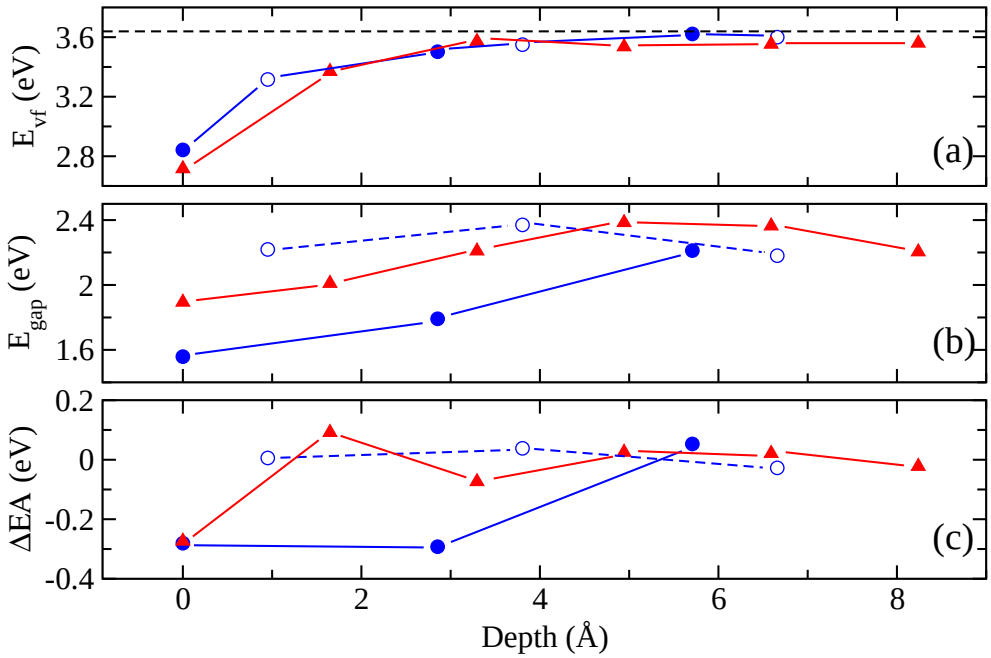

Figure 4.5: (a) Vacancy formation energy $E_{\rm vf}$, (b) energy gap $E_{\rm gap}$ and (c) electron affinity variation with respect to the stoichiometric surface (ΔEA) as a function of the defect depth (Å) in the slab. The origin on the abscissa is at the position of the surface vacancy. Circles and triangles distinguish the two different surface orientations ($(10\bar{1}0)$ and $(11\bar{2}0)$, respectively) while full and empty circles distinguish, for the $(10\bar{1}0)$ slab, the vacancy in the A or B planes, respectively. The black dotted line corresponds to the formation energy of a bulk oxygen vacancy. The defect concentration is 25% (larger unit cells, corresponding to 11% and 12% defect concentration for the two surfaces, respectively, give rise to $E_{\rm vf}$ and ΔEA variations by only 0.1 eV). Figure taken from D'Amico *et al.* [184].

In Figures 4.6(a) and 4.6(b) we show the band structure (calculated using the GGA+U approach) of the ZnO $(10\bar{1}0)$ and $(11\bar{2}0)$ surfaces in the presence of a single oxygen vacancy in the supercell (with a concentration of 11% and 12%, respectively). The presence of the defect is responsible for the appearance of an occupied dispersionless band which is located about 2 eV above the bulk crystal top valence band. Such a band, as revealed by the PDOS analysis, is mainly derived from the Zn_{4s} atomic orbitals belonging to the atoms surrounding the vacancy, with a smaller contribution coming from O_{2p} orbitals of the atoms closest to the vacancy itself. This is confirmed

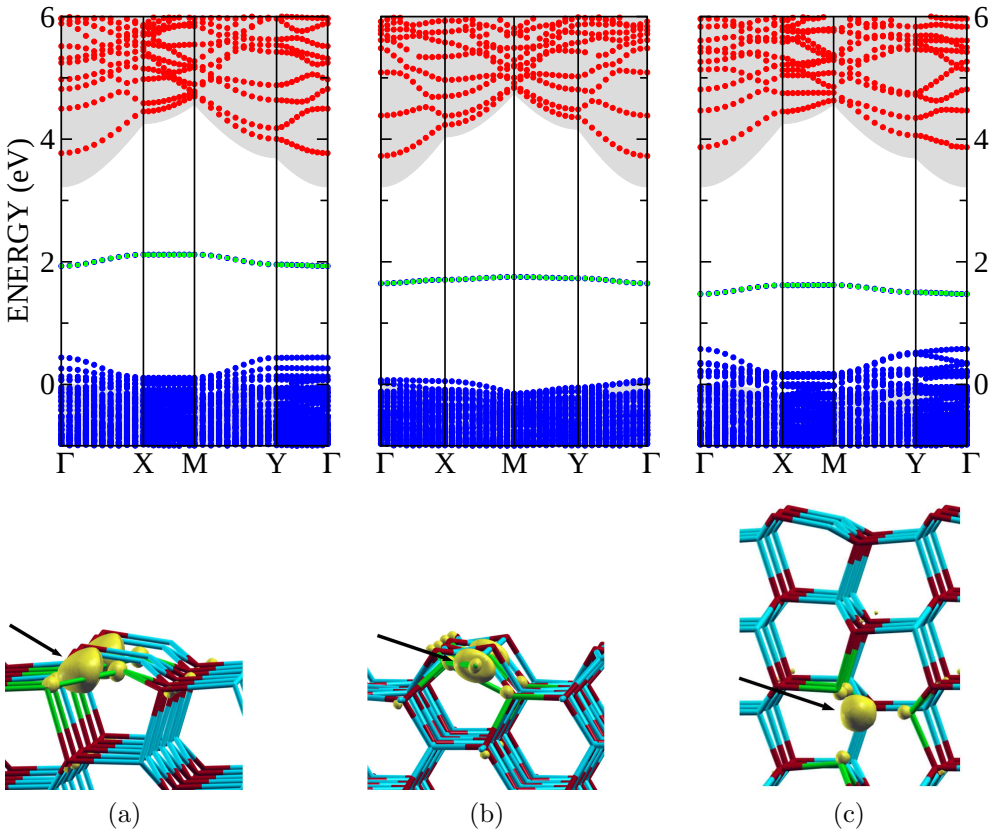

Figure 4.6: Band structures calculated within the GGA+U approach (top panels) and contour plots of the square modulus of the defect band wave function (at Γ point) (bottom panels) for (a) the ZnO $(10\bar{1}0)$ surface with an oxygen vacancy in the surface layer, (b) the ZnO $(11\bar{2}0)$ surface with an oxygen vacancy in the surface layer, and (c) the ZnO $(10\bar{1}0)$ surface with an oxygen vacancy in the sixth layer. The vacancy concentration is 11% in (a) and (c) and 12% in (b). Occupied (unoccupied) bands are reported as blue (red) filled circles. The green square symbols identify the electronic levels with a significant projection (> 0.4) on the atomic orbitals of the Zn atoms surrounding the vacancy. The shaded regions correspond to the bulk band structure projected onto the surface two-dimensional BZ. The energy zero is set to the top bulk valence band. In all cases the almost flat band around $\sim$2 eV corresponds to a defect electronic level. The contours correspond to a density equal to 15% of the maximum value and the arrows mark the defect position. Figure taken from D'Amico *et al.* [184].

by the electron charge density distribution of the defect states. The contour plot of the square modulus of the defect band wave function (calculated at

Γ point), reported in the bottom panels of the same figure, clearly shows a localized character, with the majority of the wave function around the defect site. A qualitatively similar behaviour is found when the defect occupies deeper positions. As an example, we show in Figure 4.6(c) the band structure of the $(10\bar{1}0)$ surface with a single vacancy in the sixth atomic layer (11% vacancy concentration). As with the surface vacancy, a defect level appears within the bulk band gap. The only significant difference is a downwards shift of the defect band as the vacancy approaches bulk-like positions. Moreover, as revealed by the bottom panel of the same figure, the localized character of the defect-related electronic levels gets more pronounced.

The calculated energy gap E_{gap} as a function of the vacancy depth is reported in Figure 4.5(b). E_{gap} is strongly influenced by the hybridization of the atomic orbitals surrounding the vacancy, which explains its dependence on the vacancy site. In particular, a moderate dependence on the depth is found for O vacancies in the B planes of the $(10\bar{1}0)$ surface, whereas a more significant dependence is found when the vacancy is located within the A planes of the $(10\bar{1}0)$ surface or for the $(11\bar{2}0)$ surface. This is a signature of how the atomic relaxation around the point defect is not the same for all the investigated systems, leading to different positions of the lowest occupied and highest unoccupied electronic levels.

We have also investigated the electron affinity (EA) variations with respect to the stoichiometric surfaces (ΔEA) induced by the presence of the O vacancies [see Fig. 4.5(c)]. The electron affinity can be easily calculated once the vacuum level has been determined from the self-consistent electrostatic potential [195]. The results for the stoichiometric ZnO $(10\bar{1}0)$ and $(11\bar{2}0)$ surfaces are 5.34 eV and 5.49 eV, respectively. It is seen from Figure 4.5(c) that only surface and, to a smaller extent, subsurface oxygen vacancies can induce changes of the EA. In particular, we observe considerable EA variation (-0.28 eV and -0.27 eV for the $(10\bar{1}0)$ and $(11\bar{2}0)$ surfaces, respectively) in the presence of surface vacancies. O vacancies in the B planes of the $(10\bar{1}0)$ surface produce only small EA variations. Moreover, it can be noticed that the presence of an oxygen vacancy in the A plane of $(10\bar{1}0)$ surface at a depth of 2.85 Å induces EA changes as large as -0.29 eV. As with the energy gap, the EA variations bring the signature of different atomic rearrangement around the point defect as a function of its depth.

As a last point of this section, we want to compare the stability of the investigated surfaces under experimental conditions. With this aim, we consider surfaces with different vacancy concentrations, assumed to be in equilibrium with an external environment (molecular oxygen in gas phase). The quantity to be computed is the surface formation energy per unit area, Eq. (4.8) which, at variance with the stoichiometric surface, depends on

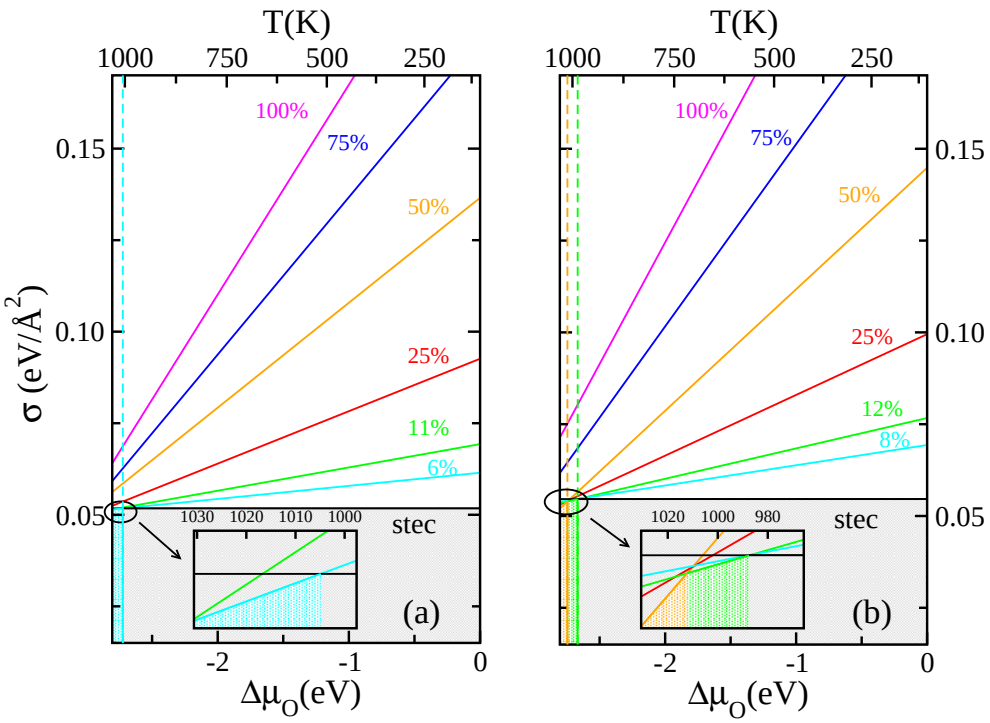

Figure 4.7: Surface free energies for the non-polar ZnO $(10\bar{1}0)$ [left panel] and $(11\bar{2}0)$ [right panel] surfaces as a function of the oxygen chemical potential. Different surface vacancy concentrations are considered. The top axis shows, according to Eq. (4.9), the conversion of the chemical potential range to temperature for an oxygen gas partial pressure of $\sim 10^{-10}$ atm. The insets show a magnification of the temperature range where the defective surface is thermodynamically more stable than the defect-free surface. Figure taken from D'Amico *et al.* [184].

$\Delta\mu_O(T,p)$ which is a function of temperature and pressure [Eq. (4.9)].

The lower bound for $\Delta\mu_O(T,p)$ is given by the formation energy of the bulk ZnO crystal E_f^{ZnO} (referred to the bulk Zn crystal and molecular oxygen in the gas phase). We estimate $E_f^{ZnO} = -2.80$ eV, in agreement with previous theoretical calculations [41, 200]. The given estimation of $E_f^{ZnO} = -2.80$ eV does not match the experimental value (-3.63 eV, measured at $T = 298$ K and $p = 1$ bar [190]). The discrepancy arises from using the DFT total energy of the O_2 molecule, which is well-known to be severely underestimated in DFT-PBE. Another possible route, pursued in the literature, is that the total energy of the O_2 molecule is chosen in such a way that, combined with the DFT-PBE total energies of bulk metallic Zn and bulk ZnO, the experimental value of E_f^{ZnO} is correctly predicted [201, 49]. In this case,

because the formation energy of an O vacancy becomes larger but the range of allowed chemical potentials (horizontal axis in Figure 4.7) is wider, the same (qualitative) results for surface stabilities are obtained, because all the thermodynamic plots are shifted towards high temperatures.

In Figure 4.7 we show the surface formation energy per unit surface area of stoichiometric and defected surfaces as a function of $\Delta\mu_O(T,p)$ for several reduction percentages. Only surface defects are considered. The top horizontal axis reports, according to Eq. (4.9), the conversion scale of the chemical potential (bottom horizontal axis) to temperature, for an oxygen partial pressure of 10^{-10} atm.

The results show that, at variance with other oxide materials and other ZnO surface terminations, the stoichiometric surface is thermodynamically the most stable over most of the temperature range (if we use instead the total energy of the O_2 molecule as obtained from the experimental measurements of E_f^{ZnO}, the stability of the defected surface at the lowest considered vacancy concentration occurs at $\sim$1250 K). Only for sufficiently low vacancy concentrations, ultra-high vacuum conditions and high temperature ($\sim$1000 K in Figure 4.7) the defected system can become more stable. While these pressure/temperature conditions under which defects are stable might be considered too severe, it should be noticed that under similar conditions Göpel and Lampe [51, 52] were able to obtain thermodynamically stable ZnO $(10\bar{1}0)$ surfaces in the presence of oxygen vacancies. In particular, intrinsic point defect were intentionally induced, with a maximum coverage of 10^{-2}, by pursuing several routes, including: i) high-temperature treatment and subsequent cooling down under ultrahigh vacuum conditions, ii) UV illumination, leading to thermally activated desorption of oxygen atoms, iii) in the absence of UV light, by CO exposure and subsequent CO_2 desorption. Of course, the surface defects could only be frozen in the absence of O_2, since they react rapidly with oxygen even at low temperature (T $\leq$ 700 K). In the same experiment, fundamental effects induced by the presence of oxygen vacancies, such as the formation of strong accumulation layers, surface free carriers, variations in rates of charge transfer, were extensively characterized. It should be pointed out that more recent studies, based on atomically resolved STM experiments [53, 54], have found no signature of the presence of oxygen defects on the same surface. As far as we can understand, the different conclusions might originate from different preparation conditions. In other words, while it is not likely to find significant concentrations of defects on the surfaces under investigation under "ordinary" temperature and pressure conditions, it is possible to intentionally induce such defects if suitable preparation conditions are met.

A last question concerns the possibility of observing other kind of defects,

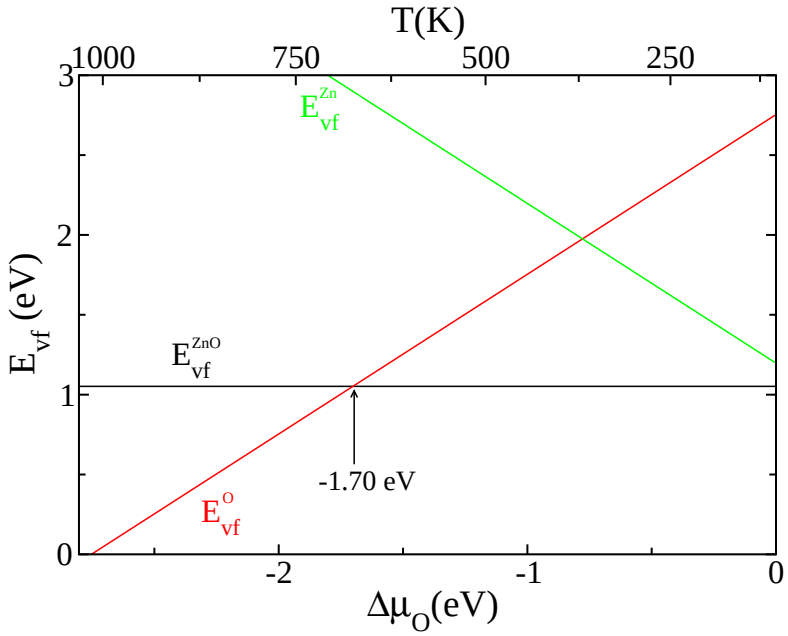

Figure 4.8: The formation energy of a ZnO dimer (black line), a Zn vacancy (green line) and an O vacancy (red line) on the ZnO $(10\bar{1}0)$ as a function of the oxygen chemical potential. All the energies are referred to the stoichiometric, clean surface. As with Eq. (4.11), which defines the O vacancy formation energy, we define the formation energy of a single ZnO dimer and a Zn vacancy respectively as $E_{\rm vf}^{\rm ZnO} = E_{\rm slab} + E_{\rm ZnO}^{\rm bulk} - E_{\rm slab}^{\rm st}$ and $E_{\rm vf}^{\rm Zn} = E_{\rm slab} + E_{\rm ZnO}^{\rm bulk} - \frac{1}{2}E_{O_2} - E_{\rm slab}^{\rm st}$. The top horizontal axis reports, according to Eq. (4.9), the conversion scale of the chemical potential (bottom horizontal axis) to temperature, for an oxygen partial pressure of 10^{-10} atm. Figure taken from D'Amico *et al.* [184].

such as a missing ZnO dimer or a Zn vacancy. Such a possibility has been theoretically argued for [49] and has been given some evidence by recent experiments [54]. To get more insight, in Figure (4.8) we compare, for the $(10\bar{1}0)$ surface (3×3 unit cell), the defect formation energy (with respect to the stoichiometric surface) of a surface oxygen vacancy, Zn vacancy and ZnO vacancy as a function of the oxygen chemical potential. The $E_{\rm vf} = 0$ axis corresponds to the stoichiometric surface. The results show that while, as previously discussed, extremely reducing conditions are needed for the defected surface to become more stable, the same condition cannot be met in the presence of the Zn or ZnO vacancies. Moreover, at sufficiently high temperatures (∼700 K in the shown example), the O vacancy is the most stable defect, in agreement with previous results [49]. Finally, it should be noticed

that, within the approximation of the present calculations, even strongly oxidizing conditions are not enough for the Zn vacancy to be more stable than either the other defects or the stoichiometric system. As previously observed, if we use instead the total energy of the O_2 molecule as obtained from the experimental measurements of E_f^{ZnO}, the shift of the thermodynamic plots to high temperature is such that, in the O-rich limit (low temperature limit) the Zn vacancy can become stable in a small temperature range [49], up to $\sim$250 K in the example of Figure 4.8.

4.3 Diffusion mechanisms of O vacancy

The diffusion mechanism of oxygen and zinc vacancies in the bulk ZnO crystal is technologically important, and it has been extensively investigated [46, 47, 48, 202, 203]. On the other hand, the diffusion of oxygen vacancies in proximity of ZnO surfaces has been less investigated [204]. The results of the previous sections allow us to conclude that the formation of vacancies on the ZnO surfaces of interest for the present work is likely only under quite stringent experimental conditions. This implies that a vacancy in proximity of the surface will immediately recombine with ambient oxygen under ordinary conditions. Nevertheless, it is legitimate to wonder what happens to a defect which has been created in deeper positions. The magnitude of the diffusion barriers might induce defect migration (and successive recombination) of the defect towards the surface or prevent such a mechanism. In particular, it is relevant to point out possible differences arising in the diffusion pathways within planes parallel to the surface or along the direction orthogonal to it.

As far as the oxygen vacancy diffusion in the bulk crystal is concerned, we have considered only the paths connecting first neighbor oxygen sites because they correspond to the lowest energy barriers. Among the possible vacancy jumps, there are six symmetric equivalent paths parallel to the (0001) plane and six equivalent paths with components parallel to the [0001] axis. For an ideal *hcp* lattice ($c/a = \sqrt{8/3} = 1.633$) all these paths are equivalent but in the ZnO they are different because the axial ratio of the oxygen *hcp* sublattice is slightly smaller than the ideal one ($c/a = 1.606$). Therefore, the two above-mentioned sets of paths will be referred to as in-plane (IN) and out-of-plane (OUT), respectively.

The calculated diffusion pathways are shown in Figure 4.9 while the diffusion barriers and the estimated annealing temperatures are reported in Table 4.2. A $2\times2\times2$ BZ sampling has been employed in these calculations to reduce the computational cost (we have verified that a better BZ sampling produces

Table 4.2: Calculated migration barrier E_b and estimated annealing temperature T_a for the oxygen vacancy hopping between first neighbor sites in the bulk ZnO crystal. Previous literature results are also reported for comparison.

	This work		Ref. 46	Ref. 47	Ref. 48
	$E_b(eV)$	$T_a(K)$	$E_b(eV)$	$E_b(eV)$	$E_b(eV)$
IN	2.00	775	1.87	2.36	2.06
OUT	2.27	880	2.55	2.36	2.34

no significant changes in the computed paths). The OUT path shows an higher barrier, of about 0.3 eV, than the IN path. Such small anisotropies in the migration barriers are expected since, as pointed out, the local geometry around the oxygen vacancy has an almost, but not full tetrahedral symmetry.

From Table 4.2 we can see that the oxygen vacancies become mobile only at high temperature, in agreement with the experimental findings [205, 206] showing that oxygen vacancies are stable up to $\sim$ 670 K. In Table 4.2 we also show previous theoretical calculations of the diffusion barriers. While

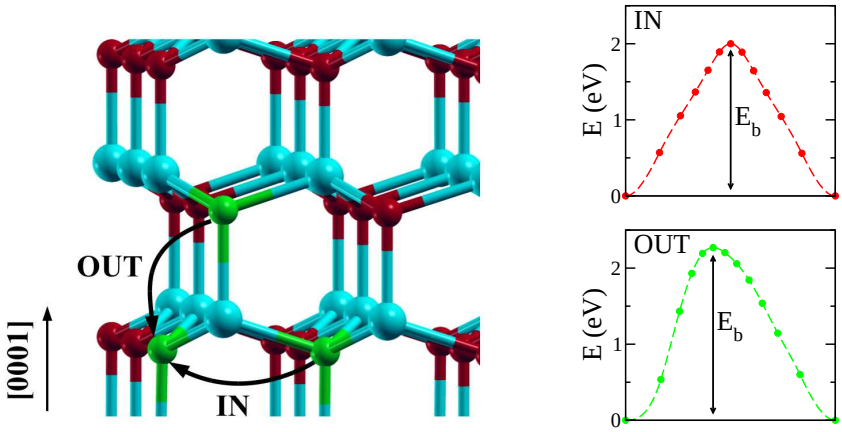

Figure 4.9: Schematic illustration (left panel) of diffusion paths (right panels) for oxygen vacancies in the wurtzite lattice. IN and OUT denote, respectively, the in-plane diffusion path within the (0001) plane and out-of-plane diffusion with component parallel to the [0001] axis. Only vacancy hopping between first-neighbor oxygen sites is investigated. The green spheres represent the oxygen sites involved in the two diffusion paths whereas the blue (red) spheres represent the other zinc (oxygen) atoms. Figure taken from D'Amico *et al.* [184].

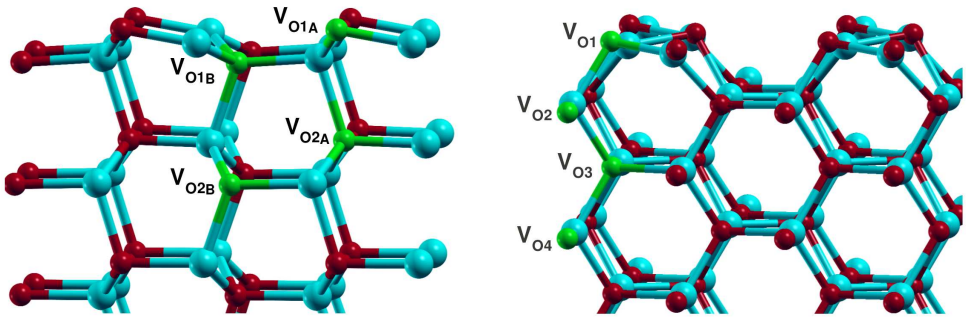

Figure 4.10: Oxygen vacancy sites (highlighted in green) considered as possible hopping sites in the vacancy diffusion process. The migration paths of Table 4.3 and Table 4.4 connect pairs of these sites. Left and right panels are for the $(10\bar{1}0)$ and $(11\bar{2}0)$ surfaces, respectively. Figure taken from D'Amico *et al.* [184].

our results agree with those reported in Ref. 48, it can be noticed that Erhart and Albe [46] find differences as large as 0.7 eV between migration barriers along the IN and OUT pathways. As already suggested by Janotti and Van de Walle [47], we have verified (by directly reproducing the calculation) that the discrepancy arises from the small supercell (32 atoms) used in Ref. 46, which does not guarantee full convergence of the calculated barriers.

Due to computational issues, for the vacancy diffusion in proximity of the $(10\bar{1}0)$ and $(11\bar{2}0)$ surfaces we have used an 8 atomic layer model with the atoms in the two bottom layers anchored to their bulk positions. No significant changes in the calculated energy barriers have been observed in

Table 4.3: Calculated migration barrier E_b and estimated annealing temperature T_a for the vacancy diffusion process across the $(10\bar{1}0)$ ZnO surface. The oxygen vacancy sites are defined in Figure 4.10, left panel.

	E_b (eV)		$T_a(K)$	
	direct	inverse	direct	inverse
$V_{O1_A} \rightarrow V_{O1_A}$	1.265	1.265	490	490
$V_{O1_B} \rightarrow V_{O1_B}$	1.721	1.721	667	667
$V_{O2_A} \rightarrow V_{O2_A}$	1.416	1.416	549	549
$V_{O2_B} \rightarrow V_{O2_B}$	1.955	1.955	757	757
$V_{O1_A} \rightarrow V_{O1_B}$	2.099	1.639	814	635
$V_{O1_A} \rightarrow V_{O2_A}$	1.901	1.240	737	481

Table 4.4: Calculated migration barrier E_b and estimated annealing temperature T_a for the vacancy diffusion process across the $(11\bar{2}0)$ ZnO surface. The oxygen vacancy sites are defined in Figure 4.10, right panel.

	E_b (eV)		$T_a(K)$	
	direct	inverse	direct	inverse
$V_{O1} \rightarrow V_{O1}$	1.224	1.224	474	474
$V_{O2} \rightarrow V_{O2}$	2.251	2.251	873	873
$V_{O3} \rightarrow V_{O3}$	1.766	1.766	685	685
$V_{O4} \rightarrow V_{O4}$	2.047	2.047	793	793
$V_{O1} \rightarrow V_{O2}$	2.154	1.501	835	582
$V_{O1} \rightarrow V_{O3}$	2.312	1.449	896	562

test cases where a 12 atomic layer slab model has been employed. 4×3 and 2×4 k-point meshes have been used to sample the two-dimensional BZ of the ZnO $(10\bar{1}0)$ and $(11\bar{2}0)$ surface supercells, respectively.

We consider different oxygen sites within the slab as possible hopping centers (see Fig. 4.10), so as to bring out differences between migration processes occurring either within a given atomic layer or across different atomic layers. We report the barriers along the most favorable pathways together with the estimated annealing temperatures in Table 4.3 and Table 4.4 for the $(10\bar{1}0)$ and $(11\bar{2}0)$ surfaces, respectively. Direct and inverse barriers refer to asymmetric paths, connecting local minima with different energies.

The results show that, for both surfaces, the most favored diffusion process occurs within the surface layer (with a migration barrier of about 1.2 eV). On the other hand, in-plane (namely, parallel to the surface) diffusion processes within the subsurface layers are much more unlikely, being driven by energy barriers as large as 1.7–2.0 eV (see the $V_{O1_B} \rightarrow V_{O1_B}$, $V_{O2_A} \rightarrow V_{O2_A}$, $V_{O2_B} \rightarrow V_{O2_B}$ and $V_{O2} \rightarrow V_{O2}$, $V_{O3} \rightarrow V_{O3}$, $V_{O4} \rightarrow V_{O4}$ paths in Table 4.3 and Table 4.4, respectively). Interestingly, the in-plane diffusion barrier is not a monotonic function of the depth. This is shown in Figure 4.11, where the variation of E_b as a function of the atomic layer depth is plotted. It can be easily argued that the considered diffusion paths for the $(10\bar{1}0)$ and $(11\bar{2}0)$ surfaces would correspond to the previously discussed IN and OUT paths in the bulk crystal, respectively. For this reason, the two panels of Figure 4.11 show different bulk limits (see Table 4.2), which are approached as the atomic layer depth increases.

As far as out-of-plane (namely, across different atomic layers) migration processes are concerned, we observe that the diffusion from the surface to

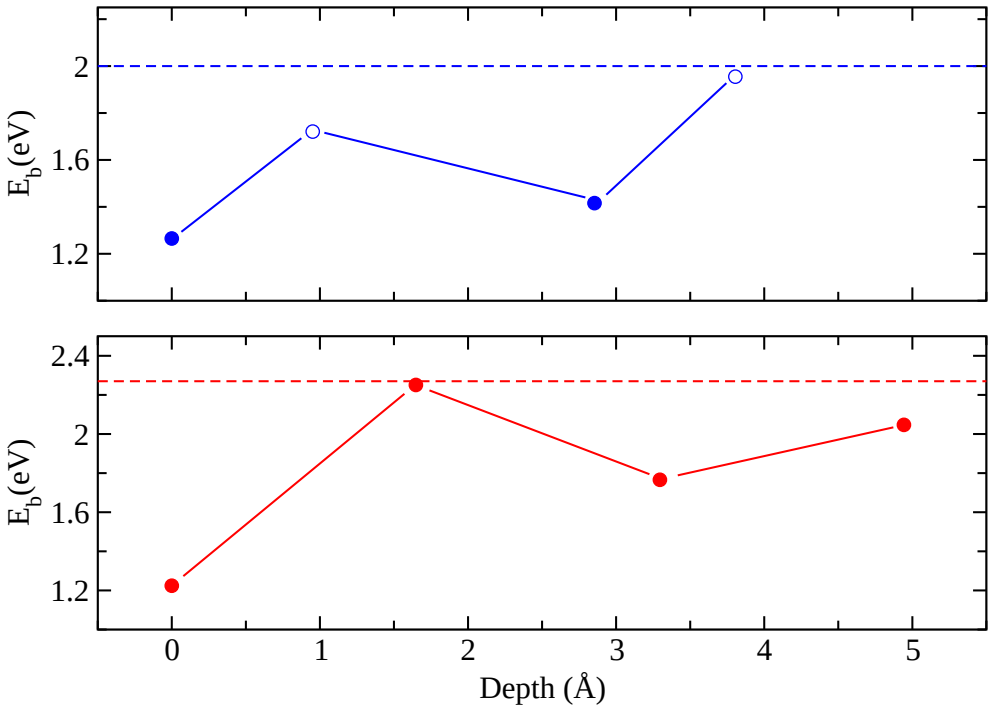

Figure 4.11: In-plane diffusion barrier E_b for the $(10\bar{1}0)$ (top panel) and $(11\bar{2}0)$ (bottom panel) surfaces as a function of the layer depth. The dashed lines correspond to the bulk limit (IN and OUT paths of Table 4.2 for the two surfaces, respectively). Figure taken from D'Amico *et al.* [184].

the subsurface ($V_{O1_A} \rightarrow V_{O1_B}$, $V_{O1_A} \rightarrow V_{O2_A}$, $V_{O1} \rightarrow V_{O2}$ and $V_{O1} \rightarrow V_{O3}$ paths) appears to be largely inhibited (E_b ∼2.0 eV). Smaller barriers are found for the inverse process (subsurface to surface diffusion) with the $V_{O2_A} \rightarrow V_{O1_A}$ process showing a barrier (∼ 1.2 eV) comparable with the surface, in-plane diffusion barrier. Therefore, we can conclude that the most likely migration processes correspond to the vacancy hopping in the surface layer (with typical activation temperature less than 500 K).

To conclude this section, we show in Figure 4.12 the calculated potential energy profile and selected NEB images for the $V_{O1} \rightarrow V_{O1}$ in-plane diffusion pathway of an oxygen vacancy parallel to the $(11\bar{2}0)$ surface. In this specific case, a metastable state (local minimum) is found. The presence of such minimum has been further checked by optimizing a nearby structure (image 6) of the metastable state. The structure relaxed indeed to a configuration having 0.31 eV higher energy than initial and final state of the pathway, confirming the reliability of the metastable state.

4.4 Conclusions

A theoretical study of the non-polar ZnO $(10\bar{1}0)$ and $(11\bar{2}0)$ surfaces has been carried out in the framework of density functional theory, in connection with possible applications in sensor devices and other smart systems. Since anion deficiency is known to play a major role in the physical and chemical properties of most functional oxides and their interfaces, we have focused on the effects of both surface and subsurface oxygen vacancies on the structural and electronic properties. In particular, we have addressed the dependence of such properties on the position of the defect with respect to the surface. Moreover since the diffusion kinetics of point defects also plays a fundamental role in technological applications, we have also characterized the migration paths of oxygen vacancies parallel or across the surface using the climbing image nudged elastic band method. The main properties that we highlighted are summarized in the following.

- Under exposure to molecular oxygen in the gas phase, no significant amounts of oxygen vacancies can be sustained by the ZnO non-polar $(10\bar{1}0)$ and $(11\bar{2}0)$ surfaces, in agreement with recent Scanning Tunnelling Microscope (STM) observations. However, our calculations

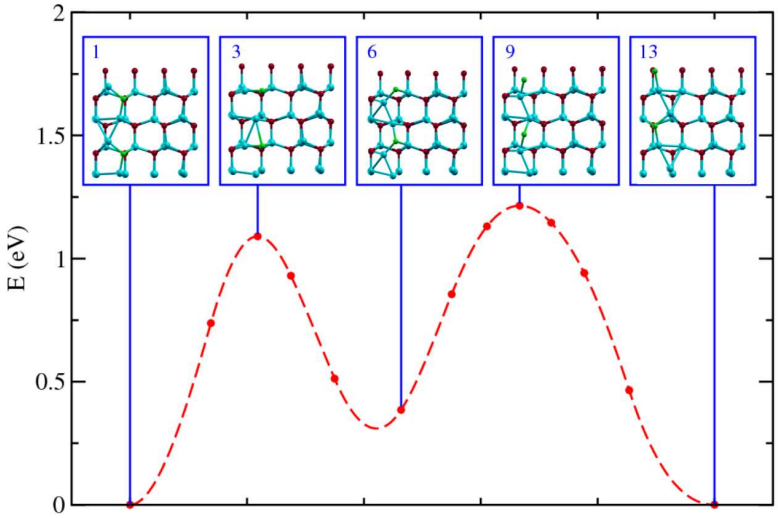

Figure 4.12: Potential energy profile of the $V_{O1}\rightarrow V_{O1}$ diffusion pathway. The insets show selected NEB images along the pathway. The oxygen atoms which undergo the larger displacements in the diffusion process are in green, while the zinc atoms and the other oxygen atoms are in blue and red, respectively. Figure taken from D'Amico *et al.* [184].

have also shown that under ultrahigh vacuum and high temperature conditions, the observation of oxygen vacancies might be possible, as reported in earlier experiments of Göpel and Lampe [51].

- By comparing the energetics of three kind of defects (O, Zn and ZnO vacancies), we have shown that, differently from the O vacancy, there are no pressure and temperature conditions under which the Zn and ZnO vacancy defects get more stable than the stoichiometric surface. In particular even strongly oxidizing conditions are not enough for the Zn vacancy to be more stable than the other defects or the stoichiometric system.

- The oxygen vacancies are responsible for the appearance of an occupied dispersionless band with a "localized" character around the oxygen vacancy. Moreover the energy of the defect state depends on the position of the oxygen vacancy inside the material.

- The surface gap energy and electron affinity can be significantly altered by the presence of the oxygen vacancy and strongly depend on its position with respect to the surface.

- The oxygen vacancies diffuse much more easily in the surface layer than in the bulk. In particular the surface oxygen vacancies become mobile at relatively modest temperatures ($490K$ and $481K$ for the ZnO $(10\bar{1}0)$ and $(11\bar{2}0)$ surfaces, respectively).

- Migration paths in the direction orthogonal to the surface show asymmetric barriers, which are smaller (by 0.5–0.9 eV) in the direction toward the surface. Thus it is favored the diffusion from subsurface layers to the surface.

Chapter 5

$SrTiO_3$–TiO_2 interface

Semiconductor–semiconductor and metal–semiconductor interfaces play a crucial role in modern electronic and optoelectronic devices. In particular, the transport properties in heterojunction devices are controlled by the electronic band profiles at the interfaces, more specifically by the valence and conduction discontinuities that accommodate the difference in bandgap between the materials, namely, the valence and conduction band offsets (VBO and CBO) in the case of semiconductor heterojunctions and the p- and n-type Schottky barriers (ϕ_p and ϕ_n) in the case of metal–semiconductor contacts (Fig. 5.1).

Extensive theoretical and experimental work has targeted the problem of the interface band alignment [207, 208, 209, 210, 211]. However, it is only in the last two decades that the physical mechanisms which give rise to the band alignment at semiconductor heterojunctions have begun to be revealed [207, 208, 209] and that the connection between band offsets and Schottky barriers has been put on a firmer basis [207, 208, 212]. Today we are still far from a complete understanding of the factors which control the band alignment, especially in the case of Schottky barriers.

In this chapter we have limited our attention on the $SrTiO_3$–TiO_2 interface. This interface has been extensively investigated [59, 60, 61, 62, 63]. Ohta *et al.* [64] claimed that the $SrTiO_3$–TiO_2 interface grown by pulsed laser deposition exhibits 2D electron gas (2DEG) behaviour and they posited that the oxygen vacancies can be considered responsible of the presence of the 2DEG. The band alignment of this interface was measured from Chambers *et al.* [65]. They used high-energy resolution X-ray photoelectron spectroscopy and their measurements revealed a VBO ranging between -0.06 eV and $+0.16$ eV for anatase thicknesses between 1 and 8 monolayers [214, 65]. Curiously, in contradiction with the XPS result, their density functional theory (DFT) calculations suggested a valence band offset of 0.5 eV. This difference

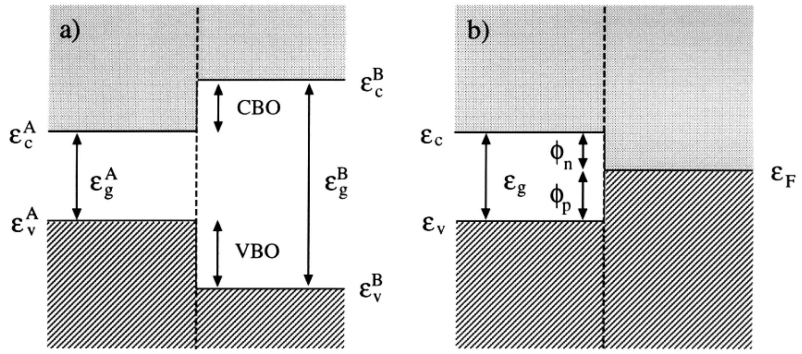

Figure 5.1: Schematic diagrams of the band structures of semiconductor–semiconductor (a) and semiconductor–metal (b) junctions, as a function of the position along the growth direction. Definitions of band offsets (VBO and CBO) and of Schottky barriers (ϕ_p and ϕ_n) are shown. Flat bands were represented, because we are focusing on a region which is of the order of 10 atomic units and the band bending is negligible at this scale. Figure taken from Peressi *et al.* [213].

between theoretical and experimental results could be interpreted either as the inability of DFT to fully account for the interface properties or that the atomic structure used in the calculation differs from the experimental one.

In this chapter we try to shed light on the discrepancy between experimental and theoretical results, through a detailed first principles study aimed to gaining insight on the role played by oxygen vacancies in the near-interface region.

This chapter is organized as follows. In Sec. 5.1 we describe the different theoretical techniques used to obtain the valence band offset (VBO) and conduction band offset (CBO). In Sec. 5.2 the computation details on the performed calculations are summarizes. The Sec. 5.3 shows the results for the ideal and defected $SrTiO_3$–TiO_2 interface. Finally, in Sec. 5.4 some conclusions are drawn.

5.1 Band offset

In this section we present a brief summary of various techniques employed for the study of band offset. These different approaches are based on the pseudopotential method, which is an efficient approach, within the LDA(or GGA)-SCF framework, for dealing with semiconductors and metals of practical interest for electronic devices. In particular, a numerical uncertainty

of a few milli-electronvolts can be typically achieved in LDA(or GGA)-SCF calculations of the band line-ups by controlling the convergence with respect to several parameters such as the number of plane waves in the basis set, the k points used and the size of the supercell describing the junction. Other sources of uncertainty are the choice of the pseudopotentials and the resulting lattice parameters used in the calculations; the global numerical uncertainty in the band alignments can be estimated to be of the order of 20-30 meV for fully converged calculations.[1]

5.1.1 Macroscopic average technique

Interfaces can be studied using periodically repeated supercells, which allow for a convenient reciprocal space formulation of the problem, which is otherwise not possible because of the loss of translational symmetry. Insofar as the bandstructure alignments are concerned, experience has shown that the relevant effects due to the presence of a neutral interface are confined to a small region and the bulk features of the charge density are completely recovered within a few atomic units far from the interface. This implies that the relevant interface features can be studied using supercells with a reasonably small number of atoms (a few atomic planes of each material). However, in general, the isolated interface configuration is well represented, provided that the adjacent interfaces are sufficiently separated that they do not interact.

The supercell self-consistent calculations provide the electronic charge density distribution and the corresponding electrostatic potential. Since the geometry is periodic in the planes parallel to the interface (the (x, y) planes), the first obvious simplification is to consider planar averages as a function of the z coordinate only:

[1] In principle, the single-particle eigenvalues obtained from the LDA(or GGA)-SCF calculations and used to evaluate the bulk band structures and the interface line-ups, are not quasi-particle energies and should be corrected for many-body effects [215, 216, 217] which are much larger, in general, than the numerical uncertainty of the LDA(or GGA)-SCF values. Since these corrections are normally much less important for the valence bands than they are for the conduction bands in semiconductors (typically less than 0.3 eV for the valence-band edge and of the order of 1 eV for the conduction-band edge [215, 217]), it is convenient to calculate the band alignments for the valence part (VBO). We note that these many-body corrections affect the bulk band structure of the crystals and tend to cancel out for the VBO at semiconductor heterojunctions. Moreover, since they do not affect the potential line-up across the interface, which, being a function of the charge density, can be accurately calculated within a DFT-LDA(or GGA) approach, they have no effect on the dependence of the band alignment on interface properties such as orientation, chemical composition and abruptness.

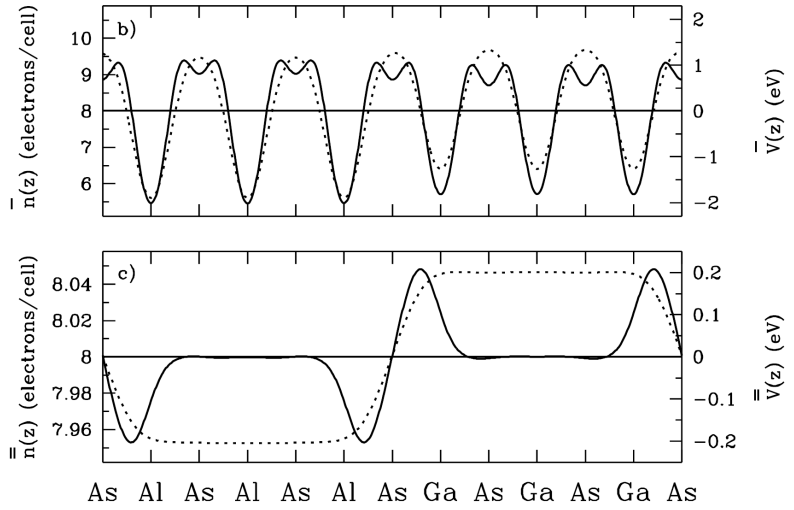

Figure 5.2: Planar averages $\bar{n}(z)$ and $\bar{V}(z)$ (top panel) and macroscopic averages $\bar{\bar{n}}(z)$ and $\bar{\bar{V}}(z)$ (bottom panel) of the electron density and of the electrostatic potential along the growth direction for the GaAs/AlAs(001) interface are shown. Figure taken from Peressi *et al.* [213].

$$\bar{f}(z) = \frac{1}{S}\int_S f(x,y,z)dxdy \tag{5.1}$$

From the three-dimensional electronic charge density it is obtained the one-dimensional charge density $\bar{n}(z)$ and electrostatic potential $\bar{V}(z)$ shown in Figure 5.2 (top panel). This exhibits two distinct, even if very similar, periodic functions in the two bulk materials, which smoothly join across the interface.[2] The effect of the interface is related to the difference between these periodic functions. Such a difference, which is barely visible in Figure 5.2 (top panel), can be enhanced by getting rid of the bulklike oscillations using the macroscopic average technique [218]. The macroscopic average is a basic concept in classical electromagnetism; for any microscopic quantity $f^{(micro)}(\mathbf{r})$ one can define a macroscopic average $f^{(micro)}(\mathbf{r})$:

$$f^{(micro)}(\mathbf{r}) = \int \omega(\mathbf{r}-\mathbf{r}')f^{(micro)}(\mathbf{r}')d\mathbf{r}' \tag{5.2}$$

where $\omega(\mathbf{r})$ is a properly chosen filter function depending on the geometry

[2]Since the system (GaAs/AlAs(001) interface) is a lattice-matched one, the period a of $\bar{n}(z)$ and $\bar{V}(z)$ is the same on both side of the interface and, in this particular case, equal to $a_0/2$ where a_0 is the bulk lattice parameter.

and on the characteristic length scale of the problem. In particular, the application is straightforward for interfaces between two isostructural lattice-matched materials, where ω is a material-independent quantity. In this case acting directly on the planar average, the filter function can be chosen simply as

$$\omega(z) = \frac{1}{a}\Theta\left(\frac{a}{2} - |z|\right) \tag{5.3}$$

where Θ is the one-dimensional step function, giving

$$\bar{\bar{f}}(z) = \frac{1}{a}\int_{z-a/2}^{z+a/2} \bar{f}(z')dz' \tag{5.4}$$

For the GaAs/AlAs(100) interface, charge and potential are shown in Figure 5.2 (bottom panel). From this image we can note that the macroscopically averaged quantities exhibit no microscopic oscillations on either side of the interface and it is recovered the constant macroscopic limit in the two bulks. Conversely, deviations from the macroscopic value indicate the interface region shown and allow one to define the "interface dipole" without referring to arbitrary "ideal" reference configurations. The macroscopic average can also be applied to an interface between two materials A and B with different periodicities because of lattice mismatch or even structural differences, the latter being the case of metal-semiconductor contacts. In order to recover macroscopic features in the bulk regions of both materials, one has to filter twice, using the functions ω_A and ω_B appropriate to each material in turn. This double filtering can be recast in terms of the single filter function

$$\omega(\mathbf{r}) = \int \omega(\mathbf{r} - \mathbf{r}')\omega_B(\mathbf{r}')d\mathbf{r}' \tag{5.5}$$

which explicitly exhibits commutativity. It is noticed that, even if ω_A and ω_B are localized as much as possible, the double filtering reduces the resolution with respect to the single filtering and, for the special case $\omega_A = \omega_B$, the use of ω is not equivalent to the use of ω_A. Different choices of the filter functions will give profiles with different details, but the macroscopic physics, which contains the relevant information, is the same.

The long-range character of the Coulomb interaction makes the average electrostatic potential $\langle V \rangle$ of an infinite system in general ill defined [219]. Therefore, the potential line-up across the interface between two semi-infinite solids cannot be simply calculated as the difference between bulk quantities; rather, it depends in principle on the detailed structure of the interface. For this reason, the problem of band alignment at interfaces is difficult and it is in principle necessary to calculate accurately the interface charge distribution

and the corresponding electrostatic potential. The difference between the macroscopic averages of the electrostatic potential in the two bulk regions is precisely the electrostatic potential line-up ΔV.[3]

Therefore in the macroscopic average techniques, the band offset is conveniently split into two contributions:

$$VBO = \Delta E_v + \Delta V \tag{5.7}$$

ΔE_v is the band structure term and it is the difference between the relevant valence band edges in the two materials, when the single-particle eigenvalues are measured with respect to the average electrostatic potential in the corresponding bulk crystal. The band-structure term is characteristic of the individual bulks. This term can be obtained from standard bulk band-structure calculations for each crystal and displays, by definition, transitivity. This is not the case for the electrostatic potential line-up ΔV, which can, in principle, depend on structural and chemical details of the interface (Figure 5.5 [top panel]). According to the above definition, microscopic quantum effects, such as many-body effects on the quasiparticle spectra [215, 216, 217], are all embedded in the band structure term ΔE_v. We would like to emphasize that the partition of the VBO into a potential line-up and a band term is not unique. ΔV must contain the line-up of the long-range electrostatic potential generated by the electronic and ionic charge distributions. All the quantities related to the short-range local components of the potential (exchange correlation, the difference between the local part of the pseudopotential and an ionic point-charge potential) are bulk quantities and can be arbitrarily included in one of the two terms. In the work reported here, they are included in the band structure term.[4]

[3]The macroscopic average commutes with the spatial differentiation which occurs in the Poisson equation and the potential line-up is thus exactly related to the dipole moment of the charge profile:

$$\Delta V = 4\pi e^2 \int z\bar{\bar{\rho}}(z)dz \tag{5.6}$$

where ρ is the total (ionic plus electronic) charge density which averages to zero in the bulk-like regions. Equation 5.6 allows one to define in an unambiguous way the concept of the interface dipole for any surface or interface.

[4]The total VBO, which is the quantity that is physically meaningful, turns out to be almost pseudopotential independent. Conversely, for a given choice of the definition of the potential line-up and the band term, different pseudopotentials can give remarkably different results for the two terms separately.

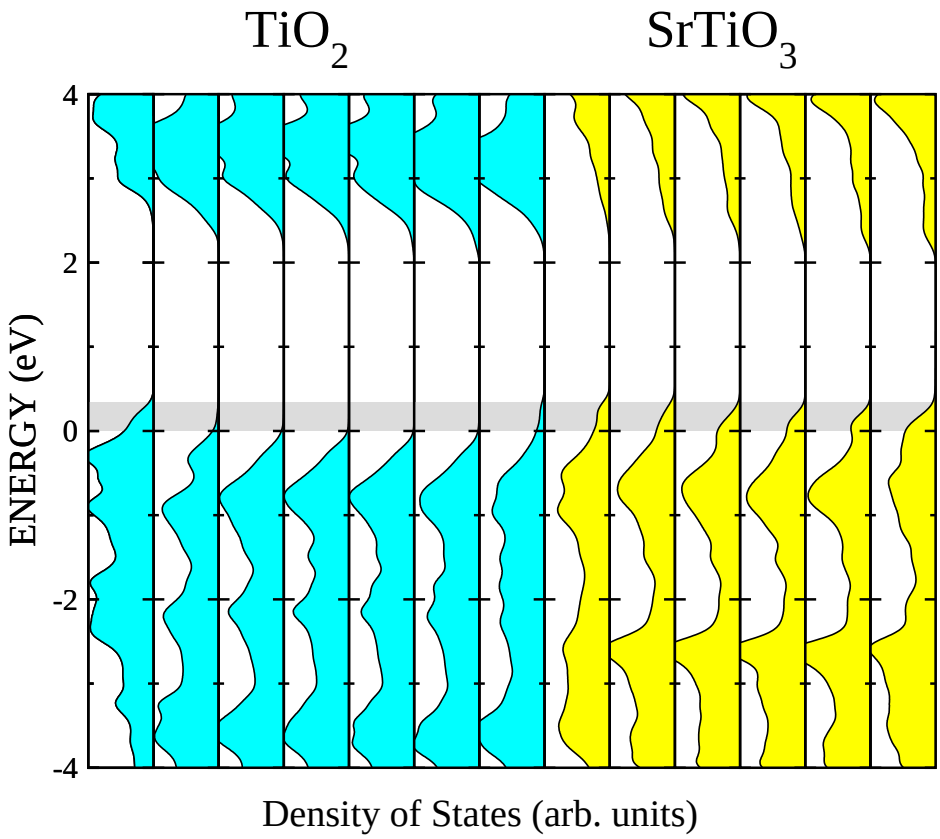

Figure 5.3: Projected density of states of the $SrTiO_3$–TiO_2 interface. The projection is done onto the atomic orbitals belonging to each atomic layer. The energy zero is set to the top anatase bulk valence band. The grey shaded region highlights the valence band offset.

5.1.2 LDOS technique

In supercell calculations, the band offset can also be evaluated directly from the *local density of states* (LDOS) $N(\epsilon, z)$ defined as

$$N(\epsilon, z) = \sum_{\mathbf{k},n} \bar{\bar{\rho}}_{\mathbf{k},n}(z)\delta(\epsilon - \epsilon_{\mathbf{k}}) \tag{5.8}$$

where the sum runs over the bands n and the wavevectors k of the BZ of the supercell, $\rho_{\mathbf{k},n}(\mathbf{r}) = |\psi_{\mathbf{k},n}(\mathbf{r})|^2$ and $\psi_{\mathbf{k},n}(\mathbf{r})$ is the electronic wavefunction. Far from the interface, on each side of the junction, the LDOS $N(\epsilon, z)$ converges to the bulk density of states of the corresponding crystal. The band offset can be obtained thus from the difference between the band edges of

the LDOS on the two sides, far from the junction (Figure 5.3).

The LDOS, however, requires supercell computations with a high number of **k** points and a large energy cut-off compared with those needed to determine the charge density and the potential line-up. In addition, larger supercells have to be used, since the LDOS has a spatial convergence to the bulk features slower than that of the charge density. As a result, the LDOS approach is less convenient, in general, than the potential-line-up approach to determine the band discontinuities.

5.1.3 Band structure technique

There is also another approach at the determination of VBO: the *band structure method* (BSM). In this method, firstly, the band structure of the supercell is determined using ab initio calculations. Then the slab electronic states are projected on the atoms in the bulk regions of the two materials that identify the interface. Therefore two different band structures are obtained for two materials and the band offset can be obtained thus from the difference between the band edges of the two materials (Figure 5.4).

In the BSM, however, it is necessary the use of supercell computations with a high number of k points compared with those needed to determine the charge density and the potential line-up. Moreover, larger supercells have to be used, since the BSM has a spatial convergence to the bulk features slower than that of the charge density. For this reason the BSM is less convenient, in general, than the potential-line-up approach to determine the band discontinuities.

5.1.4 Conduction band offset

The conduction band offset (CBO) is defined as the difference between the conduction band edge energies. Therefore the CBO can be evaluated using the simple relation

$$CBO = VBO + (E_{gap}^{M_1} - E_{gap}^{M_1}) \tag{5.9}$$

where $E_{gap}^{M_1}$ and $E_{gap}^{M_1}$ are the band gaps of the two different materials. Due to the well known inability of DFT methods to describe excited states, the magnitude of the band gap is severely underestimated (for the $SrTiO_3$ and TiO_2 the calculated values for band gaps are 1.83 eV and 2.06 eV, respectively) and cannot be used for a reliable determination of the conduction band edge. The usual way to overcome this problem is to use the experimental values of the band gaps ($E_{\mathrm{gap}}^{\mathrm{SrTiO_3}} = 3.3$ eV and $E_{\mathrm{gap}}^{\mathrm{TiO_2}} = 3.2$ eV are the

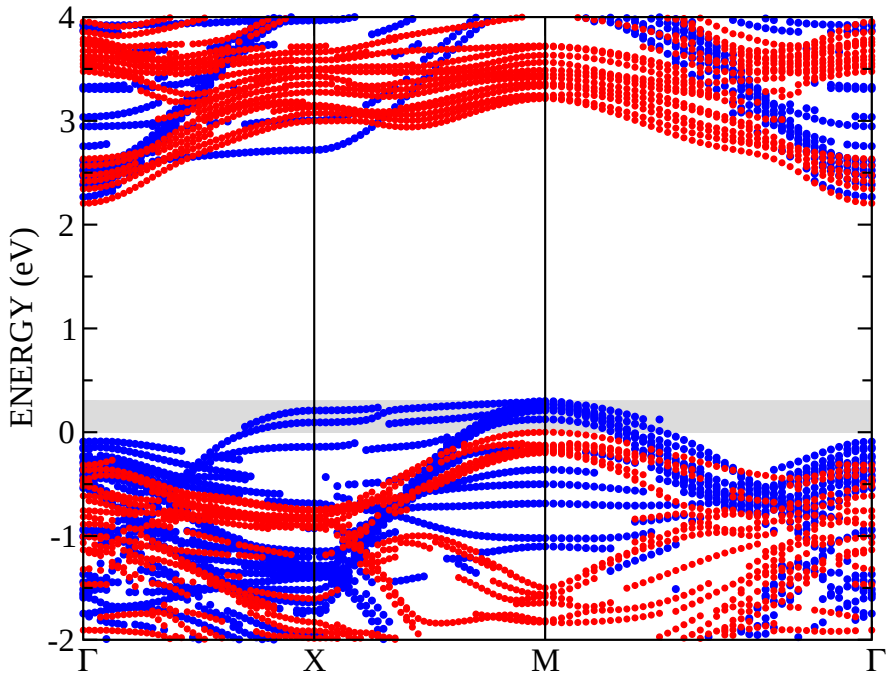

Figure 5.4: Band structure of the $SrTiO_3$–TiO_2 interface. The blue (red) circles identify the slab electronic states with a significant projection (> 0.4) on the atoms in the $SrTiO_3$ (TiO_2) bulk region of supercell. The energy zero is set to the top anatase valence band. The grey shaded region highlights the valence band offset.

experimental band gaps of $SrTiO_3$ and TiO_2, respectively)[5].

5.2 Computation details

All first–principles calculations are carried out within the DFT framework as implemented in the QUANTUM–ESPRESSO package [169]. We adopt the generalized gradient approximation (GGA) parametrized with the Perdew-Wang (PW91) exchange-correlation functional [221]. Vanderbilt ultrasoft pseudopotentials [150] are employed to mimic the ion cores. The kinetic-

[5]Strictly speaking, the experimental band gap actually corresponds to the material optical gap, whereas the relevant quantity for the discussion of band offsets is the quasiparticle gap. Nevertheless, for the TiO_2 anatase, recent first principles calculations employing the GWU method [220] have inferred a 3.27 eV quasiparticle gap, with no significant deviation with respect to the measured optical gap (3.2 eV). The same calculations report a GW redshift of the VBO of TiO_2 anatase of about 0.1 eV, showing that in the case of the VBO calculation only minor corrections to the DFT/PW91 calculations come out.

energy cutoff for the plane waves is set to 40 Ry while the cutoff for the augmented density is set to 320 Ry. The optimized lattice constants ($a = 3.937$ Å for the cubic $SrTiO_3$ bulk crystal and $a = 3.813$ Å, $c = 9.591$ Å for the tetragonal anatase crystal) well compare with previous theoretical reports [222, 21] as well as with the experimental values [126]. The calculated in-plane lattice mismatch between $SrTiO_3(001)$ and anatase $TiO_2(001)$ is -3%. The $SrTiO_3$–TiO_2 interface is modelled, within the supercell method, by a slab consisting of four-to-ten $TiO_2(001)$ layers on the top of thirteen $SrTiO_3$ layers. A 15 Å vacuum separation has been introduced between two consecutive slabs, which proved to be sufficient to avoid spurious interaction between the periodic replica. We set the in-plane lattice parameter to the theoretical equilibrium value calculated for cubic $SrTiO_3$. This reflects the experimental condition that thin layers of TiO_2 anatase are grown on the top of the $SrTiO_3$ substrate. The two-dimensional Brillouin zone (BZ) is sampled using a 8×8×1 Monkhorst-Pack grid including the Γ point. A dipole correction is applied to correct spurious effect caused by the periodic boundary conditions [183]. All the atomic coordinates are fully relaxed until the atomic forces are less than 0.026 eV/Å, except for the atoms in the bottom four layers of $SrTiO_3$, which are kept fixed to their bulk positions.

5.3 Results and Discussion

Figure 5.5 (top panel) shows a schematic representation of the band-structure discontinuities for the $SrTiO_3$–TiO_2 interface with seven layers of TiO_2 anatase using the macroscopic average technique (MA). From the figure, we note that this interface is type II, namely, with both the valence and conduction TiO_2 band edges below the corresponding $SrTiO_3$ counterparts. From our calculations, we obtain a VBO and a CBO of 0.27 and 0.37 eV, respectively.

Table 5.1: VBO and CBO (in eV) at the pure $SrTiO_3$–TiO_2 interface with seven layers of TiO_2 anatase. Theoretical results are obtained by the MA, LDOS and BSM techniques.

	MA	LDOS	BSM
VBO	0.37	0.34	0.30
CBO	0.27	0.24	0.20

The VBO is also evaluated from the local density of state technique (LDOS) and band structure method (BSM) (Figures 5.3 and 5.4, respec-

tively). A summary of the computed band offsets obtained by different approaches is presented in Table 5.1. [6]

Results from different approaches are found to be very similar with a largest difference of about 0.07 eV. In this thesis we have preferred to use the MA approach because, as we said, the LDOS and BSM require more stringent convergence parameters.

The VBO dependence on the number of TiO_2 layers is shown in Figure 5.6(a) (red bullets). The results show that the VBO ranges between +0.27 eV and +0.56 eV but with no systematic dependence on the film thickness. On the other hand, the measured [65] VBO ranges between −0.06 and 0.16 eV as shown by the grey-shaded and dotted region in Figure 5.6(a).

A possible explanation of the discrepancy between the measurements and our theoretical results is that the ideal interface with sharp boundaries is not sufficient to mimic the experimental conditions. It is quite difficult to give a definite and fully satisfactory model of the interface, as the number of possible deviations from the defect free case is enormous and includes intermixtures, impurities, vacancies, interstitials, etc.

Naturally, all these defects do change the interface structure or its chemical composition. As such, they can modify the VBO, as it has been demonstrated for many semiconductor heterostructures [218, 213]. Here, we limit our study to oxygen vacancies because they can be considered as the most abundant type of atomic defects for a large variety of oxides. Moreover, oxygen vacancies are considered responsible for the observed two-dimensional electron gas behaviour exhibited at the $SrTiO_3$–TiO_2 interface grown by laser deposition [64, 61].

For the study of oxygen vacancies near the $SrTiO_3$–TiO_2 interface, we have considered a 2×2 surface supercell (corresponding to a vacancy-vacancy distance of 7.87 Å) composed of eleven alternating atomic layers of SrO and TiO_2 for the $SrTiO_3$ substrate, and seven anatase TiO_2 layers.[7] With reference to Figure 5.5 (top panel), the oxygen vacancy position is varied on

[6] In the LDOS method the valence band edge values in each side of interface is obtained by a single supercell calculation from the LDOS of the central layers of the two materials ($STO-4$ and TiO_2+4 layers). We indicate with the central layer the most distant layer from the interface, and for a sufficiently large supercell, it has the properties of the bulk material.

In the BSM, the $SrTiO_3$ and TiO_2 band structures have been obtained by retaining the only contributions coming from electronic states with a significant projection (>0.4) onto the atomic orbitals associated to $SrTiO_3$ and TiO_2 bulk regions of slab (for $SrTiO_3$ → from STO-2 to STO-5 layers, for TiO_2 → from TiO_2+2 to TiO_2+5 layers). The labelling of the different atomic layers is the same as reported in Figure 5.5 (top panel).

[7] To reduce the computational cost, a 2×2×1 BZ sampling has been employed, since a better sampling does not produce significant variations of the computed band offsets.

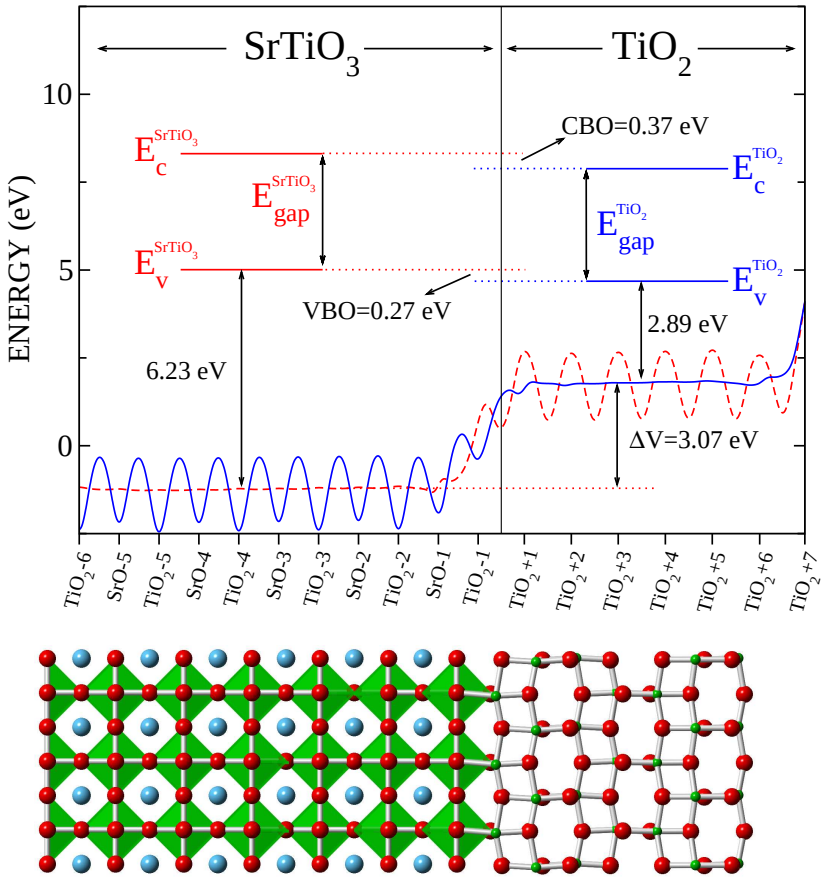

Figure 5.5: Schematic representation (top panel) of the calculated VBO and CBO of an interface modelled with seven layers of TiO_2. E_v, E_c and E_{gap} stand for the top of the valence band, the bottom of the conduction band, and the experimental band gap, respectively. The profile of the macroscopically-averaged self-consistent electrostatic potential is also shown on both sides of the interface. Due to the different *c*-axes, the macroscopic average is taken using either the $SrTiO_3$ (red line) or the TiO_2 (blue line) lattice parameter along the direction normal to the interface. Shown values of E_v are calculated with respect to the average of the electrostatic potential in each material. ΔV stands for the resulting lineup. A schematic view of the $SrTiO_3$–TiO_2 interface is shown in the bottom panel. The O, Sr and Ti atoms are marked by large red, large blue and small green spheres, respectively. Figure taken from D'Amico *et al.* [223].

either side of the interface, ranging from the TiO_2-2 to the TiO_2-1 atomic layer in the $SrTiO_3$, and from the TiO_2+1 to the TiO_2+3 atomic layer in the TiO_2 anatase. The oxygen vacancy formation energy as a function of

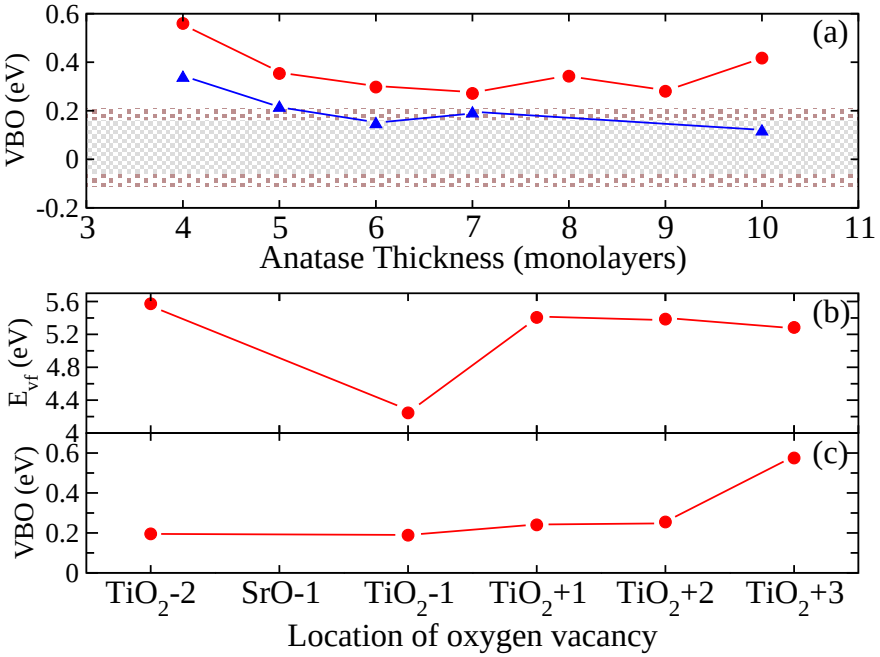

Figure 5.6: (a) VBO as a function of number of anatase TiO_2 layers. Red bullets and blue triangles are referred to the pure and the defected (oxygen vacancy in the TiO_2-1 layer) interface, respectively. The lines are guides for eyes. The grey-shaded and dotted regions highlight the maximum range of VBO values spanned by the experimental data and their uncertainties, respectively (see Ref. [65]). (b) Oxygen vacancy formation energy E_{vf} and (c) VBO as a function of the position of the oxygen vacancy. As the oxygen vacancy moves away from the interface, the formation energy approaches the bulk limits (5.11 and 4.76 eV for $SrTiO_3$ and TiO_2, respectively). The result for the vacancy in the SrO-1 layer is missing because this configuration is unstable (starting with an oxygen vacancy in the SrO-1 layer, the vacancy "diffuses" into the TiO-1 layer). The labelling of the different atomic layers is the same as that reported in Figure 5.5 (top panel). Figure taken from D'Amico *et al.* [223].

its position can be computed, in the oxygen-rich limit, by using the formula $E_{vf} = E^{\rm vac}_{\rm slab} + \frac{1}{2}E_{\rm O_2} - E_{\rm slab}$, where $E^{\rm vac}_{\rm slab}$, $E_{\rm slab}$ and $E_{\rm O_2}$ are the calculated DFT total energies of the slab containing the defect, of the spin polarized O_2 molecule and of the stoichiometric slab, respectively. The most stable configuration is found [see Fig. 5.6(b)] with the oxygen vacancy in the TiO_2-1 layer ($E_{vf} = 4.24$ eV). It is noteworthy to observe [Fig. 5.6(c)] that, in the presence of an oxygen vacancy, VBO variations as large as 0.4 eV might be

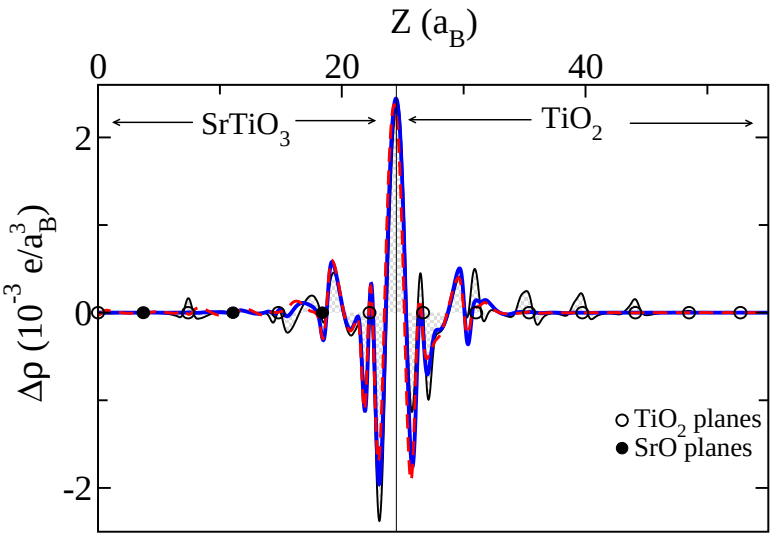

Figure 5.7: Planar average of the induced charge density at the $SrTiO_3$–TiO_2 interface. The solid blue line corresponds to the pure interface, the dashed red and the black shaded lines refer to the interface with an oxygen vacancy placed in the TiO_2+1 and TiO_2-1 layers, respectively. Figure taken from D'Amico *et al.* [223].

observed.

Focusing on the most stable configuration, we report in Figure 5.6(a) the VBO as a function of number of TiO_2 layers (blue triangles). Even in this case, no systematic dependence on the film thickness can be observed, but an evident decrease of the VBO with respect to the pure interface comes out. The range of variation is between +0.11 and +0.34 eV, which much better matches the experimental outcome (see grey-shaded and dotted regions in the same figure).

The analysis of the charge transfer (CT) following the formation of the interface (Fig. 5.7) reveals a substantial similarity between the pure interface and the one with the vacancy at the anatase TiO_2 side (solid blue and dashed red lines, respectively). In this case, the charge provided by the vacancy does not give a new contribution to the CT, resulting in the partial occupation of the Ti_{3d} states in the anatase region. On the other hand, the presence of a vacancy in the $SrTiO_3$ side involves an additional redistribution of the charge in the near-interface region [see the black shaded in Fig. 5.7]. In particular, the charge provided by the vacancy determines the occupation of the d_{xy} orbitals of the Ti atoms in the anatase side, providing also an

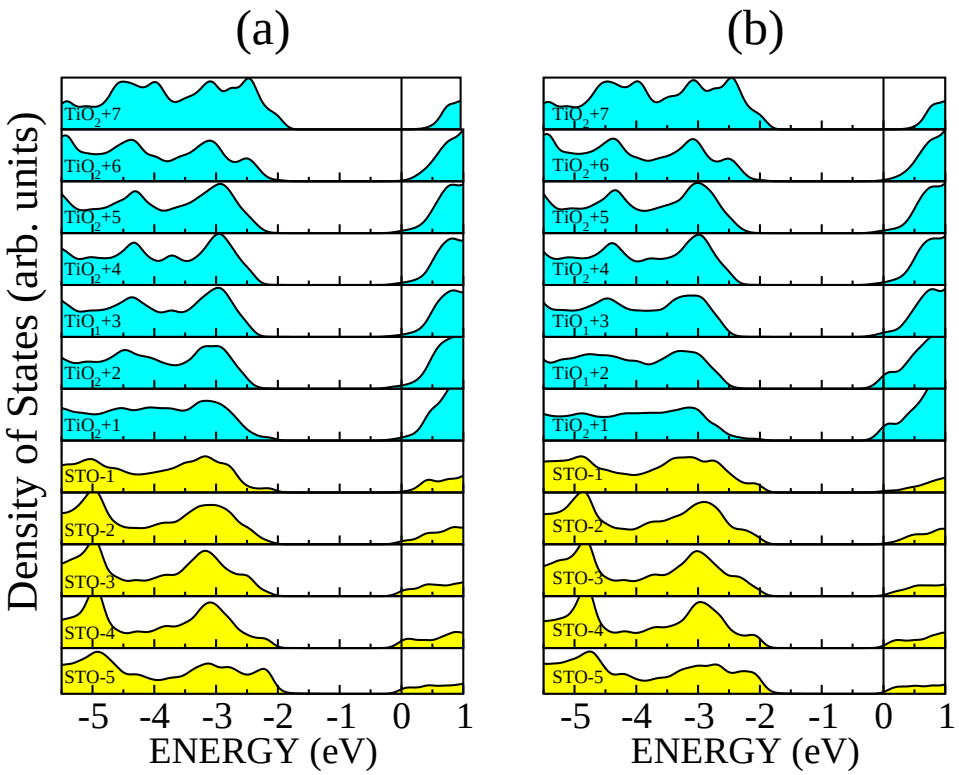

Figure 5.8: Projected density of states of the defected interface with one oxygen vacancy in (a) the TiO_2-1 and (b) the TiO_2+1 layer. The projection is done onto the atomic orbitals belonging to each atomic layer. The Fermi level is set to zero energy. Figure taken from D'Amico *et al.* [223].

evidence of a possible cooperating effect in the formation of a two-dimensional electron gas observed for this kind of interface [64, 61]. Therefore, it is evident that the presence of the defect at the $SrTiO_3$ side induces a modification in the chemical and electronic properties of the interface, that in turn have effect on the net dipole moment caused by the formation of the interface. This explains the differences of the band offsets as a function of the vacancy position (compare bullets and triangles in Fig. 5.6).

From the electronic point of view, regardless of the position of the vacancy, the partial occupation of Ti_{3d} orbitals gives rise to a metallic interface, as it is evident from the projected density of states analysis of Figure 5.8. Nevertheless, such as result should be taken with care, because the well known failures of DFT in properly treating the strong Coulomb interaction between 3d electrons might lead to an inadequate description of 3d states of Ti^{3+} in

the oxygen-deficient TiO_2 system [224, 225, 226].

5.4 Conclusions

We have reported on first principles calculations of the properties of the epitaxial $SrTiO_3$–TiO_2 (anatase) heterojunction with an emphasis on the electronic band profile and lineup at the interface. The valence and conduction band offsets have been calculated as a function of the number of anatase layers deposited onto the $SrTiO_3$. It has been shown that there is a discrepancy between the measurements and our theoretical results and a possible explanation of this discrepancy is that the ideal interface with sharp boundaries is not sufficient to mimic experimental conditions. Therefore we have investigated the effects of oxygen vacancies on the electronic band profile and lineup at the $SrTiO_3$–TiO_2 interface. We have limited out study to the oxygen vacancies because they are considered as the most abundant type of atomic defects for a large variety of oxides. The main properties that we highlighted are summarized in the following:

- For the pure interface, the VBO ranges between +0.27 eV and +0.56 eV but there is no systematic dependence on the film thickness. These values are significantly higher than the experimental values.

- For the defected interface, the most stable configuration is found with the oxygen vacancy in the TiO_2-1 layer. Moreover, as the oxygen vacancy moves away from the interface, the formation energy approaches the bulk limits (5.11 and 4.76 eV for $SrTiO_3$ and TiO_2, respectively).

- Focusing on the most stable configuration, an evident decrease of the VBO with respect to the pure interface comes out, (the range variation is between +0.11 and +0.34 eV), which much better matches the experimental outcome, suggesting that the perceived absence of a valence band offset is not intrinsic.

Conclusions

In this thesis we have performed DFT calculations for two different classes of oxide materials. The first class of system which have been considered concerns the ZnO $(10\bar{1}0)$ and $(11\bar{2}0)$ non polar surfaces. The second one is represented by $SrTiO_3$–TiO_2 interface.

By using ab initio computational methods, we have investigated the formation and the diffusion of oxygen vacancies at the ZnO $(10\bar{1}0)$ and $(11\bar{2}0)$ surfaces. As expected, the formation energy tends to increase, when the vacancy moves from the surface to subsurface layer, approaching the bulk limit for sufficiently deep vacancy sites.

The study of the defected slab formation energy as a function of the oxygen chemical potential (that, in turn, depends on the external environment conditions) shows the possibility of obtaining, under strongly reducing conditions, reduced surfaces by varying the oxygen gas temperature and/or pressure. This is confirmed by a number of experiments, which were able also to measure the effects on the electronic and transport properties of the defects. Yet, at variance with other materials, such as TiO_2, obtaining stable defected surfaces is only achievable under well defined experimental conditions, which explains why more recent STM studies do exclude the presence of oxygen vacancies at the surface. By comparing the energetics of three kind of defects (O, Zn and ZnO vacancies), we can also conclude that, differently from the O vacancy, there are no pressure and temperature conditions under which the Zn and ZnO vacancy defects get more stable than the stoichiometric surface.

The defect formation affects the surface electronic structure, in that an intra-gap occupied state shows up, with a "localized" character around the oxygen vacancy. The energy of the intra-gap state depends on the oxygen vacancy depth inside the material. Moreover, other fundamental properties, such as the surface gap energy and electron affinity, can be significantly altered by the presence of the defect and strongly depend on its position with respect to the surface.

Finally, we have also performed a detailed first principles study of the

diffusion behavior of oxygen vacancies both in the bulk ZnO crystal and in the ZnO $(10\bar{1}0)$ and $(11\bar{2}0)$ surfaces. We have found that the oxygen vacancies diffuse much more easily in the surface layer than in the bulk. In particular, we have verified that surface diffusion can be activated at relatively modest temperature (490 K and 481 K for the $(10\bar{1}0)$ and $(11\bar{2}0)$ surfaces, respectively). Moreover, migration paths in the direction orthogonal to the surface show asymmetric barriers, which are smaller (by 0.5–0.9 eV) in the direction toward the surface, thus showing that it is favored the diffusion from subsurface layers to the surface. Of course, it is expected that surface defects will remain stable only in absence of O_2, since the surface vacancy sites are expected to be very reactive even at low temperatures [51].

The second class of materials that we have studied in this thesis is the $SrTiO_3$–TiO_2 interface. We have given a detailed description of the electronic properties of the pure and defected $SrTiO_3$–TiO_2 interface. In particular, we have focused on the determination of the VBO and CBO. Our results indicate that, for the pure interface, the VBO ranges between +0.27 eV to +0.56 eV with no systematic dependence on the film thickness. These calculated band offsets are significantly higher than the near zero experimental values [65]. Therefore, to explain this discrepancy, we have studied the $SrTiO_3$–TiO_2 interface in presence of oxygen vacancies on either side of the interface. Our results indicate that the most stable configuration is found with the oxygen vacancy in the TiO_2-1 layer of $SrTiO_3$.

Focusing on the most stable configuration, even in this case, no systematic dependence on the the film thickness can be observed for the VBO. In particular the range of variation of VBO is between +0.11 eV and +0.34 eV. These results clearly indicate that the oxygen vacancies are responsible of an evident decrease of the VBO with respect to the pure interface. Therefore, focusing on the VBO, we have identified the presence of oxygen vacancies as a possible tool to lower barrier heights, in agreement with the near zero band offsets which have been experimentally observed. Moreover, our results show that profound modifications of the electronic structure of the interface can be induced by the presence of such vacancies, giving indication of a possible tool to tailor the interface properties.

These results are relevant for fundamental photochemistry studies involving this heterojunction, in that neither photogenerated electron nor holes are expected to become trapped in the substrate. Rather, both kind of charged particles can freely diffuse to the surface and drive heterogeneous photochemical reactions.

Our investigation on both defected ZnO non-polar surfaces and $SrTiO_3$–TiO_2 interface, performed by means of DFT calculations, indicates that electronic properties of such oxide materials can be significantly modulated

through the oxygen vacancies. Therefore the results of this thesis show the important role of oxygen vacancies in these metal oxide nanostructures.

Bibliography

[1] S. Pelet, M. Gratzel, and J.-E. Moser. *J. Phys. Chem. B*, 107:3215–3224, 2003.

[2] X. Qiu, Y. Zhao, and C. Burda. *Adv. Mater.*, 19:3995–3999, 2007.

[3] K. Tvrdy, P. .A. Frantsuzov, and P. V. Kamat. *Proceedings of the National Academy of Sciences*, 108:29–34, 2011.

[4] P. V. Kamat. *J. Phys. Chem. B Lett.*, 2:839–840, 2011.

[5] J. Z. Zhang. *MRS Bulletin*, 36:48–55, 2011.

[6] N. Yamazoe. *Sens. Act. B*, 5:7–19, 1991.

[7] G. Sberveglieri. *Sens. Act. B*, 23:103–109, 1995.

[8] A. M. Azad, S. A. Akbar, S. G. Mhaisalkar, L. D. Birkefeld, and K. S. Goto. *J. Electrochem. Soc.*, 139:3690–3704, 1992.

[9] K. J. Choi and H. W. Jang. *Sensors*, 10:4083–4099, 2010.

[10] G. Korotcenkov. *Mater. Sci. Eng. B*, 139:1–23, 2007.

[11] N. Barsan, D. Koziej, and U. Weimar. *Sens. Act. B*, 121:18–35, 2007.

[12] R. Moos, K. Sahner, M. Fleischer, U. Guth, N. Barsan, and U. Weimar. *Sensors*, 9:4323–4365, 2009.

[13] C. Wang, L. Yin, L. Zhang, D. Xiang, and R. Gao. *Sensors*, 10:2088–2106, 2010.

[14] M. Batzill. *Sensors*, 6:1345–1366, 2006.

[15] M. Batzill, K. Katsiev, J. M. Burst, U. Diebold, A. M. Chaka, and B. Delley. *Phys. Rev. B*, 72:165414, 2005.

[16] M. Batzill and U. Diebold. *Prog. Surf. Sci.*, 79:47–154, 2005.

[17] N. Koshizaki and T. Oyama. *Sens. Act. B*, 66:119–121, 2000.

[18] F. Trani, M. Causà, D. Ninno, G. Cantele, and V. Barone. *Phys. Rev. B*, 77:245410, 2008.

[19] X. Chen and S. S. Mao. *Chem. Rev.*, 107:2891–2959, 2007.

[20] A. Iacomino, G. Cantele, D. Ninno, I. Marri, and S. Ossicini. *Phys. Rev. B*, 78:075405, 2008.

[21] A. Iacomino, G. Cantele, F. Trani, and D. Ninno. *J. Phys. Chem. C*, 114:12389–12400, 2010.

[22] K. Hameeuw, G. Cantele, D. Ninno, F. Trani, and G. Iadonisi. *Phys. Status Solidi A*, 203:2219–2222, 2006.

[23] R. N. Viswanath, S. Ramasamy, R. Ramamoorthy, P. Jayavel, and T. Nagarajan. *Nanostr. Mater.*, 6:993–996, 1995.

[24] M. S. Wu, A. Azuma, T. Shiosaki, and A. Kawabata. *IEEE Trans. Ultrasonics Ferroelec. Freq. Control*, 36:442–445, 1989.

[25] M. K. Jayaraj, A. Antony, and M. Ramachandran. *Bull. Mater. Sci.*, 25:227–230, 2002.

[26] K. Keis, C. Bauer, G. Boschloo, A. Hagfeldt, K. Westermark, H. Rensmo, and H. Siegbahn. *J. Photochem. Photobiol. A*, 148:57–64, 2002.

[27] P. Yang, H. Yan, S. Mao, R. Russo, J. Johnson, R. Saykally, N. Morris, J. Pham, R. He, and H.-J. Choi. *Adv. Funct. Mater.*, 12:323–331, 2002.

[28] Y. Hu, L. Lin, Y. Zhang, and Z. L. Wang. *Adv. Mater.*, 24:110–114, 2012.

[29] Y. Hu, Y. Zhang, C. Xu, L. Lin, R. L. Snyder, and Z. L. Wang. *Nano Lett.*, 11:2572–2577, 2011.

[30] S. Roy and S. Basu. *Bull. Mater. Sci.*, 25:513–515, 2002.

[31] A. R. Raju and C. N. R. Rao. *Sens. Act. B*, 3:305–310, 1991.

[32] F. Patolsky, B. P. Timko, G. Zheng, and C. M. Lieber. *MRS Bull.*, 32:142–149, 2007.

[33] Z. W. Pan, Z. R. Dai, and Z. L. Wang. *Science*, 291:1947–1949, 2001.

[34] M. D. McCluskey and S. J. Jokela. *J. Appl. Phys.*, 106:071101, 2009.

[35] S. Dutta, S. Chattopadhyay, A. Sarkar, M. Chakrabarti, D. Sanyal, and D. Jana. *Progr. Mater. Sci.*, 54:89–136, 2009.

[36] T. K. Gupta and W. G. Carlson. *J. Mater. Sci.*, 20:3487–3500, 1985.

[37] M. S. Ramanachalam, A. Rohatgi, J. P. Schaffer, and T. K. Gupta. *J. Appl. Phys.*, 69:8380–8386, 1991.

[38] L. J. Brillson and Y. Lu. *J. Appl. Phys.*, 109:121301, 2011. and references therein.

[39] A. F. Kohan, G. Ceder, D. Morgan, and C. G. Van de Walle. *Phys. Rev. B*, 61:15019–15027, 2000.

[40] S. B. Zhang, S.-H. Wei, and A. Zunger. *Phys. Rev. B*, 63:075205, 2001.

[41] F. Oba, S. R. Nishitani, S. Isotani, H. Adachi, and I. Tanaka. *J. Appl. Phys.*, 90:824–828, 2001.

[42] P. Erhart, A. Klein, and K. Albe. *Phys. Rev. B*, 72:085213, 2005.

[43] Y. Yan, S. B. Zhang, and S. T. Pantelides. *Phys. Rev. Lett.*, 86:5723–5726, 2001.

[44] S. Limpijumnong, S. B. Zhang, S.-H. Wei, and C. H. Park. *Phys. Rev. Lett.*, 92:155504, 2004.

[45] G. Pacchioni. *Chem. Phys. Chem*, 4:1041–1047, 2003.

[46] P. Erhart and K. Albe. *Phys. Rev. B*, 73:115207, 2006.

[47] A. Janotti and C. G. Van de Walle. *Phys. Rev. B*, 76:165202, 2007.

[48] G.-Y. Huang, C.-Y. Wang, and J.-T. Wang. *J. Phys.: Cond. Matt.*, 21:345802, 2009.

[49] R. Kováčik, B. Meyer, and D. Marx. *Angew. Chem. Intern. Ed.*, 46:4894–4897, 2007.

[50] Q. Wang, Q. Sun, G. Chen, Y. Kawazoe, and P. Jena. *Phys. Rev. B*, 77:205411, 2008.

[51] W. Göpel and U. Lampe. *Phys. Rev. B*, 22:6447–6462, 1980.

[52] W. Göpel, L. J. Brillson, and C. F. Brucker. *J. Vac. Sci. Tech.*, 17:894–898, 1980.

[53] U. Diebold, L. V. Koplitz, and O. Dulub. *Appl. Surf. Sci.*, 237:336–342, 2004.

[54] X. Shao, K.-I. Fukui, H. Kondoh, M. Shionoya, and Y. Iwasawa. *J. Phys. Chem. C*, 113:14356–14362, 2009.

[55] F. Trani, M. Causà, S. Lettieri, A. Setaro, D. Ninno, V. Barone, and P. Maddalena. *Microelectron. J.*, 40:236–238, 2009.

[56] J. Mannhart and D. G. Schlom. *Science*, 327:1607–1611, 2010.

[57] P. Zubko, S. Gariglio, M. Gabay, P. Ghosez, and J.-M. Triscone. *Annu. Rev. Condens. Matter Phys.*, 2:141–165, 2011.

[58] H. Y. Hwang, Y. Iwasa, M. Kawasaki, B. Keimer, N. Nagaosa, and Y. Tokura. *Nat. Mater.*, 11:103–113, 2012.

[59] A. Lotnyk, S. Senz, and D. Hesse. *Thin Solid Films*, 515:3439–3447, 2007.

[60] Z. Wang, R. Sun, C. Chen, M. Saito, S. Tsukimoto, and Y. Ikuhara. *J. Mater. Sci.*, 47:5148–5147, 2012.

[61] H. L. Kwok. *J. Phys. D: Appl. Phys*, 43:415303, 2010.

[62] M. Radovic, M. Salluzzo, Z. Ristic, R. Di Capua, N. Lampis, R. Vaglio, and F. Miletto Granozio. *J. Chem. Phys.*, 135:034705, 2011.

[63] R. Ciancio, E. Carlino, C. Aruta, D. Maccariello, F. Miletto Granozio, and U. Scotti di Uccio. *Nanoscale*, 4:91–94, 2012.

[64] H. Ohta, S. Kim, Y. Mune, T. Mizoguchi, K. Nomura, S. Ohta, T. Nomura, Y. Nakanishi, Y. Ikuhara, M. Hirano, H. Hosono, and K. Koumoto. *Nat. Mater.*, 6:129–134, 2007.

[65] S. A. Chambers, T. Ohsawa, C. M. Wang, I. Lyubinetsky, and J. E. Jaffe. *Surf. Sci.*, 603:771–780, 2009.

[66] Y. Tokura and H. Y. Hwang. *Nat. Mater.*, 7:694, 2008.

[67] J. Heber. *Nature*, 459:28, 2009.

[68] P. N. Keating. *Phys. Rev.*, 145:637–645, 1966.

[69] I. K. Robinson, W. K. Waskiewicz, P. H. Fuoss, and L. J. Norton. *Phys. Rev. B*, 37:4325–4328, 1988.

[70] L. D. Marks, E. Bengu, C. Collazo-Davila, D. Grozea, E. Landree, C. Leslie, and W. Sinkler. *Surf. Rev. Lett.*, 05:1087–1106, 1998.

[71] J. H. Sinfelt. *Ind. Eng. Chem. Fundam.*, 25:2–9, 1986.

[72] V. E. Henrich and P. A. Cox. *The Surface Science of Metal Oxides*. Cambridge: Cambridge University Press, 1994.

[73] P. W. Tasker. *J Phys. C: Sol. St. Phys.*, 12:4977, 1979.

[74] D. Wolf. *Phys. Rev. Lett.*, 68:3315–3318, 1992.

[75] A. Subramanian, L. D. Marks, O. Warschkow, and D. E. Ellis. *Phys. Rev. Lett.*, 92:026101, 2004.

[76] A. N. Chiaramonti, C. H. Lanier, L. D. Marks, and P. C. Stair. *Surf. Sci.*, 602:3018–3025, 2008.

[77] O. Warschkow, M. Asta, N. Erdman, K. R. Poeppelmeier, D. E. Ellis, and L. D. Marks. *Surf. Sci.*, 573:446–456, 2004.

[78] C. B. Duke. *Chem. Rev.*, 96:1237–1260, 1996.

[79] A. Tsukazaki, S. Akasaka, K. Nakahara, Y. Ohno, D. Maryenko, A. Ohtomo, and M. Kawasaki. *Nat. Mater.*, 9:889–893, 2010.

[80] A. Ohtomo and H. Y. Hwang. *Nature*, 427:423–426, 2004.

[81] N. Ogawa, T. Satoh, Y. Ogimoto, and K. Miyano. *Phys. Rev. B*, 78:212409, 2008.

[82] M. Izumi, Y. Ogimoto, Y. Konishi, T. Manako, M. Kawasaki, and Y. Tokura. *Mater. Sci. Eng. B*, 84:53–57, 2001.

[83] M. Chiesa, M. C. Paganini, E. Giamello, and D. M. Murphy. *Langmuir*, 13:5306–5315, 1997.

[84] R. Schaub, E. Wahlström, A. Ronnau, E. Laegsgaard, I. Stensgaard, and F. Besenbacher. *Science*, 299:377–379, 2003.

[85] H.-J. Freund. *Surf. Sci.*, 500:271–299, 2002.

[86] S. Abbet, A. Sanchez, U. Heiz, and W.-D. Schneider. *J. Catal.*, 198:122–127, 2001.

[87] A. Bogicevic and D. R. Jennison. *Surf. Sci.*, 515:L481–L486, 2002.

[88] C. T. Campbell and D. E. Starr. *J. Am. Chem. Soc.*, 124:9212–9218, 2002.

[89] S. Abbet, A. Sanchez, U. Heiz, W.-D. Schneider, A. M. Ferrari, G. Pacchioni, and N. Rösch. *J. Am. Chem. Soc.*, 122:3453–3457, 2000.

[90] F. Decremps, F. Datchi, A. M. Saitta, A. Polian, S. Pascarelli, A. Di Cicco, J. P. Itié, and F. Baudelet. *Phys. Rev. B*, 68:104101, 2003.

[91] U. Ozgur, Y. I. Alivov, C. Liu, A. Teke, M. A. Reshchikov, S. Dogan, V. Avrutin, S.-J. Cho, and H. Morkoc. *J. Appl. Phys.*, 98:041301, 2005.

[92] D. C. Look, D. C. Reynolds, J. R. Sizelove, R. L. Jones, C. W. Litton, G. Cantwell, and W. C. Harsch. *Sol. St. Comm.*, 105:399–401, 1998.

[93] K. Maeda, M. Sato, I. Niikura, and T. Fukuda. *Semicond. Sci. Technol.*, 20:S49, 2005.

[94] D. C. Look, D. C. Reynolds, C. W. Litton, R. L. Jones, D. B. Eason, and G. Cantwell. *Appl. Phys. Lett.*, 81:1830–1832, 2002.

[95] A. Ohtomo and A. Tsukazaki. *Semicond. Sci. Technol.*, 20:S1, 2005.

[96] S. Heinze, A. Krtschil, J. Blsing, T. Hempel, P. Veit, A. Dadgar, J. Christen, and A. Krost. *J. Cryst. Growth*, 308:170–175, 2007.

[97] A. Mang, K. Reimann, and St. Rbenacke. *Sol. St. Comm.*, 94:251–254, 1995.

[98] D. C. Look. *Mater. Sci. Eng. B*, 80:383–387, 2001.

[99] D. C. Reynolds, D. C. Look, and B. Jogai. *Sol. St. Comm.*, 99:873–875, 1996.

[100] D. M. Bagnall, Y. F. Chen, Z. Zhu, T. Yao, S. Koyama, M. Y. Shen, and T. Goto. *Appl. Phys. Lett.*, 70:2230–2232, 1997.

[101] H. Cao, Y. G. Zhao, S. T. Ho, E. W. Seelig, Q. H. Wang, and R. P. H. Chang. *Phys. Rev. Lett.*, 82:2278–2281, 1999.

[102] M. H. Huang, S. Mao, H. Feick, H. Yan, Y. Wu, H. Kind, E. Weber, R. Russo, and P. Yang. *Science*, 292:1897–1899, 2001.

[103] Y. R. Ryu, W. J. Kim, and H. W. White. *J. Cryst. Growth*, 219:419–422, 2000.

[104] J. Molarius, J. Kaitila, T. Pensala, and M. Ylilammi. *J. Mater. Sci. - Mater. Electron.*, 14:431–435, 2003.

[105] M. N. Kamalasanan and S. Chandra. *Thin Solid Films*, 288:112–115, 1996.

[106] O. Schmidt, P. Kiesel, C. G. Van de Walle, N. M. Johnson, J. Nause, and G. H. Döhler. *Jpn. J. Appl. Phys.*, 44:7271–7274, 2005.

[107] O. Schmidt, A. Geis, P. Kiesel, C. G. Van de Walle, N. M. Johnson, A. Bakin, and A. Waag. *Superlattices Microstruct.*, 39:8–16, 2006.

[108] M. C. Larciprete, D. Haertle, A. Belardini, M. Bertolotti, F. Sarto, and P. Günter. *Appl. Phys. B*, 82:431–437, 2006.

[109] D. I. Florescu, L. G. Mourokh, Fred H. Pollak, D. C. Look, G. Cantwell, and X. Li. *J. Appl. Phys.*, 91:890–892, 2002.

[110] F. Tuomisto, K. Saarinen, D. C. Look, and G. C. Farlow. *Phys. Rev. B*, 72:085206, 2005.

[111] C. B. Duke, R. J. Meyer, A. Paton, and P. Mark. *Phys. Rev. B*, 18:4225–4240, 1978.

[112] C. B. Duke, A. R. Lubinsky, S. C. Chang, B. W. Lee, and P. Mark. *Phys. Rev. B*, 15:4865–4873, 1977.

[113] H. van Hove and R. Leysen. *Phys. Status Solidi A*, 9:361–367, 1972.

[114] Y. Wang, B. Meyer, X. Yin, M. Kunat, D. Langenberg, F. Traeger, A. Birkner, and C. Wöll. *Phys. Rev. Lett.*, 95:266104, 2005.

[115] B. Meyer, D. Marx, O. Dulub, U. Diebold, M. Kunat, D. Langenberg, and C. Wöll. *Angew. Chem. Int. Ed.*, 43:6641–6645, 2004.

[116] Y. Yan and M. M. Al-Jassim. *Phys. Rev. B*, 72:235406, 2005.

[117] O. Dulub, L. A. Boatner, and U. Diebold. *Surf. Sci.*, 519:201–217, 2002.

[118] X.-L. Yin, A. Birkner, K. Hanel, T. Lober, U. Kohler, and C. Woll. *Phys. Chem. Chem. Phys.*, 8:1477–1481, 2006.

[119] B. Meyer and D. Marx. *Phys. Rev. B*, 67:035403, 2003. and references therein.

[120] A. S. Bhalla, R. Guo, and R. Roy. *Material Research Innovations*, 4:3–26, 2000.

[121] L. V. Goncharova, D. G. Starodub, E. Garfunkel, T. Gustafsson, V. Vaithyanathan, J. Lettieri, and D. G. Schlom. *J. Appl. Phys.*, 100:014912, 2006.

[122] K. I. Hadjiivanov and D. G. Klissurski. *Chem. Soc. Rev.*, 25:61–69, 1996.

[123] A. L. Linsebigler, G. Lu, and J. T. Yates. *Chem. Rev.*, 95:735–758, 1995.

[124] H.-J. Freund. *Faraday Discuss.*, 114:1–31, 1999.

[125] X. Weng, P. Fisher, M. Skowronski, P.A. Salvador, and O. Maksimov. *J. Cryst. Growth*, 310:545–550, 2008.

[126] C. C. Hsieh, K. H. Wu, J. Y. Juang, T. M. Uen, J.-Y. Lin, and Y. S. Gou. *J. Appl. Phys.*, 92:2518–2523, 2002.

[127] M. Kawasaki, K. Takahashi, T. Maeda, R. Tsuchiya, M. Shinohara, O. Ishiyama, T. Yonezawa, M. Yoshimoto, and H. Koinuma. *Science*, 266:1540–1542, 1994.

[128] S. A. Chambers, Y. Liang, Z. Yu, R. Droopad, J. Ramdani, and K. Eisenbeiser. *Appl. Phys. Lett.*, 77:1662–1664, 2000.

[129] S. A. Chambers, Y. Liang, and Y. Gao. *Phys. Rev. B*, 61:13223–13229, 2000.

[130] S. A. Chambers, Y. Liang, Z. Yu, R. Droopad, and J. Ramdani. *J. Vac. Sci. Technol., A*, 19:934–939, 2001.

[131] S. A. Chambers, J. R. Williams, M. A. Henderson, A. G. Joly, M. Varela, and S. J. Pennycook. *Surf. Sci.*, 587:L197–L207, 2005.

[132] J. M. Carlsson, B. Hellsing, H. S. Domingos, and P. D. Bristowe. *J. Phys.: Cond. Mat.*, 13:9937, 2001.

[133] F. Oba, H. Adachi, and I. Tanaka. *J. Mater. Res.*, 15:2167–2175, 2000.

[134] N. W. Ashcroft and N. D. Mermin. *Solid State Physics*. Science: Physics. Saunders College, 1976.

[135] W. A. Harrison. *Surf. Sci.*, 299–300:298–310, 1994.

[136] P. Hohenberg and W. Kohn. *Phys. Rev.*, 136:B864–B871, 1964.

[137] W. Kohn and L. J. Sham. *Phys. Rev.*, 140:A1133–A1138, 1965.

[138] D. M. Ceperley and B. J. Alder. *Phys. Rev. Lett.*, 45:566–569, 1980.

[139] J. P. Perdew and Alex Zunger. *Phys. Rev. B*, 23:5048–5079, 1981.

[140] D. C. Langreth and M. J. Mehl. *Phys. Rev. Lett.*, 47:446–450, 1981.

[141] J. P. Perdew. *Phys. Rev. B*, 33:8822–8824, 1986.

[142] A. D. Becke. *Phys. Rev. A*, 38:3098–3100, 1988.

[143] J. P. Perdew, J. A. Chevary, S. H. Vosko, Koblar A. Jackson, M. R. Pederson, D. J. Singh, and C. Fiolhais. *Phys. Rev. B*, 46:6671–6687, 1992.

[144] John P. Perdew, Kieron Burke, and Matthias Ernzerhof. *Phys. Rev. Lett.*, 77:3865–3868, 1996.

[145] J. P. Perdew, S. Kurth, A. Zupan, and P. Blaha. *Phys. Rev. Lett.*, 82:2544–2547, 1999.

[146] W. A. Harrison. *Electronic structure and the properties of solids: the physics of the chemical bond*. Dover Books on Physics. Dover Publications, 1989.

[147] D. R. Hamann, M. Schlüter, and C. Chiang. *Phys. Rev. Lett.*, 43:1494–1497, 1979.

[148] L. Kleinman and D. M. Bylander. *Phys. Rev. Lett.*, 48:1425–1428, 1982.

[149] N. Troullier and J. Martins. *Sol. St. Comm.*, 74:613–616, 1990.

[150] D. Vanderbilt. *Phys. Rev. B*, 41:7892–7895, 1990.

[151] K. Laasonen, A. Pasquarello, R. Car, C. Lee, and D. Vanderbilt. *Phys. Rev. B*, 47:10142–10153, 1993.

[152] H. J. Monkhorst and J. D. Pack. *Phys. Rev. B*, 13:5188–5192, 1976.

[153] F. D. Murnaghan. *Proceedings of the National Academy of Sciences*, 30:244–247, 1944.

[154] R. P. Feynman. *J. Phys. Rev. 2*, 56:340–343, 1939.

[155] W. H. Press. *Numerical Recipes in Fortran 77: The Art of Scientific Computing*. Fortran Numerical Recipes. University Press, 1992.

[156] R. A. Marcus. *J. Chem. Phys.*, 45:4493–4499, 1966.

[157] G. H. Vineyard. *J. Phys. Chem. Sol.*, 3:121–127, 1957.

[158] C. J. Cerjan and W. H. Miller. *J. Chem. Phys.*, 75:2800–2806, 1981.

[159] D. T. Nguyen and D. A. Case. *J. Phys. Chem.*, 89:4020–4026, 1985.

[160] W. Quapp. *Chem. Phys. Lett.*, 253:286–292, 1996.

[161] H. Taylor and J. Simons. *J. Phys. Chem.*, 89:684–688, 1985.

[162] J. Baker. *J. Comp. Chem.*, 7:385–395, 1986.

[163] H. Jónsson, G. Mills, and K. W. Jacobsen. *Nudged elastic band method for finding minimum energy paths of transition*, chapter 16, pages 385–404. World Scientific, 1998.

[164] T. A. Halgren and W. N. Lipscomb. *Chem. Phys. Lett.*, 49:225–232, 1977.

[165] M. J. Rothman and L. L. Lohr Jr. *Chem. Phys. Lett.*, 70:405–409, 1980.

[166] G. Henkelman, B. P. Uberuaga, and H. Jónsson. *J. Chem. Phys.*, 113:9901–9904, 2000.

[167] G. Henkelman and H. Jónsson. *J. Chem. Phys.*, 113:9978–9985, 2000.

[168] B. J. Berne, G. Cicotti, D. F. Coke, and Societá italiana di fisica. Euroconference on "Technical Advances in Particle-Based Computational Material Sicences". World Scientific, 1998.

[169] P. Giannozzi, S. Baroni, N. Bonini, M. Calandra, R. Car, C. Cavazzoni, D. Ceresoli, G. L. Chiarotti, M. Cococcioni, I. Dabo, and et al. *J Phys.: Cond. Matt.*, 21:395502, 2009.

[170] H.-M. Lin, S.-J. Tzeng, P.-J. Hsiau, and W.-L. Tsai. *Nanostruct. Mater.*, 10:465–477, 1998.

[171] G. S. T. Rao and D. T. Rao. *Sens. Act. B*, 55:166–169, 1999.

[172] B. B. Rao. *Mater. Chem. Phys*, 64:62–65, 2000.

[173] E. Comini, G. Faglia, G. Sberveglieri, Z. Pan, and Z. L. Wang. *Appl. Phys. Lett.*, 81:1869–1871, 2002.

[174] Q. H. Li, Y. X. Liang, Q. Wan, and T. H. Wang. *Appl. Phys. Lett.*, 85:6389–6391, 2004.

[175] Q. Wan, Q. H. Li, Y. J. Chen, T. H. Wang, X. L. He, J. P. Li, and C. L. Lin. *Appl. Phys. Lett.*, 84:3654–3656, 2004.

[176] Z. Fan and J. G. Lu. *Appl. Phys. Lett.*, 86:123510, 2005.

[177] C. Li, D. Zhang, X. Liu, S. Han, T. Tang, J. Han, and C. Zhou. *Appl. Phys. Lett.*, 82:1613–1615, 2003.

[178] A. Mordecai. *Nonlinear Programming: Analysis and Methods*. Dover, 2003.

[179] F. Birch. *J. Geophys. Res.*, 83:1257, 1978.

[180] L. Ley, R. A. Pollak, F. R. McFeely, S. P. Kowalczyk, and D. A. Shirley. *Phys. Rev. B*, 9:600–621, 1974.

[181] A. Calzolari, A. Ruini, and A. Catellani. *J. Am. Chem. Soc.*, 133:5893–5899, 2011.

[182] K. J. Hameeuw, G. Cantele, D. Ninno, F. Trani, and G. Iadonisi. *J. Chem. Phys.*, 124:024708, 2006.

[183] L. Bengtsson. *Phys. Rev. B*, 59:12301–12304, 1999.

[184] N. R. D'Amico, G. Cantele, and D. Ninno. *J. Phys. Chem. C*, 116:21391–21400, 2012.

[185] K. Reuter and M. Scheffler. *Phys. Rev. B*, 65:035406, 2001.

[186] G. Henkelman, G. Jóhannesson, and H. Jónsson. *Progr. Theor. Chem. Phys.*, page 269, 2000.

[187] E. Kaxiras, Y. Bar-Yam, J. D. Joannopoulos, and K. C. Pandey. *Phys. Rev. B*, 35:9625–9635, 1987.

[188] G.-X. Qian, R. M. Martin, and D. J. Chadi. *Phys. Rev. B*, 38:7649–7663, 1988.

[189] J. E. Northrup. *Phys. Rev. Lett.*, 62:2487–2490, 1989.

[190] P. J. Linstrom and W. G. Mallard. *NIST Chemistry WebBook ,NIST Standard Reference Database Number 69.* National Institute of Standards and Technology, Gaithersburg MD, 20899, 2003.

[191] H. J. Kulik, M. Cococcioni, D. A. Scherlis, and N. Marzari. *Phys. Rev. Lett.*, 97:103001, 2006.

[192] C. Franchini, R. Podloucky, J. Paier, M. Marsman, and G. Kresse. *Phys. Rev. B*, 75:195128, 2007.

[193] D. J. Cooke, A. Marmier, and S. C. Parker. *J. Phys. Chem. B*, 110:7985–7991, 2006.

[194] M. J. S. Spencer, K. W. J. Wong, and I. Yarovsky. *Mater. Chem. Phys.*, 119:505–514, 2010.

[195] I. Borriello, G. Cantele, D. Ninno, G. Iadonisi, M. Cossi, and V. Barone. *Phys. Rev. B*, 76:035430, 2007.

[196] N. L. Marana, V. M. Longo, E. Longo, J. B. L. Martins, and J. R. Sambrano. *J. Phys. Chem. A*, 112:8958–8963, 2008.

[197] Y. Yan, M. M. Al-Jassim, and S.-H. Wei. *Phys. Rev. B*, 72:161307, 2005.

[198] A. Calzolari and A. Catellani. *J. Phys. Chem. C*, 113:2896–2902, 2009.

[199] T. Kaewmaraya, B. Pathak, C. M. Araujo, A. L. Rosa, and R. Ahuja. *Europhys. Lett.*, 97:17014, 2012.

[200] S. J. Clark, J. Robertson, S. Lany, and A. Zunger. *Phys. Rev. B*, 81:115311, 2010.

[201] B. Meyer. *Phys. Rev. B*, 69:045416, 2004.

[202] G.-Y. Huang, C.-Y. Wang, and J.-T. Wang. *Sol. St. Comm.*, 149:199–204, 2009.

[203] P. Erhart and K. Albe. *Appl. Phys. Lett.*, 88:201918, 2006.

[204] G.-Y. Huang, C.-Y. Wang, and J.-T. Wang. *Chin. Phys. B*, 19:013101, 2010.

[205] L. S. Vlasenko and G. D. Watkins. *Phys. Rev. B*, 72:035203, 2005.

[206] L. S. Vlasenko and G. D. Watkins. *Phys. Rev. B*, 71:125210, 2005.

[207] F. Capasso and G. Margaritondo. *Heterojunction band discontinuities: physics and device applications*. North-Holland, 1987.

[208] G. Margaritondo. *Electronic structure of semiconductor heterojunctions*. Perspectives in condensed matter physics. Jaca Book, 1988.

[209] A. Franciosi and C. G. Van de Walle. *Surf. Sci. Reports*, 25:1–140, 1996.

[210] E. H. Rhoderick and R. H. Williams. *Metal-semiconductor contacts*. Monographs in electrical and electronic engineering. Clarendon Press, 1988.

[211] W. Mönch. *Electronic Structure of Metal-Semiconductor Contacts*. Perspectives in Condensed Matter Physics. Springer, 1990.

[212] F. Flores and C. Tejedor. *J Phys. C: Sol. St. Phys.*, 20:145, 1987.

[213] M. Peressi, N. Binggeli, and A. Baldereschi. *J. Phys. D: Appl. Phys.*, 31:1273, 1998.

[214] A. C. Tuan, T. C. Kaspar, T. Droubay, Jr. J. W. Rogers, and S. A. Chambers. *Appl. Phys. Lett.*, 83:3734–3736, 2003.

[215] M. S. Hybertsen and S. G. Louie. *Phys. Rev. B*, 34:5390–5413, 1986.

[216] S. B. Zhang, D. Tomanek, S. G. Louie, M. L. Cohen, and M. S. Hybertsen. *Sol. St. Comm.*, 66:585–588, 1988.

[217] X. Zhu and S. G. Louie. *Phys. Rev. B*, 43:14142–14156, 1991.

[218] A. Baldereschi, S. Baroni, and R. Resta. *Phys. Rev. Lett.*, 61:734–737, 1988.

[219] L. Kleinman. *Phys. Rev. B*, 24:7412–7414, 1981.

[220] C. E. Patrick and F. Giustino. *J. Phys.: Cond. Mat.*, 24:202201, 2012.

[221] J. P. Perdew and Y. Wang. *Phys. Rev. B*, 45:13244–13249, 1992.

[222] R. I. Eglitis and D. Vanderbilt. *Phys. Rev. B*, 77:195408, 2008.

[223] N. R. D'Amico, G. Cantele, and D. Ninno. *Appl. Phys. Lett.*, 101:141606, 2012.

[224] E. Finazzi, C. Di Valentin, G. Pacchioni, and A. Selloni. *J. Chem. Phys.*, 129:154113, 2008.

[225] S. Na-Phattalung, M. F. Smith, K. Kim, M.-H. Du, S.-H. Wei, S. B. Zhang, and S. Limpijumnong. *Phys. Rev. B*, 73:125205, 2006.

[226] G. Mattioli, F. Filippone, P. Alippi, and A. Amore Bonapasta. *Phys. Rev. B*, 78:241201, 2008.